

LANCASTER UNIVERSITY

**Towards a magnet-on-cantilever type
Carbon Nanotube Force Sensor for
Magnetic Resonance Force Microscopy**

by

Patrick Steger, M. Sc.

*This thesis is submitted in partial fulfilment of the requirements for the degree of
Doctor of Philosophy*

in the

Faculty of Science and Technology
Department of Physics



December 2024

Declaration of Authorship

I declare that this thesis has been composed by myself and has not been submitted in substantially the same form for the award of a higher degree elsewhere. The work presented is my own, except where stated otherwise by reference or acknowledgement.

I confirm that the total length of this thesis is about 38 338 words and does not exceed the 80 000 word limit of a PhD thesis.

At the time of writing of this thesis, work carried out for this thesis has not yet resulted in any publications. However, work that was reproduced from the author's master's thesis in [Section 4.2.3](#) has contributed to the following publications:

- N. Hüttner, S. Blien, **P. Steger**, A. N. Loh, R. Graaf, and A. K. Hüttel. “Optomechanical coupling and damping of a carbon nanotube quantum dot”, *Physical Review Applied* **20**, 064019 (2023)
- S. Blien, **P. Steger**, N. Hüttner, R. Graaf, and A. K. Hüttel. “Quantum capacitance mediated carbon nanotube optomechanics”, *Nature Communications* **11**, 1636 (2020)
- S. Blien, **P. Steger**, A. Albang, N. Paradiso, and A. K. Hüttel. “Quartz tuning-fork based carbon nanotube transfer into quantum device geometries”, *Physica Status Solidi B* **255**, 1800118 (2018)

Patrick Steger, M. Sc.

December 2024

BLANK PAGE

Abstract

Patrick Steger, M. Sc.

Towards a magnet-on-cantilever type Carbon Nanotube Force Sensor for Magnetic Resonance Force Microscopy

Doctor of Philosophy, December 2024

Magnetic resonance force microscopy (MRFM) is a scanning probe technique capable of producing high-resolution 3d magnetic resonance imaging (MRI) data from nanoscale sample volumes. The detection mechanism is based on the interaction between unpaired spins in the sample and a magnetic particle on a mechanical resonator, which transduces resonant spin flips into resonator motion. Several proof of concept experiments have demonstrated the detection of individual spins and sub-nanometre spatial resolution. However, practical implementations of the technique so far have not been able to achieve the same.

In this thesis a new design for a MRFM detector based on a carbon nanotube (CNT) nanoelectromechanical system (NEMS) is proposed. CNT resonators, due to their low mass, high compliance and high mechanical quality factor, are known to be excellent force detectors. The main challenge in fabrication of a CNT based MRFM detector is deposition of a high purity magnet on the nanotube without causing device degradation from fabrication induced defects and contamination. The proposed device design addresses this by using the substrate as shadow mask for material deposition on the nanotube. A corresponding fabrication process based on CNT stamp transfer is developed, aiming to produce ultraclean devices.

A device is successfully fabricated (skipping magnet deposition for initial characterisation) and characterised at millikelvin temperatures. It exhibits Coulomb blockade with minor disorder in the hole conduction regime and fully blocked current in electron conduction. Sixteen mechanical resonances in the MHz range with quality factors up to about 2×10^5 are identified, some of which are suspected to be parametric excitations.

Finally, first tests of a new method for the detection of nanotube motion are

presented. Electromechanical mixing is used to upconvert CNT mechanical frequencies to the GHz range and the signal is detected with a near quantum-limited Josephson travelling wave parametric amplifier as primary gain stage. Initial results seem promising, with measurement sensitivity clearly exceeding that of detection via electromechanically rectified dc current. Nanotube oscillation without external drive, presumably current-driven self-oscillation, is observed. Unfortunately, more data is still required to unambiguously identify the origin of non-driven oscillation and for determining the force sensitivity of the experiment.

Acknowledgements

Most work in modern science is a collaborative effort, and so I would like to thank the fantastic team of people who supported my work over the past couple of years.

First and foremost, I thank my supervisor Edward Laird for his invaluable support and guidance, and for many discussions that helped advance any projects I was working on, be it fridge engineering, sample fabrication, measurement techniques or data analysis. I also thank my deputy supervisor Jon Prance for his advice and his interest in my work.

Sample fabrication was a particular challenge during this project. Thus, I am all the more grateful for the great cleanroom crew that I was allowed to join at Lancaster QTC. I thank Kunal Lulla for introducing me to the cleanroom in general and much of the equipment therein. Special thanks go to Gary Vernon, our hero cleanroom technician, who single handedly has been keeping things up and running for the past few years. I would also like to thank fellow cleanroom users Sam Jones, Jono Hall, Adam Craig, Xiuxin Xia and Mahesh Soni who trained me on several pieces of equipment. To all the other cleanroom users, too many to name them all, thank you for the mutual support, our many discussions of various processes and the constant sharing of little tips and tricks and quirks of our equipment, which helped me improve my micro- and nanofabrication skills and played an important part in the success of my device fabrication. Thanks go to Fred Schedin at the cleanroom of the National Graphene Institute in Manchester, who helped me getting started with electron beam lithography.

Next, I would like to thank all fellow members of the Laird group and ultra-low temperature lab, I couldn't ask for better colleagues. Thanks to Saba Khan and Deepanjan Das for help with setting up our fridges and for many interesting discussions about carbon nanotubes, parametric amplifiers and many other things. Big thanks to Sam Dicker, who joined me in my project about halfway through. Without his tireless tinkering, meticulous documentation of processes and operating procedures and just extra manpower a lot of my work (especially developing my sample fabrication process) would have been a lot more difficult; we figured out the EBL eventually. I thank Matthew Green for his many contributions to the programming efforts in our group, especially his Python drivers for various lab instruments.

Thanks to Roch Schanen and Dima Zmeev for occasional support with various issues in the ULT lab and to Alan Stokes and Harald Schlegl for keeping the liquid nitrogen flowing. I would also like to thank all other members of the Laird group and ULT lab who haven't been mentioned by name, yet. It's great to work around people who are always willing to give advice or lend a helping hand whenever needed, and who are open for a chat (on or off topic) in the lab or over a cup of coffee when my brain needs a little bit of distraction.

Some of my first tasks after coming to Lancaster were installation, custom wiring and testing of two dry dilution fridges. I'd like to thank Jacob Bunn, Daniel Cox and Stephanos Aradiotis, three great engineers at Oxford Instruments, who installed our fridges, showed me how to use them and helped ironing out a few initial difficulties.

Thanks to Graham Chapman and his team in the machine shop, especially Reece Grimshaw and Phelton Stephenson, who made all the little bits and pieces we needed for installing our custom fridge wiring and automating our probe station. Thanks to Mike Thompson for allowing me to use his 3d printers. Many jigs, prototype parts and probe station and nanotube stamping setup components were made that way.

Thanks to Stephen Holt and Ashley Wilson and their team in the electronics workshop for their support with anything electronic and for their help with many soldering jobs. Thanks to Lucy Wilson for help with developing a buffer for feeding outputs from transimpedance amplifiers in our measurement rack into our fast digitiser cards. I did not forget about this, the prototype is still being tested, I promise.

Lastly, I would like to thank my family for their never ending unconditional support in everything I do. I thank my parents, who always encourage my creativity and curiosity and were among my first inspirations for becoming a scientist. I thank my sister Astrid for keeping me physically active and for the occasional much-needed reminder that there are loads of things to do outside the lab and away from my desk.

Table of Contents

Declaration of Authorship	iii
Abstract	v
Acknowledgements	vii
Table of Contents	ix
List of Figures	xi
List of Tables	xiii
List of Acronyms	xv
1 Introduction	1
2 Cryogenic setup	5
2.1 Fundamentals of dilution refrigeration	6
2.2 System overview	8
2.3 Cryostat wiring for experiments with quantum devices	10
3 Characterising a Josephson travelling wave parametric amplifier	17
3.1 Fundamentals of Josephson travelling wave parametric amplifiers . . .	17
3.2 Tuning of a Josephson travelling wave parametric amplifier	19
3.3 Josephson parametric amplifiers in magnetic fields	24
3.4 Y-factor measurement for characterisation of a cryogenic low-noise amplifier	26
4 Carbon nanotube nanoelectromechanical systems	33
4.1 Fundamental properties of carbon nanotubes	34
4.1.1 Structure of carbon nanotubes	34
4.1.2 Carbon nanotube band structure	37
4.2 Device design and fabrication techniques	44
4.2.1 Description of the device design	44
4.2.2 Carbon nanotube synthesis	47

4.2.3	Carbon nanotube stamp transfer	49
4.2.4	Device chip fabrication	59
4.2.5	Opportunities for process improvements	65
4.3	Low temperature electronic transport and Coulomb blockade	67
4.3.1	Carbon nanotube quantum dots	67
4.3.2	Transport spectroscopy of a carbon nanotube quantum dot	71
4.4	Carbon nanotube nanomechanical resonators	73
4.4.1	Transverse vibrations of a suspended carbon nanotube	74
4.4.2	Actuation and detection of vibrations	76
4.4.3	Frequency tuning and electromechanical backaction	79
5	Carbon nanotube vibration readout with a Josephson travelling wave parametric amplifier	83
5.1	A carbon nanotube as an electromechanical mixer	84
5.2	Build-up of experimental setup	85
5.3	Mechanical resonances detected through electromechanical mixing	89
5.4	Carbon nanotube oscillation without external drive	93
6	Conclusion and Outlook	101
	Bibliography	107

List of Figures

2.1	Schematic of a ^3He - ^4He dilution unit	7
2.2	Phase diagram of liquid ^3He - ^4He mixtures	8
2.3	Cryostat overview	9
2.4	Installed custom coax wiring for RF/MW signals	12
3.1	Fundamentals of a SNAIL based TWPA	18
3.2	Initial exploration of parameter space for TWPA tuning	21
3.3	TWPA gain and signal-to-noise ratio improvement	22
3.4	TWPA gain while using the cryostat's superconducting vector magnet	25
3.5	Matched temperature-variable noise source	27
3.6	Noise temperature measurement of the TWPA	29
4.1	Structure of graphene and carbon nanotubes	35
4.2	Chirality classes of carbon nanotubes	37
4.3	Band structure of graphene	39
4.4	CNT band structure in zone folding approximation	42
4.5	Room temperature conductance of CNT types	44
4.6	Design proposal for a CNT NEMS based magnet-on-cantilever type MRFM sensor	47
4.7	Tube furnace CVD setup for CNT synthesis	48
4.8	Commercially available quartz tuning forks for CNT growth and transfer	50
4.9	In-house fabricated Si combs for CNT growth and transfer	51
4.10	SEM images of CNT growth for stamp transfer	53
4.11	Setup for CNT stamp transfer	55
4.12	Schematics for CNT transfer process	57
4.13	CNT transfer in situ measurements example data	58
4.14	Process flow for the fabrication of a CNT NEMS	60
4.15	Through etched markers for aligning features on two sides of a Si/SiO ₂ wafer	62
4.16	SEM images of a device chip ready for CNT transfer	65
4.17	Schematic of a quantum dot	67
4.18	Coulomb blockade and single electron tunnelling in a quantum dot . .	69
4.19	Measurement setup for CNT quantum dot spectroscopy	71

4.20	Transport spectroscopy of a CNT quantum dot	72
4.21	Carbon nanotube mechanical resonator	74
4.22	Actuation and detection of CNT vibration	77
4.23	Mechanical resonance curves at high and low drive powers	77
4.24	Mechanical resonances and frequency tuning of the device	80
5.1	Measurement setup for CNT electromechanical mixing readout with a TWPA	87
5.2	Frequency components of the CNT electromechanical mixing signal .	90
5.3	Qualitative comparison of vibration detection sensitivity in dc current vs mixer sideband	92
5.4	Non-driven CNT oscillation as a function of temperature	94

List of Tables

2.1	List of RF/MW components installed in the cryostat	15
4.1	Electronic properties of graphene and CNTs	43
4.2	Overview of CNT device parameters	82
4.3	Summary of fit parameters for frequency tuning of CNT mechanical resonances	82

BLANK PAGE

List of Acronyms

AFM	atomic force microscopy
ac	alternating current
CAD	computer-aided design
CNT	carbon nanotube
CPW	coplanar waveguide
CVD	chemical vapour deposition
DAC	digital-to-analogue converter
dc	direct current
DI	deionised
DU	dilution unit
DUT	device under test
EBL	electron beam lithography
FEBID	focused electron beam induced deposition
HEMT	high electron mobility transistor
IPA	isopropyl alcohol
MC	mixing chamber
MW	microwave
MRFM	magnetic resonance force microscopy
MRI	magnetic resonance imaging
MRM	magnetic resonance microscopy
MWCNT	multi-wall carbon nanotube
NEMS	nanoelectromechanical system

NMR	nuclear magnetic resonance
PCB	printed circuit board
PECVD	plasma-enhanced chemical vapour deposition
PSD	power spectral density
PTR	pulse tube refrigerator
QD	quantum dot
RF	radio frequency
RIE	reactive ion etching
SEM	scanning electron microscopy
SNAIL	superconducting nonlinear asymmetric inductive element
SNR	signal-to-noise ratio
SQUID	superconducting quantum interference device
SWCNT	single-wall carbon nanotube
TWPA	travelling wave parametric amplifier
VNA	vector network analyser

Chapter 1

Introduction

Nuclear magnetic resonance (NMR) can be observed in materials that contain atomic nuclei with non-zero nuclear spin, such as ^1H , ^{13}C , ^{19}F or ^{31}P . A corresponding experiment begins with placing a sample of the material in a strong constant external magnetic field \mathbf{B}_0 (typically up to 20 T from a superconducting magnet in modern apparatus) to align the nuclear spins. Perturbation of the system by a weak oscillating magnetic field (typically in the radio frequency (RF) range) drives precession of the spins around \mathbf{B}_0 , which is detected as an induced voltage in a pickup coil. Significant perturbation and detectable signal levels can only be achieved with resonant perturbation, i.e., when the frequency of the oscillating field matches the Larmor frequency $\omega_L = |\gamma B_0| = |\frac{eg}{2m} B_0|$ of nuclear spins in the sample. Here γ is the gyromagnetic ratio for a nucleus with charge e and mass m , and g is the g-factor. Since the resonance condition depends on properties of the nucleus, NMR can identify chemical elements and distinguish between isotopes (as long as the nuclei have non-zero spin). The resonance condition also depends on the external static magnetic field at the location of the nucleus, which can be shielded by electrons in the local environment. Therefore, an element's NMR signature changes slightly as it participates in the formation of different chemical groups. This makes NMR a powerful and non-destructive tool for analysing the molecular structure of chemical compounds, testing the composition and purity of materials, monitoring of manufacturing processes and a few other applications.

When the external field \mathbf{B}_0 is non-uniform, the Larmor frequency of nuclei in the sample depends on position. This allows probing the NMR response of a sample with three-dimensional resolution and is the basis of magnetic resonance imaging (MRI), which is best known for its medical applications, and magnetic resonance microscopy (MRM), which is mostly found in scientific settings.

Unfortunately, even with the best modern NMR and MRI techniques, detection via electromagnetic induction requires macroscopic samples. The number of

nuclear spins contained in the smallest detectable spin ensemble is on the order 10^{12} [1]. To overcome this limitation and possibly even enable detection of single spins, J. A. Sidles in 1991 proposed switching from inductive detection to a force detection technique similar to what is used in atomic force microscopy (AFM) [2]. For this new technique, which is called magnetic resonance force microscopy (MRFM), a small ferromagnetic particle is attached to an ultrasensitive cantilever. The particle experiences a weak magnetic force from a nearby spin. If the spin is driven to perform oscillations at the cantilever frequency, this force will excite vibrations of the cantilever, which can be detected, for example, via optical methods.

The new technique quickly drew attention from experimentalists and important milestones have been achieved over the past 30 years. In 2004, D. Rugar *et al.* reported the detection of a single electron spin [3]. In 2009, 3D imaging of virus particles was demonstrated by C. L. Degen *et al.* [4]. Finally, in 2019, U. Grob *et al.* demonstrated sub-nanometre spatial resolution in one dimension when detecting ^1H in an adsorbate layer on a silicon nanorod [5].

Progress in the field often came with significant modifications in comparison to the initial proposal. The position of sample and magnetic particle is swapped in many experiments, switching from a magnet-on-cantilever configuration (as per the initial proposal and used for example in Refs. [3, 6]) to a sample-on-cantilever configuration (used for example in Refs. [4, 5, 7]). Various options for the mechanical resonator in the setup are being explored, including ultrasensitive silicon cantilevers [4, 5], silicon nanowires [7, 8] and silicon nitride membranes [9, 10]. Additionally, improved measurement protocols are being developed, using RF pulse sequences for spin manipulation and readout [5, 11] instead of a continuous wave approach. However, despite all this, the holy grail of MRFM, that is mapping the structure of complex molecules to a resolution of individual atoms, has not been accomplished, yet. The potential impact of such a “microscope for molecules” on fields like chemistry, biology and medicine is enormous and is a major motivation for continuing the search for better MRFM detectors and methods.

A promising strategy for building better force sensors from mechanical resonators is to use carbon nanotubes (CNTs) as cantilevers. The classical limit for the force sensitivity of a mechanical resonator is given by $S_{\text{FF}} = 4k_{\text{B}}T\frac{\sqrt{mk_0}}{Q}$ [12] with thermal energy $k_{\text{B}}T$, resonator mass m , spring constant k_0 and quality factor Q . Since CNT cantilevers are made from just a single macromolecule, they have very low mass, while their spring constant can be low and quality factors can be high [13], which promises great potential for outstanding force sensitivity. J. Moser *et al.* already demonstrated force sensitivity on the order of 10 zN [12] (exceeding performance of the best Si cantilevers [14] by more than an order of magnitude), with potential for

further improvement.

In this thesis a new detector design for MRFM at cryogenic temperatures is proposed. The design uses a doubly clamped ultraclean suspended CNT as a mechanical resonator. The overall device structure is that of a classical CNT nanoelectromechanical system (NEMS), allowing for electrical readout. This eliminates the experimental challenges of implementing optical readout methods (which are widely used for other MRFM detectors) in a cryostat. A magnet-on-cantilever configuration is chosen, as it likely allows more flexibility in sample preparation (depositing material on the middle of a suspended CNT is difficult) and keeps detectors reusable for many samples.

Since the sensitivity of a measurement not only depends on the quality of the detector, but also on noise in the experimental setup (introduced by, for example, amplifiers in the signal readout path) an attempt is made to implement a Josephson travelling wave parametric amplifier (TWPA) as primary gain stage in the signal readout of a CNT NEMS. This relatively new amplifier technology [15, 16] can be nearly noiseless, boosting the signal-to-noise ratio (SNR). Electromechanical mixing in the CNT device is used to upconvert the frequency of CNT vibrations into the frequency band of the TWPA.

The rest of this thesis is structured as follows: [Chapter 2](#) describes the cryogenic setup that is the platform for experiments presented in later chapters. Despite being part of the cryogenic setup, the TWPA is covered separately in [Chapter 3](#). After a brief description of the amplifier and its fundamental working principle, the rest of this chapter focuses on characterising the performance of our amplifier. [Chapter 4](#) is dedicated to CNT NEMSs. After a brief introduction to the molecular and electronic structure of CNTs, the MRFM detector design mentioned above and a corresponding fabrication method are presented. Subsequently, a successfully fabricated device (without a magnet) is characterised at millikelvin temperatures. Properties of the quantum dot that forms on the device are explored in electronic transport measurements, and mechanical resonances are identified. In [Chapter 5](#) CNT vibration detection via electromechanical mixing with the TWPA as primary amplifier is demonstrated. Challenges in implementation of this technique are discussed and initial experimental results are shown. Finally, the thesis concludes in [Chapter 6](#) with a short summary of important outcomes, suggestions for improving integration of the TWPA in electromechanical mixing experiments and an outlook on future work.

BLANK PAGE

Chapter 2

Cryogenic setup

With the exception of sample fabrication and some crude pre-characterisation at room temperature for the purpose of device selection (see [Section 4.2](#)), all experiments presented in the following chapters are performed at cryogenic temperatures. This is necessary due to the following reasons:

1. *CNT vibration detection mechanism*

We will see in [Section 4.4.2](#) that the detection mechanism for CNT vibrations relies on non-linearity of the device conductance. Best results are achieved when the device is deep in the Coulomb blockade regime (see [Section 4.3](#)), where sharpness of conductance variations is mostly determined by lifetime broadening, i.e., $T \ll \hbar\Gamma_{\text{lifetime}}/k_B$. With electron tunnel rates through a CNT quantum dot (see [Section 4.3.1](#)) typically on the order of a few hundred GHz, this requires temperatures much lower than a few Kelvin.

2. *CNT mechanical resonator phonon population*

With the objective of using CNT vibrations for highly sensitive detection of external forces on the nanotube, it is desirable to pre-cool the device as close as possible to its mechanical quantum ground state. For a CNT mechanical resonator with $\omega_m = 2\pi \cdot 250$ MHz this corresponds to a temperature $T = \hbar\omega_m/k_B \approx 12$ mK.

3. *Amplifier operation*

The first amplifier in the high frequency signal readout of [Chapter 5](#) is based on Josephson junctions made from Niobium (see [Chapter 3](#)). For the amplifier to properly function the Niobium needs to be in its superconducting state. The critical temperature of Niobium thin films is on the order of 7–9 K [[17](#), [18](#)].

All of these conditions can be met by using a dilution refrigerator as platform for the experiment.

This chapter begins with a brief description of the basic operation principle of a

dilution refrigerator. The rest of the chapter provides an overview of our cryostat and describes the custom wiring and components installed for the purpose of performing experiments on CNT NEMS and quantum devices.

2.1 Fundamentals of dilution refrigeration

Dilution refrigerators were first realised by P. Das *et al.* in 1965 [19]. Still being the only solution for reliable continuous cooling to milli-kelvin temperatures to date, they have become an essential platform for modern low-temperature physics. Commercial variants are used in laboratories worldwide to cool down experiments and the ongoing hype around quantum computing motivates developments towards larger scales and more available cooling power.

Plenty of literature on various cooling techniques for low-temperature experiments is available (e.g., use the textbooks by Pobell [20] or Enss and Hunklinger [21] as starting points). Here only a brief description of the working principle of a cryogen-free dilution refrigerator will be given, which is the type of cryostat used for all experiments in this thesis.

The term *cryogen-free* refers to the method of pre-cooling that is used to bring the cryostat to approximately liquid helium temperature. In a non-cryogen-free system (or “wet fridge”) the dilution refrigerator is submerged in a bath of liquid helium, which is in turn surrounded by vacuum, a bath of liquid nitrogen and another vacuum space to reduce boil-off of cryogenic liquids and provide thermal isolation. In a cryogen-free cryostat (or “dry fridge”) the system is pre-cooled by a pulse tube refrigerator (PTR), which in our case can reach a base temperature of approximately 3.5 K. Note that “dry” cryostats are cheaper to maintain and more convenient to operate than similarly sized “wet” systems, since no periodic refilling of cryoliquids is required. However, cryogen-free systems are typically more noisy due to vibrations from the PTR.

Further cooling below liquid helium temperatures is achieved by exploiting the phenomenon of spontaneous phase separation in liquid mixtures of the helium isotopes ^3He and ^4He . This is done in a separate closed-loop system, the cold part of which is called the dilution unit (DU) (see [Figure 2.1](#) for schematic).

The temperatures achieved by the pre-cooling stage allow the ^3He - ^4He mixture to condense into a liquid in the DU. By pumping on the still side of the DU the system temperature is reduced further via evaporation of the helium mixture at low pressure. From the phase diagram of liquid mixtures of helium isotopes shown in [Figure 2.2](#) we can see that, once the temperature gets low enough, the helium mixture spontaneously separates into two phases, one rich in ^3He and one rich in

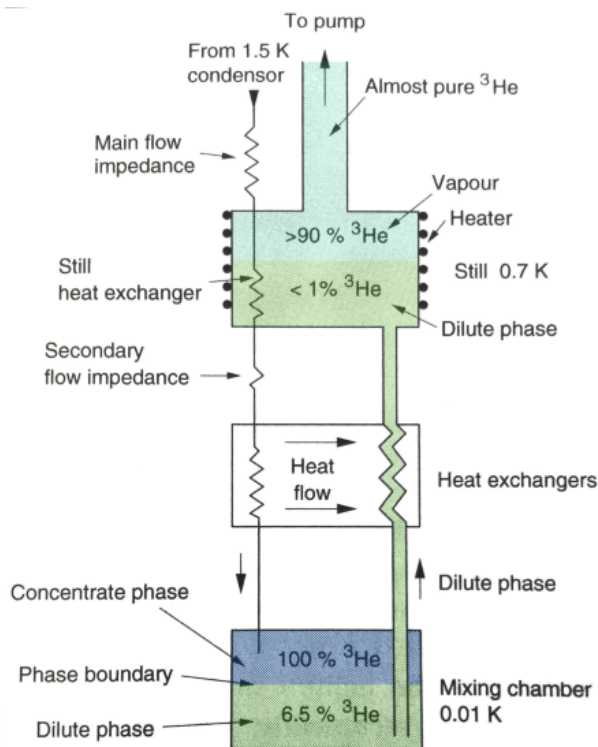


Figure 2.1: Schematic of the dilution unit in a ${}^3\text{He}$ - ${}^4\text{He}$ dilution refrigerator. See text for a description of the working principle. (Taken from [21], colour added)

${}^4\text{He}$. The two phases are called *concentrated* and *dilute*, respectively, referring to the concentration of ${}^3\text{He}$ contained in each phase. This phase separation is the result of a difference in attractive inter-atomic forces between different helium isotopes, combined with the Pauli exclusion principle applying to fermionic ${}^3\text{He}$ atoms but not to bosonic ${}^4\text{He}$ atoms [20]. The same effects also allow finite solubility of ${}^3\text{He}$ in ${}^4\text{He}$ at all temperatures, which is crucial for dilution refrigeration [20]. Due to different densities, the concentrated phase floats on top of the dilute phase, with the phase boundary located in the mixing chamber (MC). A siphon allows for the dilute phase to rise from the bottom of the MC into the still.

Due to the large difference in vapour pressure of the two helium isotopes, mostly ${}^3\text{He}$ evaporates in the still, despite its low concentration. This pushes the dilute phase away from its equilibrium isotope ratio. Equilibrium is restored by ${}^3\text{He}$ atoms crossing the phase boundary in the MC. Pulling ${}^3\text{He}$ atoms across the phase boundary comes with an energy penalty. The required energy is taken from the environment, thus providing cooling power at the MC. Assuming equal temperatures for both liquid phases of the helium mixture, the cooling power is directly proportional to the flow of ${}^3\text{He}$ through the phase boundary [20]:

$$\dot{Q} = 84\dot{n}_3 T^2 \quad (2.1)$$

where \dot{n}_3 is the molar flow rate of ${}^3\text{He}$.

The process is made continuous by pumping gaseous helium out of the still and

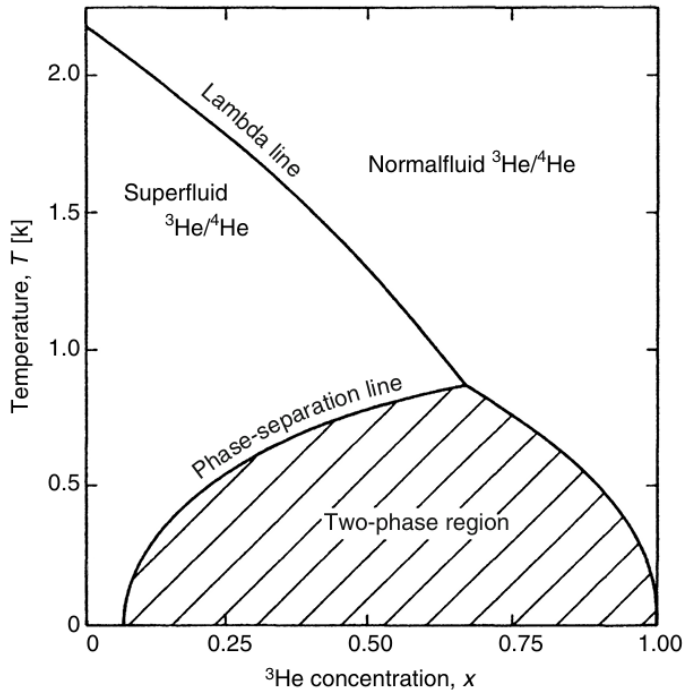


Figure 2.2: Phase diagram of liquid ${}^3\text{He}$ - ${}^4\text{He}$ mixtures at saturated vapour pressure. The lambda line marks the transition from a normal fluid to Fermi liquid ${}^3\text{He}$ in superfluid ${}^4\text{He}$. Mixtures below the phase-separation line spontaneously separate into two phases, one rich in ${}^3\text{He}$, the other rich in ${}^4\text{He}$. (Adapted from [20] which gives additional references for data sources that were used to construct this plot)

returning it to the condenser side of the DU. Flow impedances keep the pressure high enough to allow re-condensation. The returning helium is pre-cooled in heat exchangers by the already cold ${}^3\text{He}$ rising to the still before it enters the concentrated phase in the MC.

2.2 System overview

Figure 2.3(a) shows an overview of the insert of our Oxford Instruments Triton DR-15-300-H dilution refrigerator. During operation this sits inside a vacuum space and inner stages are surrounded by metallic radiation shields mounted to the PT1, PT2 and still stages for thermal isolation. A Lakeshore 372 AC resistance bridge and temperature controller reads temperatures from thermometers installed on all cryostat stages. It can apply power to a resistive heater on the mixing chamber stage for PID controlled temperature regulation. Another heater is installed on the still plate for tuning He mixture circulation rate and optimising available cooling power.

The system base temperature is less than 8mK ¹. Available cooling power on the still and mixing chamber stages can be measured by applying a known heat load via the installed heaters and allowing the system to reach steady state. The applied heat load then corresponds to the available cooling power on the respective cryostat stage at its steady state temperature. We obtain cooling powers of 9.9mW

¹Installed thermometers are only calibrated down to 8mK . The actual system base temperature is lower than that, so no precise number can be given.

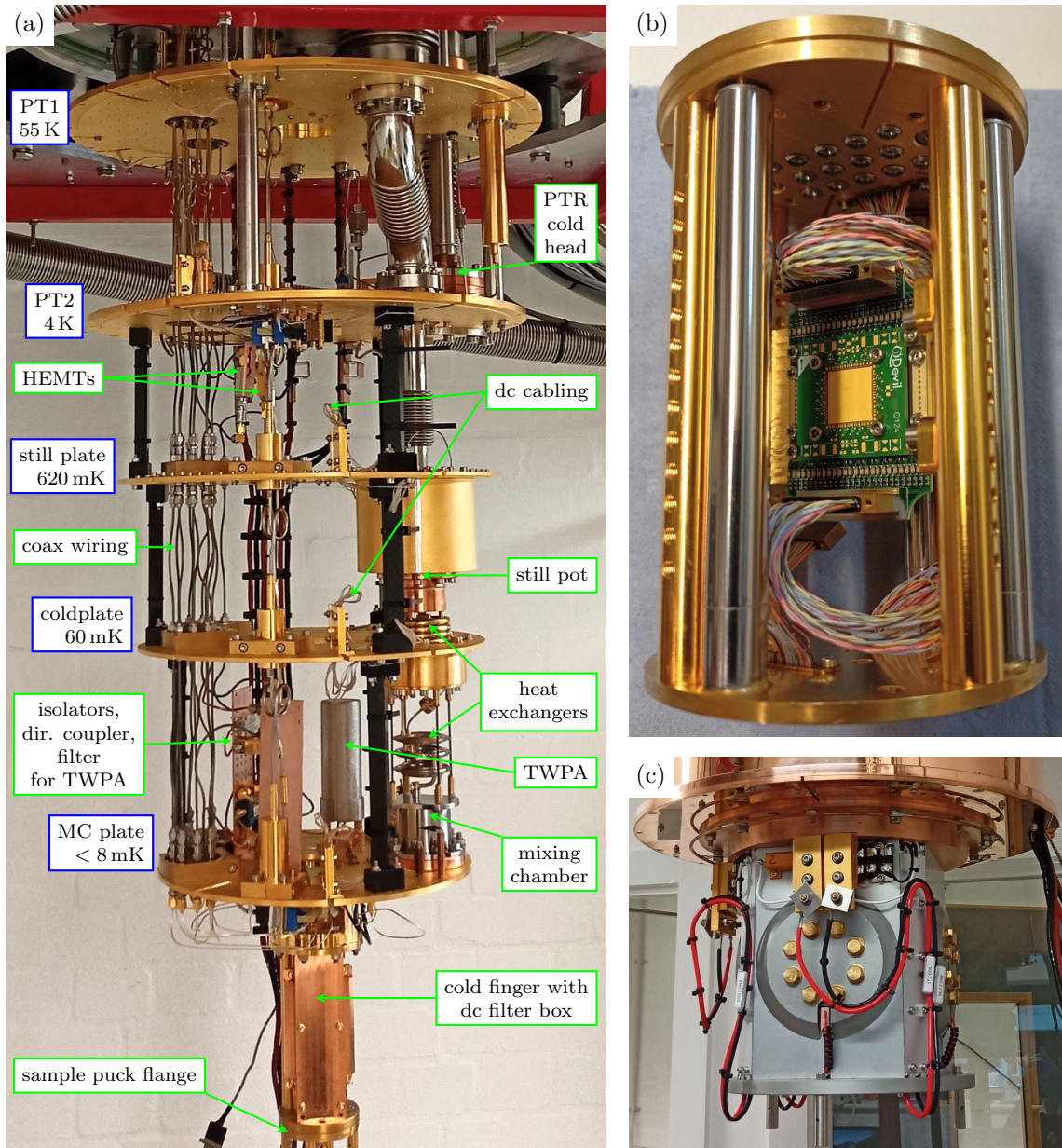


Figure 2.3: Overview of our Oxford Instruments Triton DR-15-300-H dilution refrigerator. (a) Cryostat insert. Temperature stages and important components are labelled. (b) Puck (outer shell removed) for loading samples onto the cold finger on the cryostat’s mixing chamber stage. Samples are glued and wire bonded into a sample carrier PCB stack from QDevil. The sample carrier connects to the cryostat wiring via a 51-way nano-D connector for dc signals and up to 16 MiniCoax to SMP coax cable assemblies for RF/MW signals. (c) Three-axis vector magnet (max. field: 1 T/1 T/6 T in $X/Y/Z$) mounted to the radiation shield of the 4 K stage. The mounting position for the sample puck is in the centre of the magnet bore.

at 900 mK for the still stage and 250 μ W at 80 mK for the mixing chamber. The constant flow of ^3He from the mixing chamber towards the still also provides cooling power on the cold plate. However, since we do not know the He flow rate in our system, and with no heater installed on the cold plate, we can neither measure nor calculate the cold plate cooling power. Typical values for similar systems found in literature are on the order of 200 μ W at 140 mK [22].

The cryostat is equipped with a three-axis superconducting vector magnet (Figure 2.3(c)) that can produce up to 1 T along its X - and Y -axis and up to 6 T in the Z direction.

We use a QBoard non-magnetic sample holder from QDevil² to mount sample chips in the cryostat. Samples are glued and wire bonded into a small daughterboard printed circuit board (PCB), which is then mounted onto a larger motherboard PCB. Electrical contact between the boards is made through a fuzz button interposer. The motherboard connects to the cryostat wiring via a 51-way nano-D connector (48 pins used) for dc signals and up to 16 MiniCoax connectors for RF/MW signals. Each RF line is connected to a dc line through a bias tee on the motherboard, leaving us with 32 clean dc lines and 16 lines for combined dc+ac signals. Each dc line on the motherboard is equipped with an RC lowpass filter with 132 kHz cutoff frequency.

The sample holder is mounted in a puck (Figure 2.3(b)) which connects to the flange on a cold finger extending down from the mixing chamber stage. This positions the sample in the centre of the vector magnet’s bore, where the magnet can produce uniform fields. The cryostat is equipped with a load-lock that allows exchange of sample pucks without fully thermal cycling the cryostat or breaking the vacuum space around the insert.

2.3 Cryostat wiring for experiments with quantum devices

Our dilution refrigerator is equipped with factory installed cabling for dc signals. This is implemented as twisted pair cables in loom wires that are clamped between metal brackets on every cryostat stage for thermalisation, providing 48 dc connections from room temperature to the sample space and 24 spare dc lines from room temperature to the 4 K stage. Some of the spare dc lines are used for supplying power to amplifiers on the 4 K stage. The remaining spare lines are extended to the mixing chamber stage using superconducting NbTi twisted pair loom wire for operating a TWPA and a temperature-variable noise source (see Section 3.4).

²Now part of Quantum Machines (Q.M Technologies Ltd.)

To minimise (thermal) noise that reaches the sample through the dc wiring, all dc connections to the sample space are routed through a filter box that was added to the cold finger (see bottom of [Figure 2.3\(a\)](#)). The box contains a PCB with RC lowpass filters (approximately 90 kHz cutoff frequency) and three stages of LC lowpass filters (cutoff frequencies 80 MHz, 1450 MHz and 5000 MHz). Long meandering copper traces on the PCB run next to microwave absorbing foam (Eccosorb[®] LS-26) to filter out noise in the GHz range.

For high-frequency signals a custom set of $50\ \Omega$ matched 2.19 mm outer-diameter semi-rigid coaxial cabling is installed, see [Figure 2.4\(a\)](#) for schematics. It consists of one readout for RF signals that can also be used for RF reflectometry, one readout for MW signals and several input/drive lines. The readout lines are each equipped with a high electron mobility transistor (HEMT) amplifier at the 4 K stage, both with a nominal gain of 36 dB. Additionally, the MW readout has a TWPA installed, which we will discuss in more detail in [Chapter 3](#). One of the input lines is reserved for a pump tone in the MW range that is required for operating the TWPA. The pump tone enters the TWPA through the same port as signals from the sample and is injected into the signal path via a directional coupler. A lowpass filter at the TWPA output attenuates the pump tone to avoid saturation of subsequent gain stages and readout electronics.

Below the 4 K stage superconducting NbTi cables are used to minimise signal loss from dissipation in the cables. The low thermal conductivity of superconductors also helps keeping the passive heat load from the added connections between cryostat stages low. Below the mixing chamber stage, near the vector magnet, magnetic fields can exceed the critical field of superconducting wiring when the magnet is operated at high fields. To eliminate possible complications in future experiments from cables switching between their superconducting and normal conducting state, copper coax cables with silver plated inner conductors are used in this area.

The coax cabling is routed through the stages of the cryostat via firmly clamped SMA bulkheads to thermalize the outer conductors. On stages with more available cooling power (i.e., the 4 K, still and mixing chamber plates) attenuators are used for thermalisation of input signals. The choice of attenuator values is a compromise between the following considerations:

- *Noise reduction*

The main purpose of these attenuators is dissipation of thermal noise that comes from higher stages in the cryostat or room temperature. For example, an attenuator with attenuation $A = 20\ \text{dB} = 100$ transmits only 1 % of incident noise (and signal!), the remaining 99 % are dissipated in the attenuator.

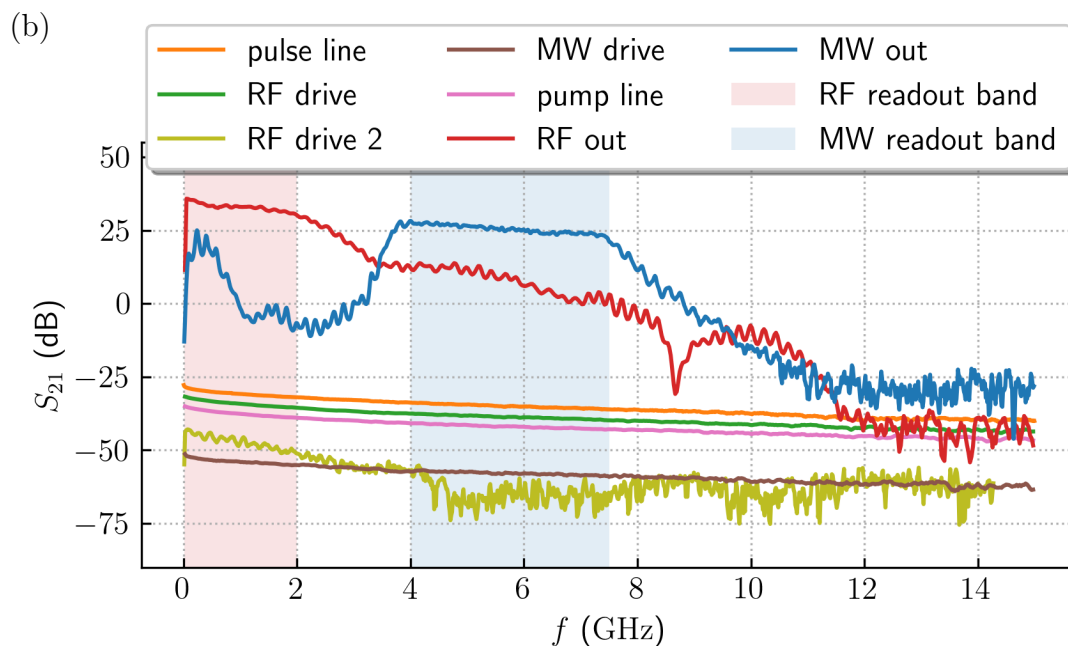
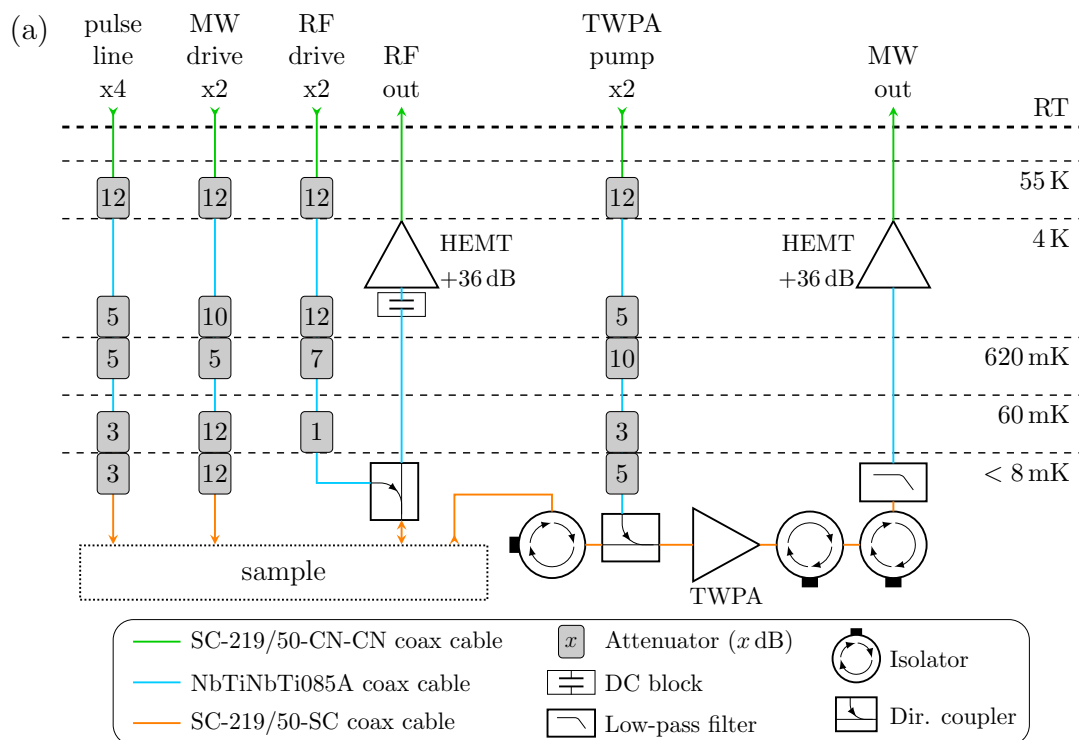


Figure 2.4: Custom coax wiring installed in our cryostats. (a) Schematic of the installed wiring with four pulse lines, two low noise MW inputs, one RF reflectometry setup and one MW output with TWPA. One spare RF drive and TWPA pump line each connect to the sample space for additional inputs (not shown). Dc cabling for amplifier power supplies and TWPA flux biasing is not shown. (b) Measured RF/MW transmission of the installed wiring at base temperature (TWPA was not pumped).

- *Attenuation of input levels*

This is usually a minor concern, since required signal levels for quantum devices are generally low (e.g., on the order of -66 dBm [22]) and more attenuation in the wiring can easily be compensated for by starting with a higher signal level from the source at room temperature.

- *Blackbody radiation of the attenuator*

The attenuator will emit blackbody radiation with the temperature at which it is thermalized back into the signal path. Therefore, efficient thermal anchoring of the attenuators is crucial. The level of attenuation should not be chosen too high to avoid excessive heating of the attenuator from dissipation of noise and input signals.

Thus, in our setup the MW drive lines are best for weak low-noise signals, while the other input lines are better for stronger signals at the expense of being slightly more noisy. On the readout lines, attenuators are not suitable for thermalisation, as we cannot afford throwing away precious signal power. Instead, circulators protect the TWPA and sample from noise emitted at higher stages of the cryostat, as well as from back reflected signals. For a more in-depth discussion of the engineering considerations that go into designing a dilution refrigerator layout for quantum experiments, see [22]. For a list of installed components in our cryostat see [Table 2.1](#)

After installation of the coax wiring, transmission of all lines is characterised with a Keysight P9375A vector network analyser (VNA) with the cryostat at base temperature. Lines are connected pairwise with short pieces of coax cable in the sample puck and the total transmission

$$S_{21}[\text{unit: dB}] = 10 \log_{10} \frac{P_{\text{out}}}{P_{\text{in}}} \quad (2.2)$$

through the pair of lines is measured, where P_{in} is the power of a probe tone injected into port 1 of a 2-port network and P_{out} is the signal power received at port 2 after the probe tone has travelled through the network. Initially, identical lines (e.g., two pulse lines) are paired together. Assuming that equally constructed lines contribute equally to the measured S_{21} , the transmission of a single line can be determined. Lines that were characterised this way can subsequently be paired up with the remaining lines to collect S_{21} data for all lines. The results are shown in [Figure 2.4\(b\)](#). The frequency ranges of the RF and MW readout marked in the figure are determined by frequency specifications of the installed components as stated in their respective datasheets. The RF band is only limited by the specifications of the HEMT. The frequency limit of the MW band is set by the circulators at the low end and by the cutoff frequency of the lowpass filter at the high end. The flatness of the

curves confirms that the wiring was installed properly (impedance mismatch from, for example, improperly installed connectors would manifest as significant ripple in the measured S_{21}). The reduction of S_{21} towards higher frequencies comes from increased cable losses due to skin effect. This data can be used to calibrate for cable losses and amplifier gain in future experiments.

The cryostat base temperature after installation of the additional wiring is still below 8 mK, showing that the additional passive heat load must be very low.

A nearly identical second cryostat (without TWPA, vector magnet and load lock) was installed and equipped with the same set of custom wiring.

Component	Part number	Specifications
RF HEMT	CITLF3 (Cosmic Microwave Technology)	RF band 0.01 – 2 GHz Gain 36 ± 2 dB Noise < 5.5 K
MW HEMT	LNF-LNC0.3_14A (Low Noise Factory)	RF band 0.3 – 14 GHz Gain 36 dB Noise 4.2 K typ.
RF dir. coupler	ZX30-12-4+ (Mini-Circuits)	RF band 5 – 1000 MHz Coupling 12 dB
MW dir. coupler	KRYTAR_120420 (Krytar)	RF band 4 – 12.4 GHz Coupling 20 dB
circulator (single junction)	LNF-CIC4_12A (Low Noise Factory)	RF band 4 – 12 GHz Ins. loss 0.2 dB typ. Isolation 20 dB typ.
circulator (dual junction)	LNF-CICIC4_12A (Low Noise Factory)	RF band 4 – 12 GHz Ins. loss 0.4 dB typ. Isolation 30 dB typ.
lowpass filter	FLP-0750 (Marki Microwave)	f_{cutoff} 7.5 GHz Ins. loss 0.9 dB typ. (passband) Ins. loss 50 dB @ 12 GHz (stopband)
DC block	BLKD-183-S+ (Mini-Circuits)	RF band 0.01 – 18 GHz Ins. loss 0.43 dB typ. DC block inner and outer conductor

Table 2.1: List of RF/MW components installed in the cryostat

BLANK PAGE

Chapter 3

Characterising a Josephson travelling wave parametric amplifier

In this chapter we shall have a closer look at the TWPA that we installed on the mixing chamber stage of our dilution refrigerator as part of the MW readout electronics. The amplifier was developed and fabricated by our collaborators at VTT Technical Research Centre of Finland Ltd. A full theoretical picture of such an amplifier, as well as the engineering required to design and build one, are well beyond the scope of this thesis. Instead, after only a brief introduction, we shall focus on characterising the performance of the amplifier in our setup.

3.1 Fundamentals of Josephson travelling wave parametric amplifiers

Our TWPA is a superconducting coplanar waveguide (CPW) transmission line where the centre conductor is made from a meta-material with non-linear inductance (see [Figure 3.1\(a\)](#) for simplified schematic). The superconductor used is niobium.

The meta-material of a TWPA centre conductor is made of Josephson elements, i.e., the centre conductor is a chain of unit cells that each contain one or more Josephson junctions. Several TWPA architectures with different unit cell designs have been demonstrated (e.g., superconducting quantum interference device (SQUID) photonic crystals [23] or a Josephson LC-ladder with periodically added resonator phase shifters for signal phase matching [16]). In our case the centre conductor is made of superconducting nonlinear asymmetric inductive elements (SNAILS) [24]. These are Josephson dipole elements consisting of an asymmetric loop with n large

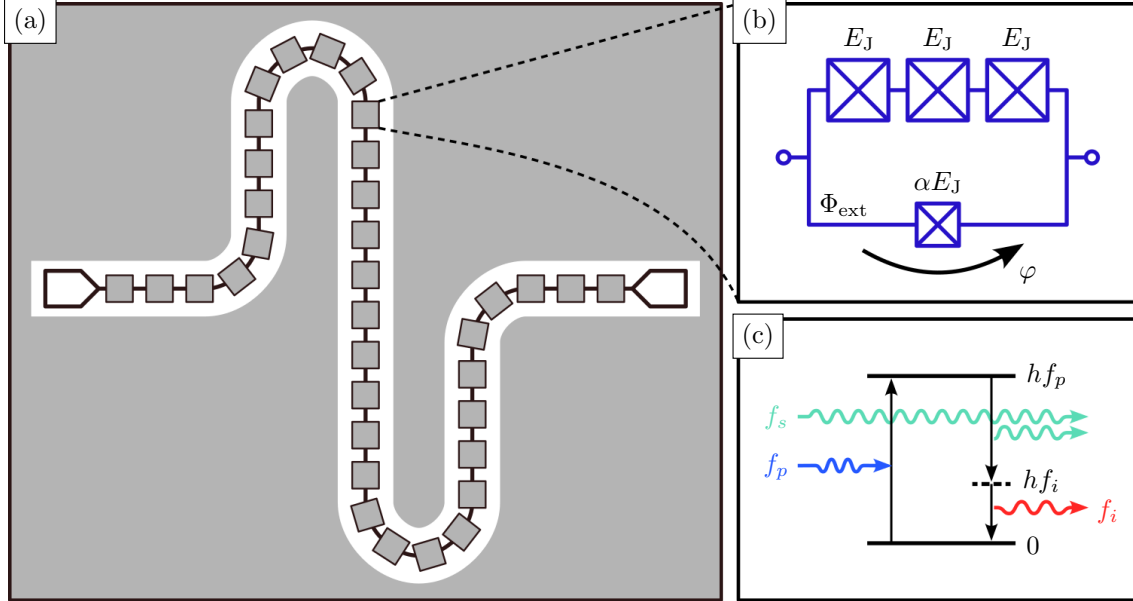


Figure 3.1: (a) Simplified layout of a TWPA (magnetic flux bias line not shown). It consists of a CPW transmission line with the centre conductor made of a meta-material with nonlinear inductance. Non-linearity of the inductance allows parametric amplification in a 3-wave mixing process. (b) Schematic of a SNAIL, an asymmetric loop of $n = 3$ large Josephson junctions and one smaller junction (tunnelling energies E_J and αE_J , respectively), threaded by an external magnetic flux Φ_{ext} and fully parametrised by the superconducting phase difference φ across it. This is the unit cell for constructing the centre conductor in our TWPA. (c) Parametric amplification via 3-wave mixing in the photon picture. A photon from a strong pump tone excites a virtual energy level. Decay of the excitation is stimulated by a photon of a weak signal, creating a copy of the signal photon. Conservation of energy requires the appearance of an idler signal at $f_i = f_p - f_s$. (Panel (b) redrawn from [24].)

Josephson junctions (tunnelling energy E_J) on one side and one smaller junction (tunnelling energy αE_J) on the other side (see Figure 3.1(b) for schematic of an example with $n = 3$). The inductance of a SNAIL, as well as the coefficients in a Taylor expansion of the inductance (i.e., the presence and strength of different order non-linearities in the inductance), depend on n , α and the external magnetic flux Φ_{ext} that threads the SNAIL loop [24, 25]. Thus, by choosing appropriate values for n and α and carefully tuning Φ_{ext} , one can impedance-match a SNAIL TWPA to 50Ω matched MW circuitry and simultaneously choose whether non-linear processes in the amplifier should favour 3-wave mixing or 4-wave mixing [25]. In our amplifier Φ_{ext} is coming from a dc current I_{FB} running through a superconducting flux bias line fabricated on the TWPA chip.

Our amplifier is designed for parametric amplification in a 3-wave mixing process (Figure 3.1(c)). When a strong pump tone with frequency f_p and a weak signal with frequency f_s travel through the TWPA together, the non-linearity of the SNAIL

inductance allows energy transfer from the pump to the signal. Conservation of energy requires that an idler tone appears at frequency $f_i = f_p - f_s$ at the same time.

The amplifier is designed to support pump frequencies in the range 9–12 GHz and can be operated in two different modes:

1. *Phase-sensitive gain*

Pump and signal travel through the TWPA with a fixed phase relation. In 3-wave mixing this is only achieved with $f_p = 2f_s$, which also implies that the idler appears at the signal frequency ($f_s = f_i$).

2. *Phase-insensitive gain*

Frequencies of the signal, pump and idler still have to obey the relation $f_p = f_s + f_i$, but now with $f_s \neq f_i$. This is suitable for broadband amplification.

Throughout the rest of this thesis we will only consider and use the phase-insensitive mode.

3.2 Tuning of a Josephson travelling wave parametric amplifier

A TWPA is generally operated with fixed values for the pump frequency f_p , pump power P_p and flux biasing current I_{FB} . The datasheet of the amplifier provides suggestions for these parameters [25]. However, characteristics of the same TWPA can vary when measured at different laboratories. A possible explanation for this difference are slight variations in impedance matching of the connectors, cables and components that directly interface with the amplifier. Another common reason is a difference in the magnetic field environment of the TWPA, since the amplifier is very sensitive to global offset fields. Therefore, to achieve best amplifier performance in our setup, we consider the operating point suggested in the datasheet as a guide while looking for a new set of optimised parameters.

Our goal is to find an operating point where the TWPA provides good broadband gain, ideally with little gain ripple across the MW readout band. Since the TWPA gain depends on the signal frequency in addition to the three parameters f_p , P_p and I_{FB} of the operating point, this means we need to optimise the TWPA gain G_{TWPA} in a four-dimensional parameter space. Not only is this difficult to visualise, but exploring the whole parameter space to find the best working point would also be incredibly time consuming. Therefore, we first need to narrow down our search.

We use a short piece of coax cable inside the sample puck to connect one of the MW drive lines to the MW readout (cf. Figure 2.4(a)). We can then measure S_{21} for transmission of MW signals with a Keysight P9375A VNA. Using the calibration data from Figure 2.4(b), we can extract G_{TWPA} from this measurement.

To identify regions of interest for setting a new TWPA operating point, we first do a relatively coarse scan of f_p , P_p ³ and I_{FB} . The pump tone is supplied by a Windfreak SynthHD microwave signal generator, while the flux biasing current is coming from a battery powered voltage source. For each setpoint we record a VNA trace, sweeping the probe frequency between 3.5–8 GHz (i.e., across the whole MW readout band plus 500 MHz on both ends), and calculate the mean TWPA gain across the whole sweep as

$$\overline{G_{\text{TWPA}}} = \frac{1}{N} \sum_{j=1}^N G_{\text{TWPA}}(f_j) \quad (3.1)$$

where f_j and N are the frequency setpoints and number of points in the VNA sweep, respectively. The result is shown in Figure 3.2. Candidates for picking a TWPA operating point are regions with high and locally flat $\overline{G_{\text{TWPA}}}$. High $\overline{G_{\text{TWPA}}}$ of course corresponds to good broadband gain, while local flatness means that small fluctuations in the parameters of the operating point will likely have little effect on amplifier performance.

For the remainder of this thesis we pick $f_p = 12$ GHz and $I_{\text{FB}} = 820$ μA . With these two parameters fixed, we can repeat the same VNA measurement from before, this time sweeping only P_p and observing $G_{\text{TWPA}}(f)$ instead of just the mean gain across the whole bandwidth (see Figure 3.3(a)). We find two bands of highest gain for -5 dBm $< P_p < 5$ dBm. For $P_p > 5$ dBm the signal is attenuated instead, likely due to the pump tone exceeding the critical current of the SNAILs in the TWPA. Comparing traces of $G_{\text{TWPA}}(f)$ from the two regions of highest gain (Figure 3.3(b)), we find that higher pump power generally yields slightly more gain, while the trace for lower pump power exhibits less gain ripple. We pick the trace with less ripple as preferred operating point for our TWPA, and therefore will use $f_p = 12$ GHz, $P_p = -2.6$ dBm and $I_{\text{FB}} = 820$ μA throughout the rest of this theses whenever the TWPA is part of the experimental setup.

Every amplifier not only increases signal power, but also adds noise (more on this in Section 3.4). An amplifier only is a useful addition to a measurement setup

³Note that TWPA pump powers P_p throughout this theses are given as power levels supplied by a signal generator at room temperature. When the pump tone reaches the TWPA it has been attenuated by approx. 65 dB (see calibration data and component specifications in Section 2.3), with some variation due to frequency dependent attenuation in the pump line.

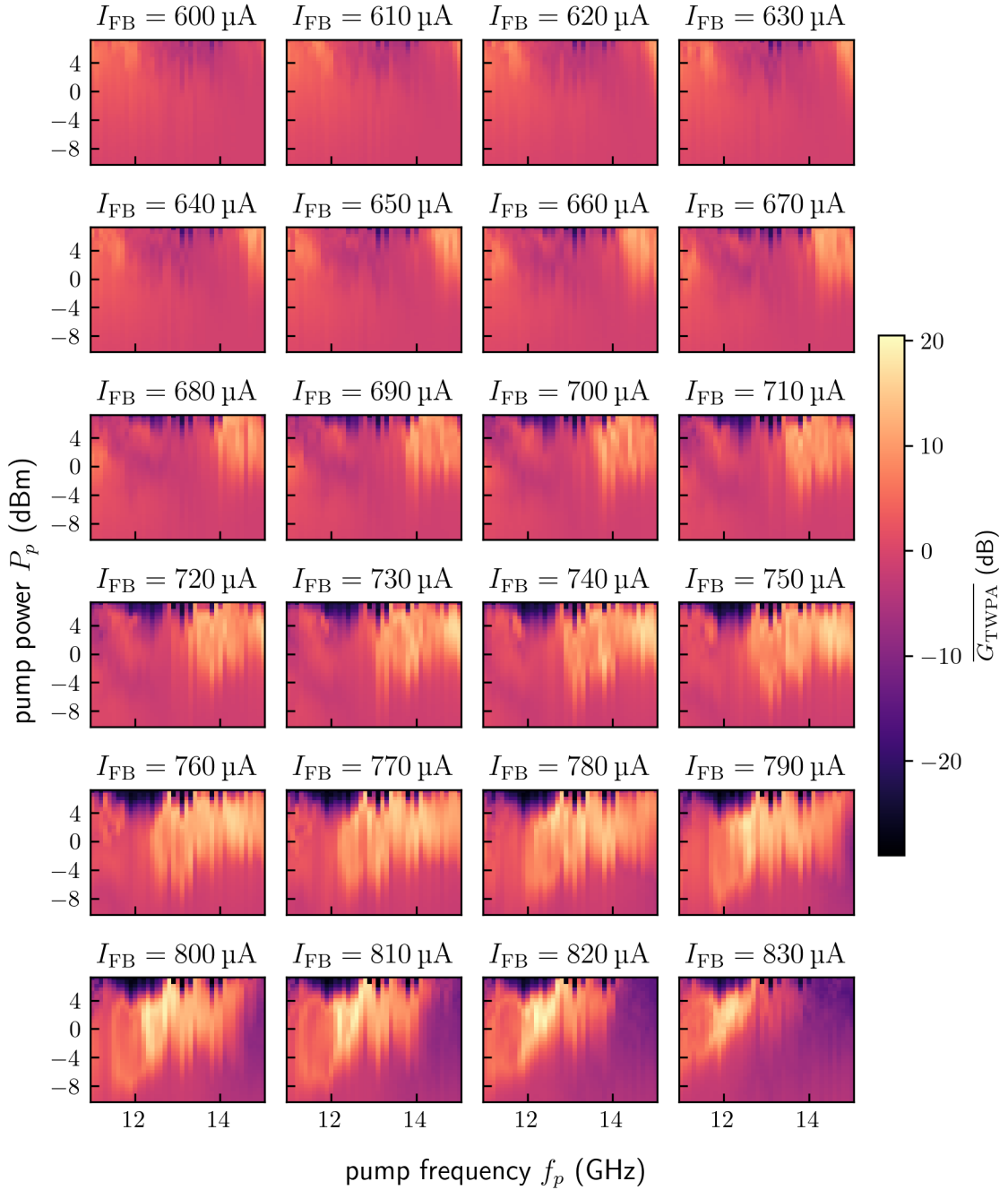


Figure 3.2: Initial exploration of parameter space for TWPA tuning. Plotted is the mean of the TWPA gain $\overline{G}_{\text{TWPA}}$ in the frequency range 3.5–8 GHz (MW readout band plus 500 MHz on both sides) as a function of pump power P_p and pump frequency f_p for different values of current I_{FB} through the flux bias line.

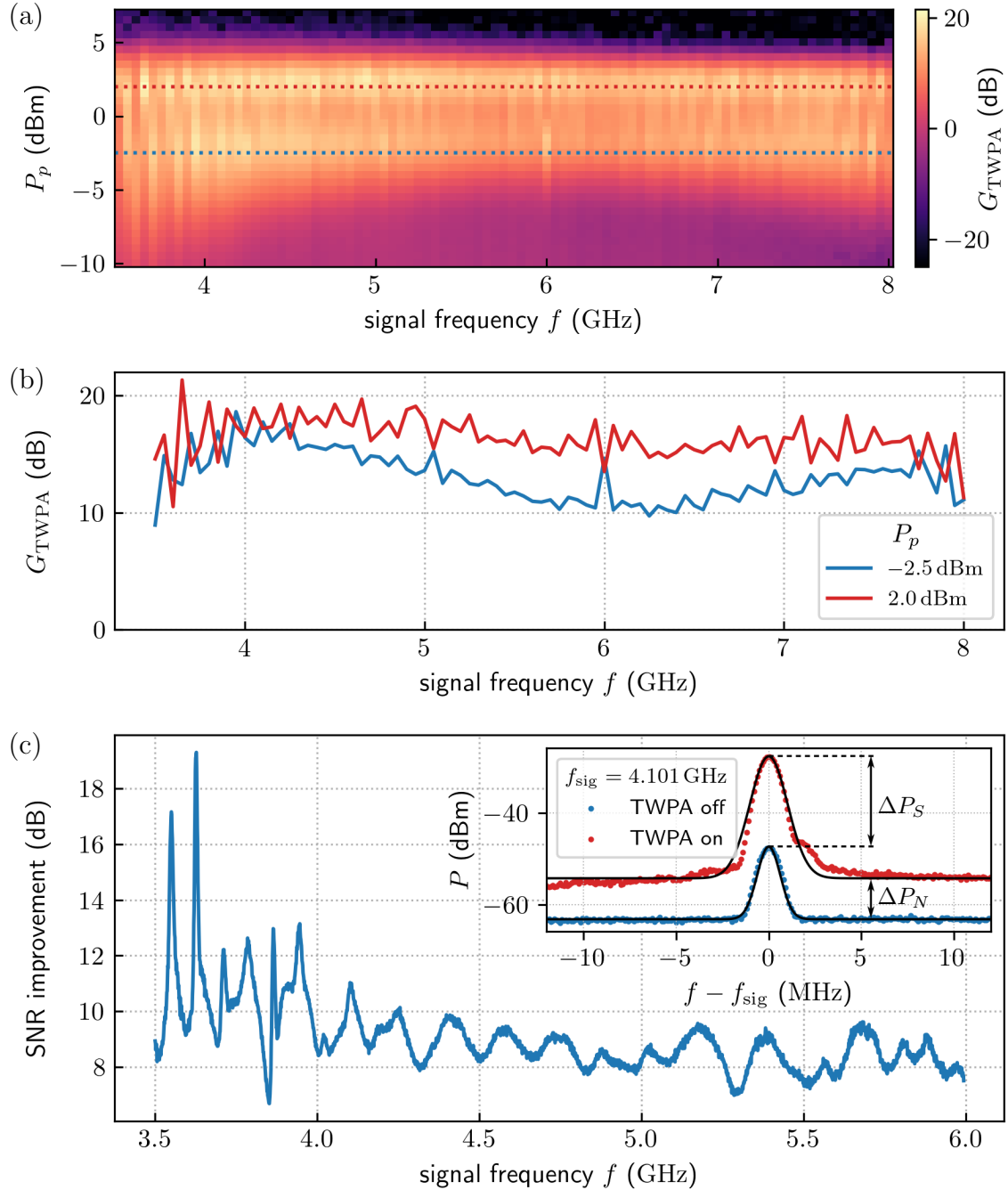


Figure 3.3: (a) TWPA gain for a range of pump powers P_p with $f_p = 12$ GHz and $I_{\text{FB}} = 820 \mu\text{A}$. We find two bands of highest gain for $-5 \text{ dBm} < P_p < 5 \text{ dBm}$. When the amplifier is overdriven ($P_p > 5 \text{ dBm}$), it blocks the signal instead of amplifying it. (b) Line cuts along the dotted lines in (a). For the higher pump power TWPA gain is slightly higher, but also exhibits more gain ripple. (c) SNR improvement from adding the TWPA to the MW readout circuitry ($f_p = 12$ GHz, $P_p = -2.6 \text{ dBm}$ and $I_{\text{FB}} = 820 \mu\text{A}$). Inset: Detection of a weak probe tone at $f_{\text{sig}} = 4.101$ GHz with the TWPA pump on (red) and off (blue). Dots are data measured with a spectrum analyser, black curves are Lorentzian peaks fitted to the data. The difference in signal levels ΔP_S is larger than the noise floor difference ΔP_N , and $\Delta \text{SNR} = \Delta P_S - \Delta P_N$ is the SNR improvement from the TWPA. Evaluating this comparison for many signal frequencies yields the main graph.

if the boost of signal power outweighs the added noise, i.e., if the amplifier improves SNR. We can verify that this is the case for our TWPA by removing the VNA from the previous experimental setup and instead connecting a signal generator to the MW drive line and a spectrum analyser to the MW readout. We then inject a weak probe tone from the signal generator into the setup and detect it with the spectrum analyser. Switching the TWPA pump on and off and comparing the detected signal, we find that the noise floor is higher when the amplifier is pumped, but the increase in signal level ΔP_S clearly exceeds the rise of the noise floor ΔP_N (see inset of [Figure 3.3\(c\)](#)). Evaluating this comparison for many probe tone frequencies, we find that the TWPA provides an SNR improvement of more than 8 dB for most of the MW readout band ([Figure 3.3\(c\)](#)). The TWPA datasheet suggests that SNR improvement as a function of pump power saturates at about 9 dB for a signal frequency of 4.25 GHz, indicating that we likely selected a reasonably good set of parameters for our TWPA operating point.

Note that while the TWPA provides an overall positive gain, a portion of the signal is still lost while it travels through the amplifier, primarily due to dissipation in the dielectric materials on the chip. This *insertion loss* of the TWPA was never measured directly in our setup, but we can estimate it from the underlying datasets of [Figure 3.3\(b\)](#) and [\(c\)](#). For this purpose we reparameterise our amplifier as an attenuator A representing the insertion loss, followed by an ideal amplifier with gain $G_{\text{TWPA}}^{\text{internal}}$ ⁴. The measured additional gain from installing the TWPA in the setup ([Figure 3.3\(a\)](#) and [\(b\)](#)) is then given by $G_{\text{TWPA}} = AG_{\text{TWPA}}^{\text{internal}}$. In contrast, the ratio of measured power levels of a weak probe tone when switching the TWPA pump on and off (labelled ΔP_S in the inset of [Figure 3.3\(c\)](#)) is given by only $G_{\text{TWPA}}^{\text{internal}}$, since the TWPA remains in the circuit and thus the signal experiences the insertion loss A in both cases. Indeed, $\Delta P_S = G_{\text{TWPA}}^{\text{internal}} = 19.5$ dB in the inset of [Figure 3.3\(c\)](#) is larger than $G_{\text{TWPA}} = 17.7$ dB for the same signal frequency in [Figure 3.3\(b\)](#). Comparing the two datasets for many probe tone frequencies, we find an average insertion loss of -1.7 dB in the frequency range 4–6 GHz, which is in good agreement with the TWPA datasheet.

⁴Note that this is a heavily simplified representation, since the losses that we summarise in the attenuator A at the input of the amplifier, in reality, are distributed across hundreds or thousands of components along the signal path inside the amplifier.

3.3 Josephson parametric amplifiers in magnetic fields

We have seen that precise control of the magnetic flux through the TWPA is important for its operation. We also have a superconducting vector magnet installed in our cryostat. To protect the TWPA from stray magnetic fields in the lab and especially from the vector magnet, it is encapsulated in multiple layers of shielding (Figure 3.4(a)). Additionally, in order to create as much physical separation between the TWPA and the vector magnet as possible, thereby minimising the strength of stray fields at the TWPA location, the amplifier is raised above the mixing chamber plate on a Cu cold finger and mounted offset from the axis of the magnet bore near the edge of the mixing chamber plate.

We shall perform a simple test to estimate safe magnetic field limits for operating the TWPA and vector magnet simultaneously. To do this we measure the TWPA gain with a VNA, using the same setup that was used for tuning the TWPA operating point in the previous section. Figure 3.4(b) shows the TWPA gain observed while sweeping the vector magnet’s field strength in different directions. Maximum field strength in the X/Y plane can be achieved along the diagonal at 45° between the X - and Y -axis ($B_{X/Y} = \sqrt{B_X^2 + B_Y^2}$ with $B_{X/Y,\max} = \sqrt{B_{X,\max}^2 + B_{Y,\max}^2} = \sqrt{(1\text{ T})^2 + (1\text{ T})^2} \approx 1.41\text{ T}$). A maximum range bipolar sweep of field strength in the X/Y plane has no effect on the TWPA gain (see left panel of Figure 3.4(b)). However, for fields along the Z -axis the TWPA stops working and strongly attenuates signals when $|B_Z| \gtrsim 2.1\text{ T}$ (see middle and right panel of Figure 3.4(b)), indicating a breakdown of the magnetic shielding around the TWPA. Due to the mounting location of the TWPA, the relation between magnetic fields in the sample space and stray fields at the TWPA location is non-trivial and results may vary for field directions other than the ones tested here. However, as a rule of thumb it seems reasonable that fields from the vector magnet should not exceed 2 T during TWPA operation.

After a breakdown of the TWPA magnetic shielding, reducing the magnetic field below the breakdown threshold is not sufficient for restoring positive amplifier gain. This is likely due to flux trapping in the proximity of the amplifier. A thermal cycle of the cryostat to 10 K (i.e., above the critical temperature of niobium) recovers the amplifier.

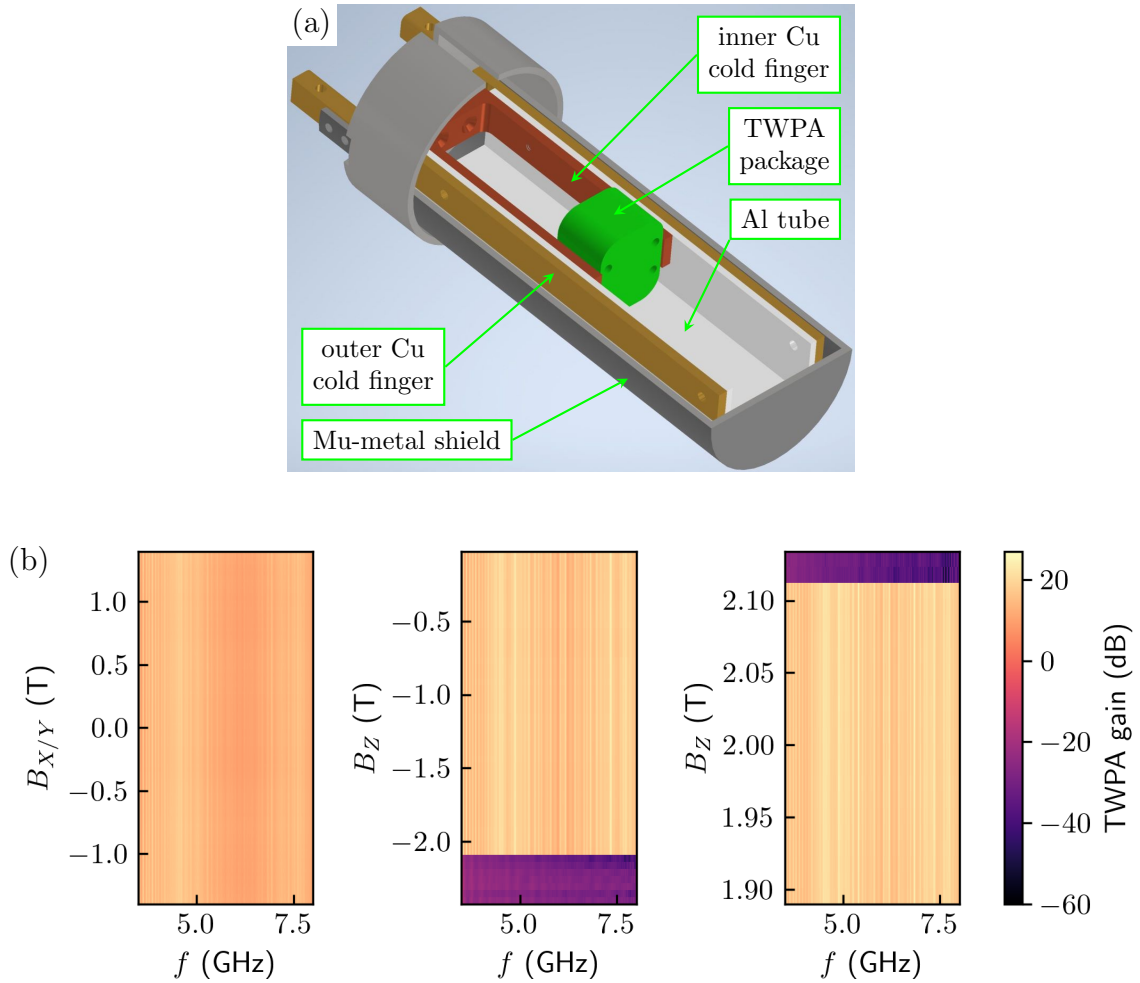


Figure 3.4: Simultaneous operation of the TWPA and superconducting vector magnet. (a) CAD model of the installed TWPA shielding. The amplifier was shipped in a package made from Cu and Al parts. It is mounted inside an Al square tube, which sits inside a Mu-metal shield, providing two layers of shielding against external magnetic fields. The amplifier package and Al tube are thermally anchored to the MC stage via Cu cold fingers. (b) TWPA gain during operation of the cryostat’s superconducting vector magnet. Left: A full range sweep of the magnetic field along the diagonal of the X/Y plane has no effect on the TWPA. Middle: When the field strength is increased in the direction of $-Z$, the magnetic shielding of the TWPA breaks down for $B_z < -2.09$ T. Right: The magnetic shielding also fails for $B_z > 2.11$ T. When the TWPA is exposed to external magnetic fields, signals are strongly attenuated.

3.4 Y-factor measurement for characterisation of a cryogenic low-noise amplifier

As a final step in the characterisation of our TWPA we shall quantify the noise performance of the amplifier. This can be expressed as noise temperature T_{TWPA} , i.e., the noise added to a signal by the amplifier is equivalent to the noise emitted by a matched resistor thermalized at T_{TWPA} . A common way of measuring the noise temperature of a device under test (DUT) is the so-called Y-factor method [26]. This is carried out by successively connecting two matched load resistors with vastly different temperatures T_1 and T_2 ($T_1 \gg T_2$) to the DUT input and measuring the noise powers N_1 and N_2 , respectively, at the DUT output in a specified bandwidth using a spectrum analyser. The Y-factor is then defined as the ratio of the measured noise powers $Y = N_1/N_2$. Finally, the noise temperature of the DUT is obtained using $T_{\text{DUT}} = (T_1 - YT_2)/(Y - 1)$.

Applying the Y-factor method to low-noise amplifiers in a millikelvin environment poses a number of challenges [27]. First, when switching between the hot and cold load (e.g., matched terminators mounted to different stages of the cryostat and connected to the DUT through a coax switch) slight impedance mismatches in the setup can lead to systematic errors. Second, additional errors can be introduced if the loads are poorly thermalized. Third, uncertainties in the load temperatures can lead to fitting errors, which is especially relevant if the noise temperature of the DUT is close to the temperature of the cold load. Finally, as a practical challenge, cold loads suitable for millikelvin environments and DUT noise temperatures of a few Kelvin or less are not readily available, requiring custom built components. We avoid most of these challenges by following a procedure similar to the one presented by S. Simbierowicz *et al.* [27].

Instead of hot and cold loads, we use a single custom built, $50\ \Omega$ matched temperature-variable noise source. The design is presented in Figure 3.5(a). Core elements of the noise source are a stainless steel 30 dB attenuator, a resistive heater cartridge and a ruthenium oxide thermometer, all clamped to a copper block for thermal connection between them. The thermometer is calibrated against the factory installed ruthenium oxide thermometer on our cryostat’s mixing chamber stage. Using the heater and thermometer we can control the temperature of the Cu body and attenuator, resulting in emission of thermal noise with a well known equivalent temperature from the attenuator into the attached coax line. For the experiment presented here, the noise source assembly is attached to the cryostat mixing chamber stage with a brass mounting bracket. Coax cables connect both ends of the attenuator to SMA bulkheads on the mounting bracket. Having an attenuator as

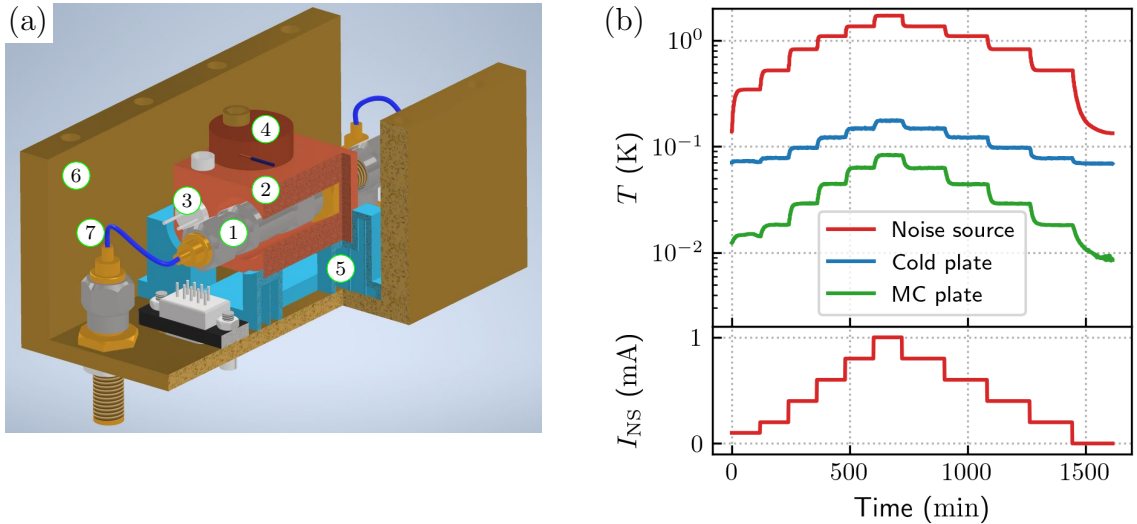


Figure 3.5: Matched temperature-variable noise source. (a) Cross section view of CAD model (design by S. Henderson). A 30 dB attenuator (1) is connected to an SMA bulkhead threaded into a Cu block (2). A heater (3) and thermometer (4) are also attached to the block. A 3d printed ABS plastic spacer (5) separates the Cu body from the brass mounting bracket (6) for thermal isolation. Superconducting semi-rigid NbTi coax cables (7) connect the noise source to the MW ports on the mounting bracket and simultaneously act as thermal weak links. (b) Noise source, cold plate and mixing chamber temperatures (top panel) for various noise source heater currents (bottom panel). Thermal time constant is on the order of 5 s for higher temperatures and 23 s for the last step in this test.

core component of the noise source instead of a terminator allows two modes of operation for the noise source, either transmission of a probe tone, or as a single ended noise source. Here we will only use the latter.

To minimise unwanted heating of nearby areas of the cryostat, a 3d printed ABS plastic spacer is mounted between the noise source Cu body and brass mounting bracket for thermal insulation. J. Chawner *et al.* [28] previously reported excellent thermal insulator performance of ABS plastic blocks at millikelvin temperatures. Heat leaks are further reduced by using semi-rigid NbTi coax cables for the connections from the attenuator to the SMA bulkheads, taking advantage of the low thermal conductivity of superconductors.

Temperature characteristics, together with impact on temperatures of nearby cryostat stages, are shown in Figure 3.5(b). With the cryostat at base temperature and the noise source mounted to the mixing chamber stage the noise source base temperature is approximately 130 mK. With heater currents I_{NS} up to 1 mA (note that this limit for the heater current was arbitrarily chosen) applied from a Keithley 2450 SourceMeter the noise source temperature covers a range of 0.13–1.7 K with reasonably little impact on cryostat temperatures (mixing chamber temperature remains below 85 mK). This provides enough range to characterise both near-quantum

limited amplifiers and low-noise HEMT amplifiers. From the steps in [Figure 3.5\(b\)](#) we extract a thermal time constant for the noise source on the order of 5 s for higher temperatures and > 20 s for noise source temperatures below 800 mK. If necessary, the thermal weak link between the cryostat and noise source could be adjusted by, for example, swapping the NbTi coax cables between the attenuator and SMA bulk-heads for cables with different length or diameter. Any such adjustment would have to strike an acceptable balance between the noise source thermal time constant and heating of the cryostat.

The physical temperature of the noise source T_{bath} determines the equivalent temperature of the emitted thermal noise T_{NS} . In the classical regime ($k_{\text{B}}T_{\text{bath}} \gg hf$, where k_{B} is the Boltzmann constant, h the Planck constant and f the signal frequency), we can assume $T_{\text{bath}} \approx T_{\text{NS}}$. In the quantum regime ($k_{\text{B}}T_{\text{bath}} \lesssim hf$) the following correction needs to be applied [27]:

$$T_{\text{NS}} = \frac{hf}{2k_{\text{B}}} \coth \frac{hf}{2k_{\text{B}}T_{\text{bath}}} \quad (3.2)$$

For best accuracy in the following experiments, we always apply this correction to all noise source temperatures. The noise power emitted by the noise source within a certain bandwidth B is then given by [26]

$$N_{\text{NS}} = k_{\text{B}}T_{\text{NS}}B \quad (3.3)$$

We now perform a variation of the Y-factor method to characterise the noise performance of the TWPA. Schematics of the setup are shown in [Figure 3.6\(a\)](#). We feed the output of our noise source into the MW readout line of the cryostat. After further amplification at room temperature (Narda LNA-30-04001200-15-10P low-noise amplifier, gain ~ 38 dB) the noise power is measured using a Rohde & Schwarz FSV3044 spectrum analyser with the measurement bandwidth set to $B = 1$ MHz. We can express the noise power detected by the spectrum analyser in terms of noise temperature contributions of individual components as [26]

$$P_{\text{out}} = G_{\text{sys}}k_{\text{B}}B \left(T_{\text{NS}} + T_{\text{TWPA}} + \frac{T_{\text{HEMT}}}{G_{\text{TWPA}}} + \frac{T_{\text{bkg}}}{G_{\text{TWPA}}G_{\text{HEMT}}} \right) \quad (3.4)$$

where G_{sys} is the combination of amplifier gains and component losses of the entire circuit, G_{TWPA} (G_{HEMT}) and T_{TWPA} (T_{HEMT}) are the gain and noise temperatures of the TWPA (HEMT), respectively, and T_{bkg} represents all additional noise contributions from components after the HEMT at higher temperatures. By combining all terms except the noise source temperature in the sum in [Equation \(3.4\)](#) into an

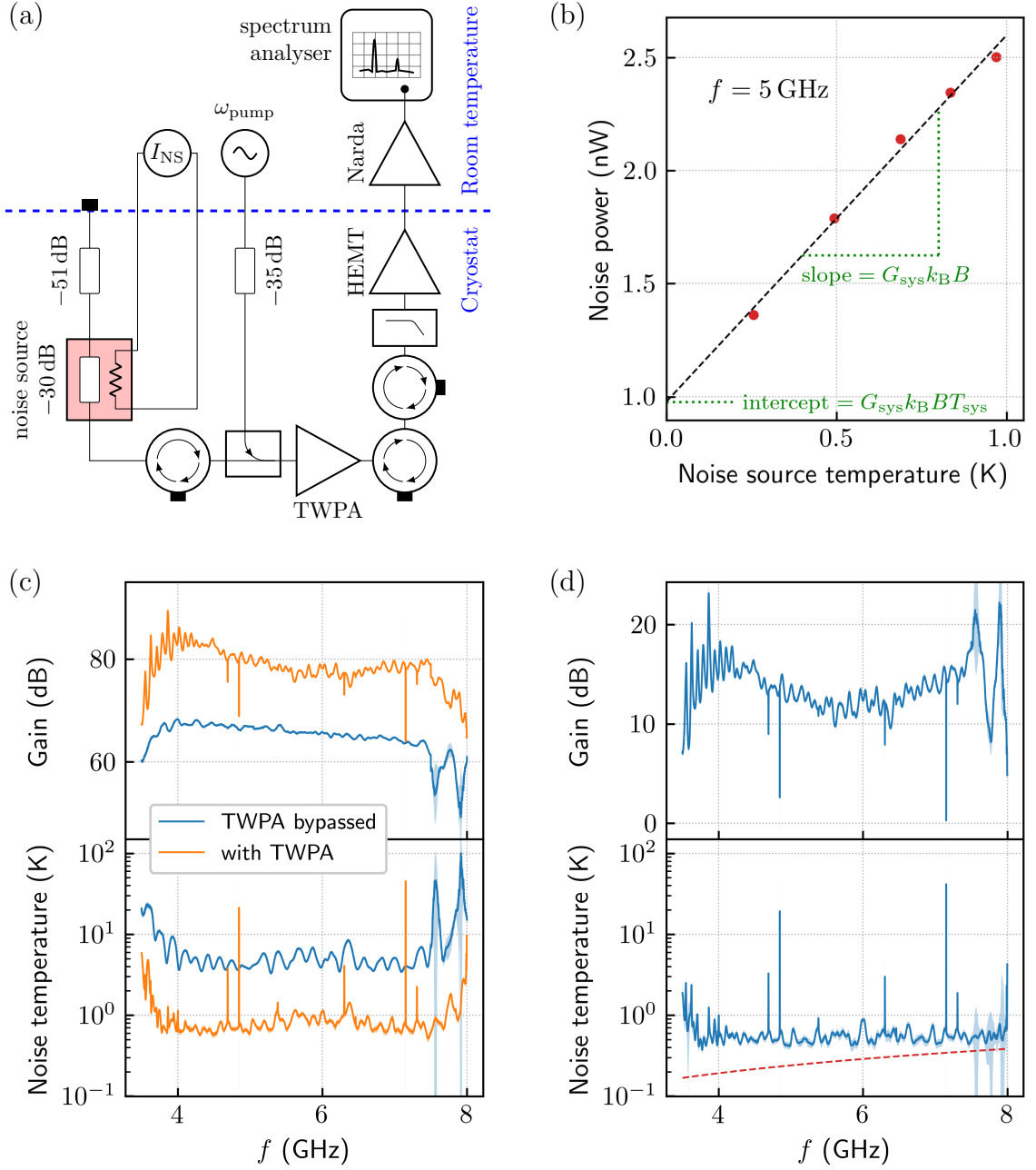


Figure 3.6: Noise temperature measurement of the TWPA. (a) Schematic of the setup. The output of the noise source is fed into the MW readout circuitry. An additional low-noise amplifier is added at room temperature. (b) Noise power detected at the spectrum analyser ($f = 5$ GHz, resolution bandwidth: 1 MHz) as a function of noise source temperature. Red circles are measurement results, the dashed black line is a linear fit to the data. (c) Gain and noise temperature of the MW readout circuit extracted from fits similar to (b) across the whole MW readout band. Shown in blue are results from a calibration run with the TWPA bypassed. Orange curves are results of a similar measurement, but with the TWPA included in the circuit. (d) Gain and noise temperature of the TWPA, extracted by comparing results of the two measurement runs in (c). The dashed red line marks the single-photon quantum limit. Shaded areas in (c) and (d) indicate uncertainties from fitting.

effective system noise temperature

$$T_{\text{sys}} = T_{\text{TWPA}} + \frac{T_{\text{HEMT}}}{G_{\text{TWPA}}} + \frac{T_{\text{bkg}}}{G_{\text{TWPA}}G_{\text{HEMT}}} \quad (3.5)$$

we can rewrite P_{out} as

$$P_{\text{out}} = G_{\text{sys}}k_{\text{B}}B(T_{\text{NS}} + T_{\text{sys}}) \quad (3.6)$$

We record P_{out} for a number of different noise source temperatures T_{NS} . To avoid saturation of the TWPA, we operate the noise source at relatively low temperatures $T_{\text{bath}} < 1$ K. Using Equation (3.6), we can extract G_{sys} and T_{sys} from the slope and intercept of linear fits to the data. An example fit for a signal frequency of 5 GHz is shown in Figure 3.6(b). Repeating this procedure for many signal frequencies, we can map the system gain and noise temperature across the whole MW readout band. The result is shown as orange curves in Figure 3.6(c). Note the sharp peaks (dips) that appear in the noise temperature (gain). Interestingly, most of these peaks can be paired up so that the sum of the frequencies of the pair equals the TWPA pump frequency. Presumably, these are signals created in the TWPA via some (unwanted) non-linear processes.

Next we collect a calibration dataset for the noise performance of the system without the TWPA. To do this, we repeat the experiment, but this time replacing the TWPA with a piece of coax cable. With the TWPA removed Equation (3.6) turns into the form

$$P_{\text{out, cal}} = G_{\text{cal}}k_{\text{B}}B(T_{\text{NS}} + T_{\text{cal}}) \quad (3.7)$$

with

$$G_{\text{cal}} = \frac{G_{\text{sys}}}{G_{\text{TWPA}}} \quad (3.8)$$

$$T_{\text{cal}} = T_{\text{HEMT}} + \frac{T_{\text{bkg}}}{G_{\text{HEMT}}} \quad (3.9)$$

We determine G_{cal} and T_{cal} following the procedure we used for G_{sys} and T_{sys} during the first run of the experiment. The result is shown as blue curves in Figure 3.6(c). The gain G_{cal} we find with this method is a reasonably close match to the gain of the MW readout line we measured in Figure 2.3 plus the gain of the room temperature amplifier that was added for this experiment. The noise temperature T_{cal} should be dominated by noise from the HEMT, but is slightly higher than the values stated in the HEMT datasheet. Simbierowicz *et al.* [27] find that such discrepancies can be explained by contributions from the filter and circulators in the circuit.

By comparing the dataset of the calibration run with the initial results for the full system, and using Equations (3.5), (3.8) and (3.9), we can isolate the TWPA

noise performance as

$$G_{\text{TWPA}} = \frac{G_{\text{sys}}}{G_{\text{cal}}} \quad (3.10)$$

$$T_{\text{TWPA}} = T_{\text{sys}} - \frac{T_{\text{cal}}}{G_{\text{TWPA}}} \quad (3.11)$$

The results are shown in [Figure 3.6\(d\)](#). Comparing G_{TWPA} from this method with the TWPA gain measured with a VNA in [Section 3.2](#) we find a good match, except for a slightly different pattern of gain ripple. This difference could be caused by a slight mismatch in flux bias tuning of the TWPA between the two experiments. The smallest noise temperature we find for the TWPA is 0.41 ± 0.04 K for $f = 4.988\,775$ GHz. Converting this to an equivalent photon number we find $n = k_{\text{B}}T_{\text{TWPA}}/hf = 1.7 \pm 0.2$, which is close to the single-photon quantum limit indicated by the dashed red line in [Figure 3.6\(d\)](#). Across the MW readout band we find values of n in the range 1.2 to 18.9, with the mean at $\bar{n} = 2.1$.

From [Equation \(3.4\)](#) we can see that noise performance of a cascaded system is dominated by the first stage, since the effect of later stages is reduced by the gain of preceding stages. Thus, having a first gain stage that adds minimal noise and has at least moderate gain is important for achieving best overall system performance. We had already seen in [Section 3.2](#) that addition of the TWPA to the experimental setup improved SNR. Comparing the results of the calibration and measurement runs of the Y-factor measurement in [Figure 3.6\(c\)](#) we can confirm again that the TWPA adds a moderate boost to the system gain and significantly reduces the system noise temperature. Comparing the system noise temperature in [Figure 3.6\(c\)](#) with the extracted TWPA noise temperature in [Figure 3.6\(d\)](#) we can see that the near-quantum limited TWPA now indeed dominates the noise performance of the system, with only a small contribution from other components.

BLANK PAGE

Chapter 4

Carbon nanotube nanoelectromechanical systems

CNTs are cylindrical macromolecules that resemble rolled up sheets of graphene. Therefore, they count among the allotropes of carbon, like graphene, graphite, diamond, fullerenes and many others [29].

Since the discovery of tubular carbon structures⁵, and especially since the discovery of single-wall CNTs in 1993 [31, 32]⁶, carbon nanotubes have attracted attention from a number of different fields in research and industry due to their exceptional properties. Their low density combined with their high tensile strength, elastic modulus and thermal and electrical conductivity make them interesting for material science and composite materials [33–37]. CNTs can be created in dense, vertically self-aligned arrays. These *CNT forests* are appealing for applications that need materials with a large surface area, but have also shown potential for a number of other applications [38]. At room temperature, devices made from CNT thin films or individual CNTs show excellent transistor attributes [39–42]. When cooled to cryogenic temperatures, suspended CNTs act as mechanical resonators with low mass, high compliance and exceptionally high quality factors [13, 43–45], which is desirable for optomechanics experiments [46–49]. Both electrical and mechanical properties of carbon nanotubes lend themselves to construction of CNT-based sensors, including various types of gas [50], biological and chemical sensors [51], as well as sensors for electric and magnetic fields [52]. Due to their very large aspect ratio, CNTs also

⁵The history of multi-wall carbon nanotubes is somewhat convoluted, in parts even controversial, and potentially extends back to times before nanomaterials became a hot topic. For a more in depth attempt of unravelling the history of CNTs see [30].

⁶Credit for the discovery of single-wall CNTs is much less controversial than in the case of multi-wall CNTs. Single-wall CNTs were first reported in 1993 in two independent papers, one by S. Iijima and T. Ichihashi at NEC, Japan [31], the other by D. S. Bethune *et al.* at IBM, California [32].

act as quasi-one dimensional conductors at low temperatures. They can have a very low density of structural defects, which leads to highly regular systems and allows the formation of quantum dots (QDs) when a short CNT segment is contacted with metallic electrodes.

The work presented in this thesis focuses solely on CNT NEMS devices made from individual suspended ultraclean single-wall carbon nanotubes (SWCNTs). In this chapter we shall derive some fundamental properties of CNTs from the molecular and electronic structure of graphene. We then outline a process for fabricating the type of device used in this work in a cleanroom. We shall also describe a model that predicts the electronic properties of this type of device at cryogenic temperatures. Furthermore, we explore the mechanical properties of a suspended nanotube segment, particularly transversal vibrations, and discuss ways of detecting, driving and tuning resonant modes of said vibrations by means of capacitive coupling to a gate electrode and measurements of electron transport. Lastly we shall briefly discuss some interactions between the electronic and mechanical subsystems of such a device.

4.1 Fundamental properties of carbon nanotubes

4.1.1 Structure of carbon nanotubes

For visualising the physical structure of carbon nanotubes it is helpful to start from a sheet of graphene, which itself is another famous carbon based nano-material with a range of applications in research and industry [53, 54].

Graphene is a two-dimensional material made up of carbon atoms arranged on a hexagonal honeycomb lattice as shown in Figure 4.1(a). The insert of Figure 4.1(a) shows the unit cell of graphene, which contains two atoms and is spanned by the lattice vectors

$$\mathbf{a}_1 = \left(\frac{\sqrt{3}}{2}, \frac{1}{2} \right) a \quad ; \quad \mathbf{a}_2 = \left(\frac{\sqrt{3}}{2}, -\frac{1}{2} \right) a \quad (4.1)$$

with lattice constant $a = \sqrt{3}a_0 = 2.46 \text{ \AA}$, where $a_0 = 1.42 \text{ \AA}$ is the carbon-carbon bond length in graphene [53]. Since the unit cell contains two atoms, the lattice can also be described as two inequivalent interleaving sublattices, labelled A and B. Both sublattices are hexagonal Bravais lattices.

Let us now choose a linear combination of graphene lattice vectors

$$\mathbf{C} = n\mathbf{a}_1 + m\mathbf{a}_2 \quad \text{with} \quad n, m \in \mathbb{N} \quad (4.2)$$

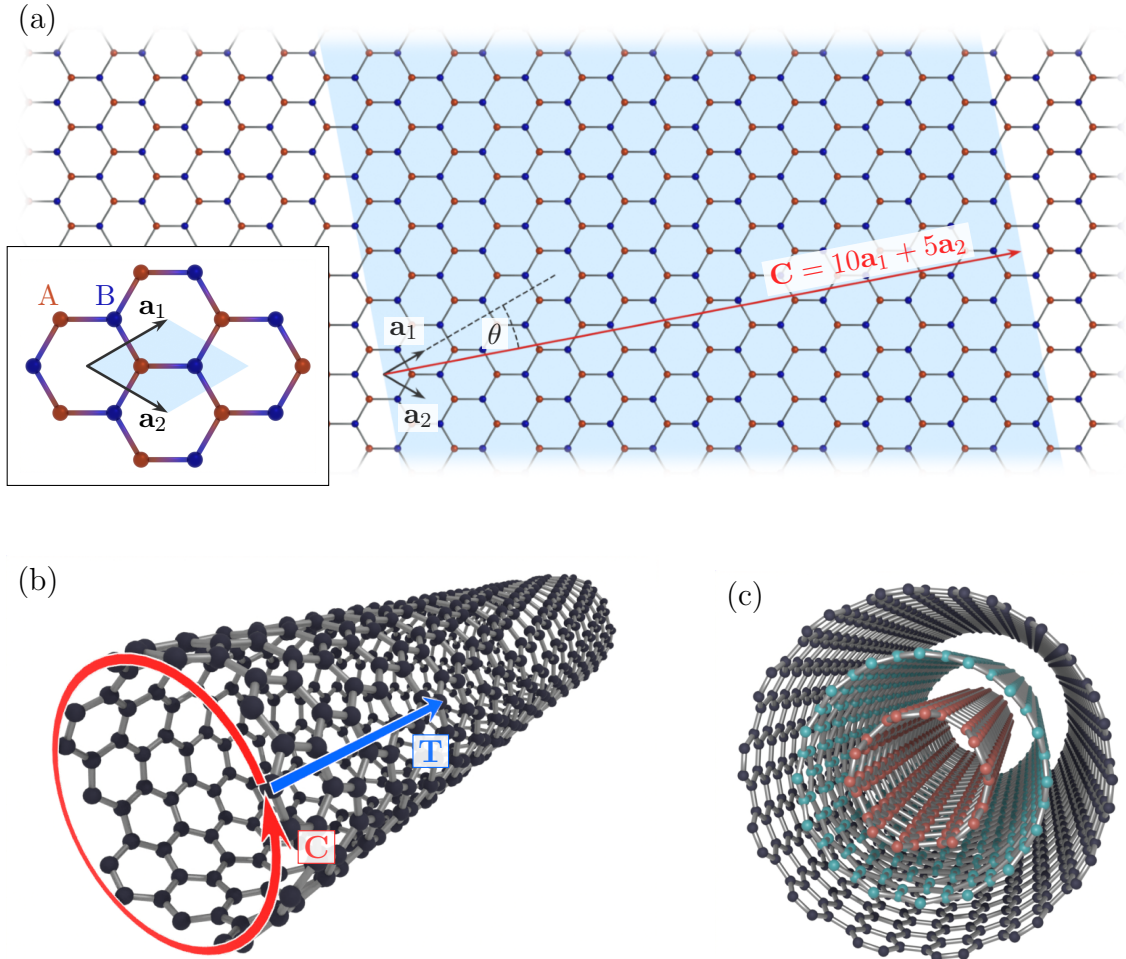


Figure 4.1: Derivation of the structure of carbon nanotubes from graphene. (a) Carbon atoms arranged on a honeycomb lattice form a sheet of graphene. Atoms belonging to the sublattices A and B (see main text) are drawn in red and blue, respectively. The shaded area marks a graphene ribbon that can be “rolled up” into a nanotube. Its width is given by the chiral vector $\mathbf{C} = n\mathbf{a}_1 + m\mathbf{a}_2$. The angle θ between \mathbf{C} and \mathbf{a}_1 is called the chiral angle of the nanotube. Inset: the graphene unit cell contains two carbon atoms and is spanned by lattice vectors \mathbf{a}_1 and \mathbf{a}_2 . (b) The graphene ribbon from (a) “rolled into” a single-wall carbon nanotube. The nanotube unit cell is defined by the chiral vector \mathbf{C} and translation vector \mathbf{T} . (c) A multi-wall carbon nanotube, formed from a concentric arrangement of multiple SWCNTs. For better visibility each shell is drawn in a different colour.

We shall call this new vector \mathbf{C} the chiral vector. Imagine a ribbon of graphene of width $|\mathbf{C}|$ that runs perpendicular to \mathbf{C} (shaded area in Figure 4.1(a)). This ribbon can be rolled into a seamless cylinder with the cylinder axis running perpendicular to \mathbf{C} (Figure 4.1(b)). Such a “graphene cylinder” is called a single-wall carbon nanotube (SWCNT). A concentric arrangement of multiple nanotubes as shown in Figure 4.1(c) is a multi-wall carbon nanotube (MWCNT).

Note that the circumference of a SWCNT is given by the length of \mathbf{C} , and thus its diameter is

$$d = \frac{|\mathbf{C}|}{\pi} = \frac{a}{\pi} \sqrt{n^2 + m^2 + nm} \quad (4.3)$$

Typical diameters range from 0.7 nm to 2.5 nm [53]. For smaller diameters the curvature of the cylinder surface induces too much strain on the C–C bonds, preventing formation of a stable structure. For larger diameters, collapse of the perfectly cylindrical structure into a “flattened” nanotube is energetically favourable, since the energy saving from van der Waals interaction between opposite walls can outweigh the added strain from deformation near the edge of the collapsed tube.

The chiral vector defined in Equation (4.2) completely describes the structure of its corresponding SWCNT and contains enough information to predict the nanotube’s properties. An abbreviated nomenclature has been established, where a nanotube is identified by the pair of chiral indices (n, m) that defines its chiral vector. For example, the CNT shown in Figure 4.1(b) is a $(10, 5)$ nanotube (i.e, its chiral vector is $\mathbf{C} = 10\mathbf{a}_1 + 5\mathbf{a}_2$). Alternatively, a CNT can be identified by its chiral angle, which is the angle between the graphene lattice vector \mathbf{a}_1 and the chiral vector, given by

$$\cos \theta = \frac{\mathbf{C} \cdot \mathbf{a}_1}{|\mathbf{C}| |\mathbf{a}_1|} = \frac{2n + m}{2\sqrt{n^2 + m^2 + nm}} \quad (4.4)$$

Due to the hexagonal symmetry of graphene, all possible SWCNTs can be described with a chiral angle in the range $0^\circ \leq \theta \leq 30^\circ$.

Depending on their chiral indices (n, m) (chiral angle θ), SWCNTs can be divided into three subclasses. A nanotube with indices (n, n) ($\theta = 30^\circ$) is an *armchair* SWCNT, a nanotube with indices $(n, 0)$ ($\theta = 0^\circ$) is a *zigzag* SWCNT and any other indices (n, m) with $n \neq m$ ($0^\circ < \theta < 30^\circ$) describe *chiral* SWCNTs. See Figure 4.2 for examples of the different chirality classes. We can see that the names “armchair” and “zigzag” refer to the cross section of the graphene lattice along the nanotube circumference (highlighted edges in Figure 4.2(a) and (b)).

To fully define the unit cell of a SWCNT, we need two lattice vectors, one of which is the chiral vector. The second lattice vector is the translation vector \mathbf{T} . It is the shortest connection between two graphene lattice points perpendicular to \mathbf{C} (i.e., parallel to the nanotube axis). Hence, like the chiral vector, \mathbf{T} can be written

as a linear combination of graphene lattice vectors:

$$\mathbf{T} = t_1 \mathbf{a}_1 + t_2 \mathbf{a}_2 \quad \text{with} \quad t_1, t_2 \in \mathbb{N} \quad (4.5)$$

Using Equation (4.1) and the condition $\mathbf{C} \cdot \mathbf{T} = 0$, we can find expressions for t_1 and t_2 :

$$t_1 = \frac{2m + n}{p} \quad ; \quad t_2 = -\frac{2n + m}{p} \quad (4.6)$$

where p is the greatest common divisor of $(2m + n)$ and $(2n + m)$.

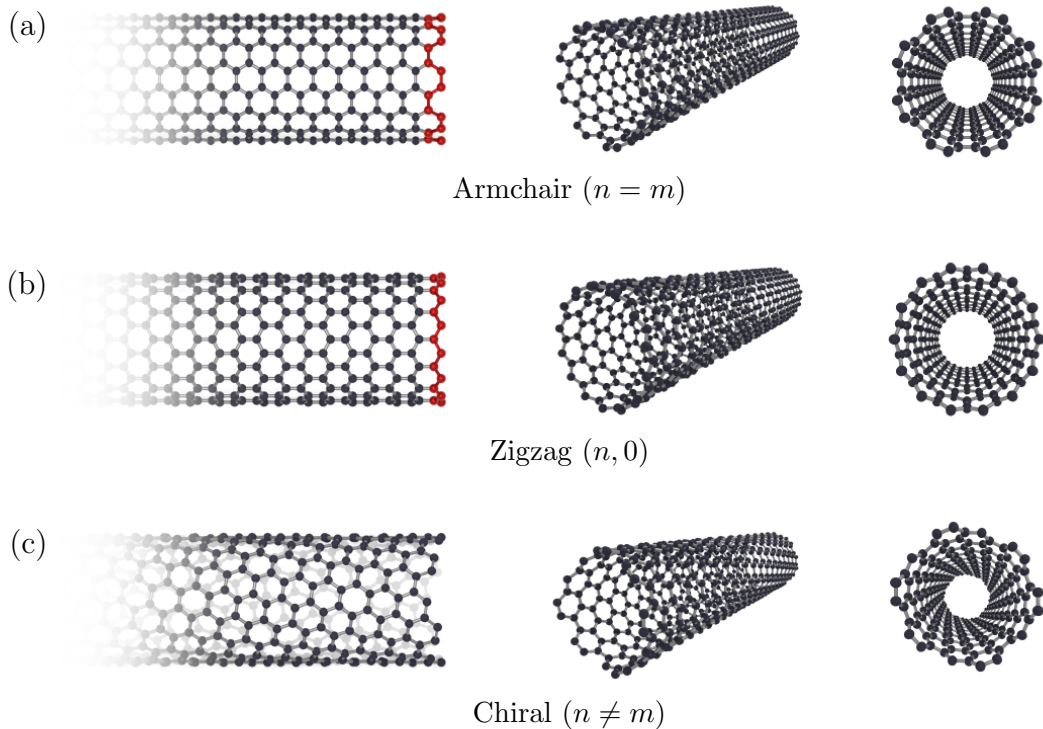


Figure 4.2: Chirality classes of carbon nanotubes. Left to right: orthogonal projection perpendicular to the CNT axis, 3D view and view along the nanotube axis. The examples shown are (a) an (8, 8) armchair CNT, (b) a (14, 0) zigzag CNT and (c) a (10, 6) chiral CNT. Note the patterns of carbon atoms highlighted in red along the CNT circumference in (a) and (b), which give rise to the names of the armchair and zigzag classes.

4.1.2 Carbon nanotube band structure

Following chapter 3 of [55] and chapters 3 and 5 of [53] we can come up with an excellent approximation for describing the band structure of carbon nanotubes. To do this, we first briefly outline a method for modelling the dispersion relation of graphene. Just like in the case of physical structure in the previous section, we then use graphene as a starting point for deriving the band structure of CNTs.

Graphene dispersion relation

We begin with the energy levels of atomic carbon, which has electron configuration $1s^2 2s^2 2p^2$. The outermost atomic shell contains one s orbital and three p orbitals p_x , p_y and p_z . Taking into account the two-fold spin degeneracy of each orbital, four out of the available eight states in the outermost atomic shell are occupied by electrons. The $2s$ - $2p$ energy splitting is small enough to allow hybridisation of all four orbitals in the outermost shell [55]. The degree of hybridisation occurring in a given structure is determined by symmetry. In graphene the $2p_x$ and $2p_y$ orbitals mix with the $2s$ orbital to form three new orbitals in the plane of the graphene sheet. The p_z orbitals remain unhybridised and extend perpendicular to the plane above and below. This configuration is known as sp^2 hybridisation (Figure 4.3(a)).

The atomic orbitals further hybridise across neighbouring atoms to form covalent bonds. The sp^2 atomic orbitals form low-energy (bonding) σ and high-energy (antibonding) σ^* molecular orbitals. Likewise, the unhybridised p_z atomic orbitals form bonding and antibonding molecular orbitals π and π^* , but with a smaller bonding energy due to less interatomic overlap [55]. Figure 4.3(b) shows a comparison of energy levels in atomic carbon and energy bands of graphene molecular orbitals. In undoped graphene, the electrons exactly fill the bonding bands (three electrons per atom in σ , one in π). Because of the large energy gap between the σ and σ^* bands, electrons in the σ band are strongly bound and do not contribute to transport. Thus, the electrical behaviour of graphene is determined almost entirely by the properties of the π and π^* bands.

The basis vectors \mathbf{b}_i to construct the reciprocal lattice of graphene can be found from the real space lattice vectors (Equation (4.1)) using the condition $\mathbf{a}_i \cdot \mathbf{b}_j = \delta_{ij}$, and are given by

$$\mathbf{b}_1 = \left(\frac{1}{\sqrt{3}}, 1 \right) \frac{2\pi}{a} \quad ; \quad \mathbf{b}_2 = \left(\frac{1}{\sqrt{3}}, -1 \right) \frac{2\pi}{a} \quad (4.7)$$

The hexagonal first Brillouin zone is shown in Figure 4.3(c). Its corners are alternately labelled K and K' . All K points are connected by reciprocal lattice vectors and thus, according to Bloch's theorem, correspond to equivalent electronic states. Likewise, all K' points are equivalent to each other. However, K and K' are not equivalent (i.e., cannot be connected by reciprocal lattice vectors), leading to an additional *valley* degree of freedom for the electronic states [55].

By applying tight binding theory in nearest neighbour approximation to the p_z orbitals of the carbon atoms on the graphene lattice, an analytical expression for the dispersion relation $E_{\text{Gr}}(\mathbf{k})$ of the graphene π and π^* bands can be calculated. This approach has been considered by a number of authors over the past few decades

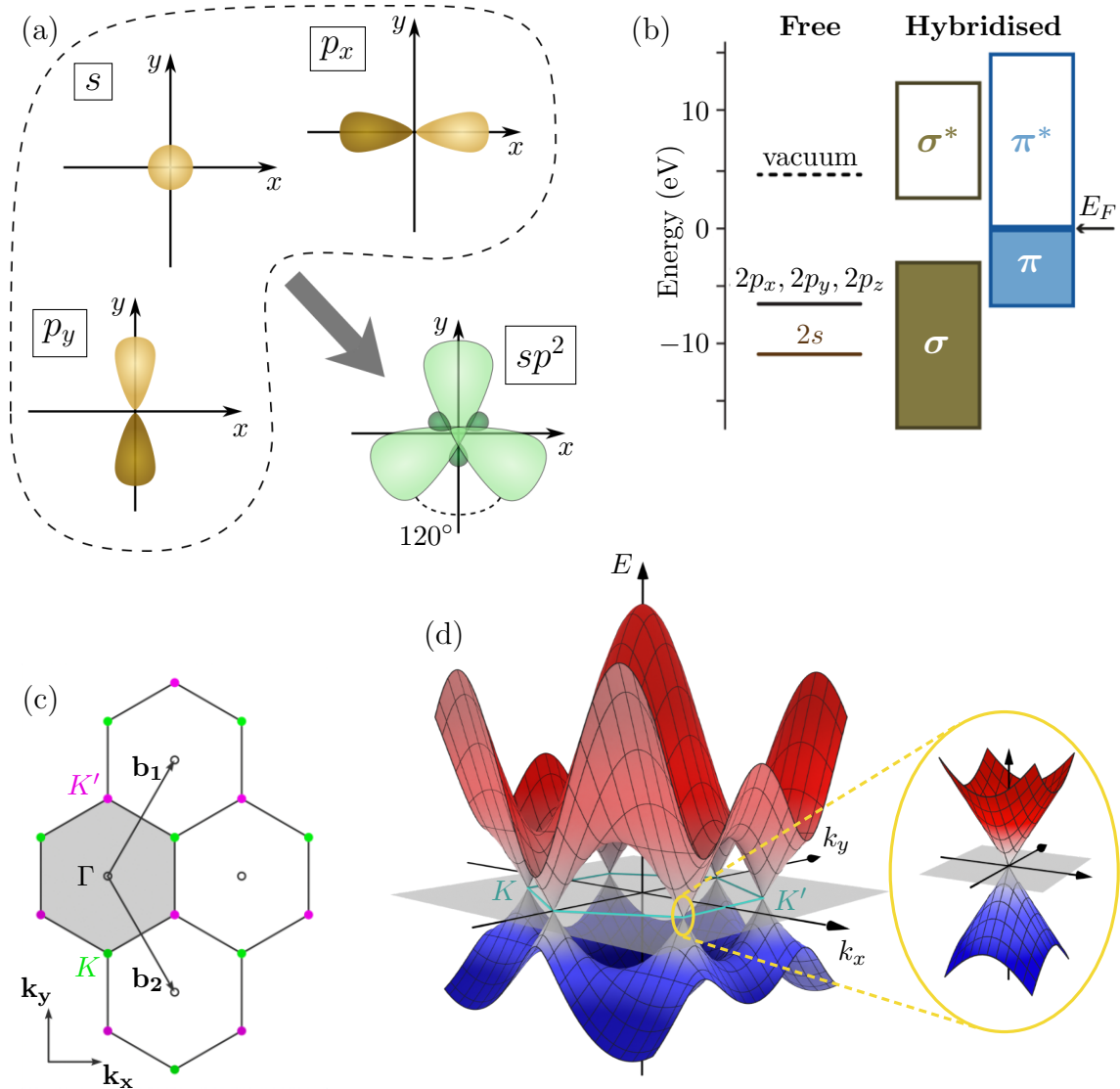


Figure 4.3: (a) sp^2 hybridisation of electron orbitals in the outermost shell of atomic carbon leads to three orbitals in the xy plane with 120° between and the electrons predominantly located on one side of the atom, ready to form covalent bonds with neighbouring atoms on a hexagonal lattice. The p_z orbital (not shown) remains unchanged in sp^2 hybridisation. Light (dark) colours indicate regions where the electron wave function is positive (negative). (b) Schematic energy levels of atomic carbon (left) and electron bands of graphene (right). Energies are referenced to E_F , approximated as the negative of the work function. (c) Segment of the graphene reciprocal lattice. The shaded area is the first Brillouin zone with high symmetry points Γ (centre of Brillouin zone) and K/K' (Brillouin zone corners). \mathbf{b}_1 and \mathbf{b}_2 are the reciprocal lattice vectors. (d) Valence (π , blue) and conduction (π^* , red) bands of graphene. The first Brillouin zone is marked by the cyan hexagon, the grey plane indicates the Fermi level. Inset: At the Brillouin zone corners and for low energies the band structure can be approximated as Dirac cones. (Panel (b) adapted from [55].)

(e.g., [56–59]). We will use the expression given in [57]:

$$E_{\text{Gr}}(\mathbf{k}) = \frac{\epsilon \pm tw(\mathbf{k})}{1 \pm sw(\mathbf{k})} \quad (4.8)$$

$$w(\mathbf{k}) = \sqrt{1 + 4 \cos \frac{\sqrt{3}k_x a}{2} \cos \frac{k_y a}{2} + 4 \left(\cos \frac{k_y a}{2} \right)^2} \quad (4.9)$$

with “+” for the valence band (π) and “-” for the conduction band (π^*). We choose $\epsilon = 0$ to put the arbitrary zero point of energy at the Fermi level. The remaining constants $t = -3.033$ eV and $s = 0.129$ are obtained from detailed analysis of the overlap integrals of the carbon p_z orbitals. These results were calculated prior to the isolation of graphene in 2004 [60], but have since been shown to accurately describe experimentally observed properties of graphene (e.g., [61, 62]).

When we plot the graphene dispersion relation described by Equation (4.8) (Figure 4.3(d)), we can see that it has some quite unusual properties. The conduction and valence bands do not overlap, but they touch at the K and K' points. This makes graphene a zero-bandgap semiconductor. Minimal amounts of thermal energy suffice to excite electrons from the valence band to the conduction band, making graphene a good conductor at any temperature above absolute zero.

To describe the dispersion relation of low-energy charge carriers, we can perform a binomial expansion of Equation (4.9) around the K and K' points. Omitting higher order terms, we get [53, 55, 56]

$$\tilde{E}_{\text{Gr}}(\boldsymbol{\kappa}) \approx \pm \hbar v_0 |\boldsymbol{\kappa}| \quad (4.10)$$

with $v_0 = (1/\hbar)|\nabla_{\mathbf{k}}E|$ the Fermi velocity of graphene and $\boldsymbol{\kappa} = \mathbf{k} - \mathbf{K}$ the distance from a K or K' point in reciprocal space. Since $\tilde{E}_{\text{Gr}}(\boldsymbol{\kappa})$ only depends on the scalar value of $\boldsymbol{\kappa}$, the dispersion relation in this region is conical (see insert of Figure 4.3(d)). The relation between energy and wavevector in this approximation is linear, which means low-energy charge carriers in graphene behave like massless Dirac fermions. This is why the K and K' points of the graphene Brillouin zone are also known as Dirac points.

Zone folding approximation for carbon nanotube dispersion relation

We will now use the graphene dispersion relation to model the electronic dispersion of SWCNTs by applying what is known as the *zone folding approximation*. This approach has some limitations, which we will briefly discuss later in this section, but the resulting model already describes many properties of CNTs.

Let us assume that, since the spacing between carbon atoms typically is much

smaller than the nanotube diameter, the graphene dispersion remains to a good approximation unperturbed by rolling a sheet of graphene into a nanotube. However, the small diameter of a CNT imposes a periodic boundary condition on the electron wavevector component k_{\perp} along the nanotube circumference [63, 64]. To ensure single valuedness of the electron wave function, \mathbf{k} must fulfil the condition

$$\mathbf{k} \cdot \mathbf{C} = 2\pi p \quad (4.11)$$

with an integer p , i.e., the component of \mathbf{k} perpendicular to the nanotube axis is

$$k_{\perp} = \frac{2}{d} p \quad (4.12)$$

Thus, \mathbf{k} is now quantised in the direction perpendicular to the nanotube axis. Since the length of a CNT is typically orders of magnitude larger than its diameter, the wavevector component k_{\parallel} in the direction of the nanotube axis remains continuous. With this, allowed \mathbf{k} values correspond to a series of quantisation lines in reciprocal space, running at an angle $\pi/3 + \theta$ from the k_x axis (Figures 4.4(a) and 4.4(b)).

To determine the dispersion relation $E(k_{\parallel})$ of a CNT we sample the graphene dispersion along quantisation lines in reciprocal space. Since the nanotube's transport properties are determined by the branches of the dispersion relation closest to the Fermi level, we will focus on sections of the quantisation lines closest to the Dirac points and neglect all other branches. From Figure 4.4 we can see that there are two types of possible nanotubes. If the quantisation lines intersect a Dirac point, the CNT valence and conduction bands touch at the Fermi level (Figure 4.4(a) and 4.4(c)), the nanotube has zero bandgap, and is referred to as *metallic* type. In contrast, if the quantisation lines miss the Dirac points, a gap opens in the CNT's band structure and the nanotube is of *semiconducting* type (Figure 4.4(b) and 4.4(d)). By substituting the \mathbf{k} vector of a Dirac point into Equation (4.11) we get a simple rule for predicting the nanotube type: If the difference of chiral indices $n - m$ is a multiple of 3 the nanotube is metallic, otherwise it is semiconducting [53, 63, 64]. Note that all armchair ($n = m$) SWCNTs are metallic, and zigzag nanotubes ($m = 0$) are metallic whenever n is divisible by three.

As previously discussed, we can use Dirac cones as approximation for the dispersion relation of low energy charge carriers in graphene (Equation (4.10)). Then the dispersion relation of a CNT is a hyperbola and we can find expressions for the bandgap, Fermi velocity and charge carrier effective mass. The results are summarised in Table 4.1.

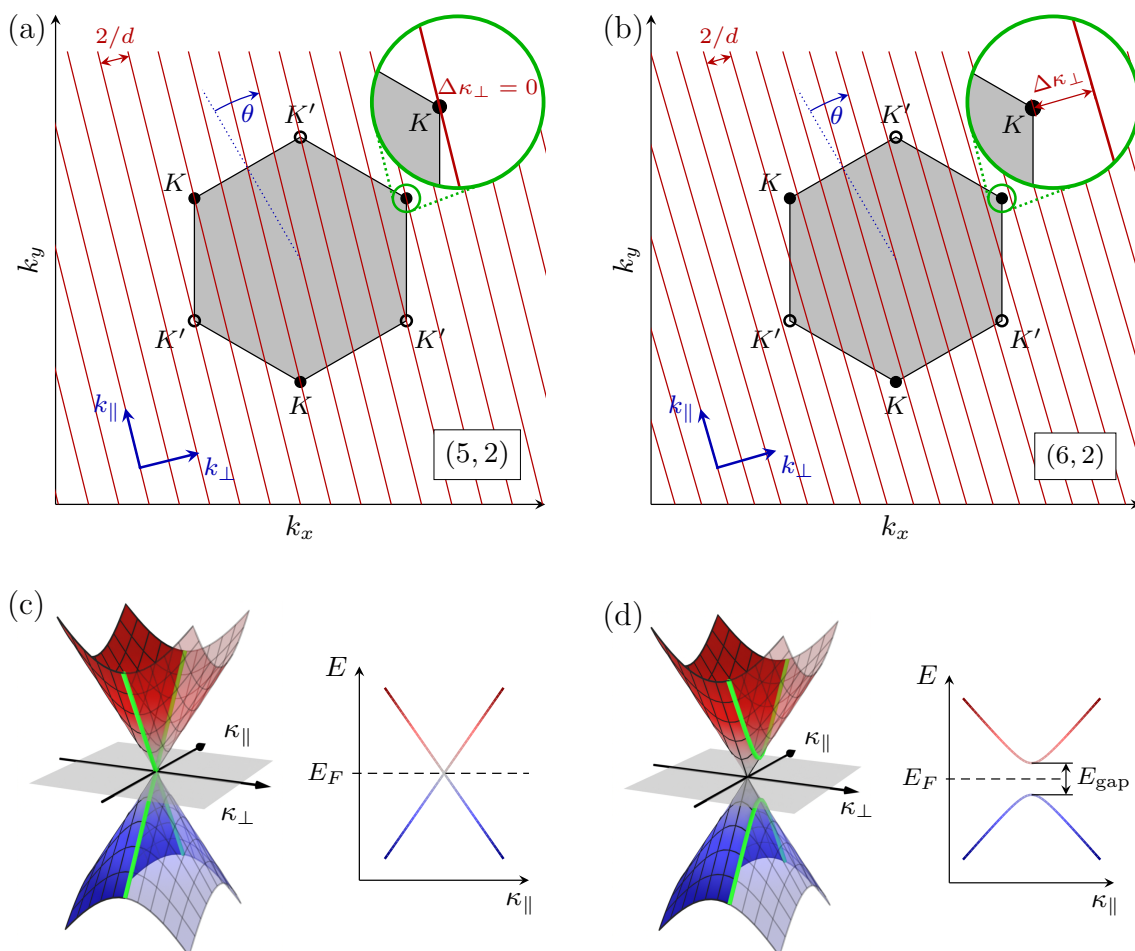


Figure 4.4: CNT band structure in zone folding approximation. (a), (b) Quantisation lines overlaid on the graphene Brillouin zone. Periodic boundary conditions along the CNT circumference constrain \mathbf{k} to lie on these lines. The indicated $\{k_{\perp}, k_{\parallel}\}$ axes in reciprocal space correspond to motion around and along the nanotube. (c), (d) For low energy charge carriers the CNT band structure is determined by sections of the graphene Dirac cones along quantisation lines. If a quantisation line intersects a Dirac point, the nanotube is metallic, i.e., its dispersion relation is linear and it has no bandgap ((a) and (c)). Otherwise the nanotube is semiconducting, with a finite bandgap and hyperbolic dispersion relation ((b) and (d)). (Adapted from [55].)

name	symbol	method	value
Graphene			
full dispersion	$E_{\text{Gr}}(\mathbf{k})$	[1]	Eq. (4.8), (4.9)
low energy Dirac cones	$\tilde{E}_{\text{Gr}}(\boldsymbol{\kappa})$	[2]	$\pm \hbar v_0 \boldsymbol{\kappa} $
Fermi velocity	v_0	$(1/\hbar) \frac{d\tilde{E}_{\text{Gr}}}{d\boldsymbol{\kappa}}$	$(7.8 - 9.8) \times 10^5 \text{ m/s}$ [3]
carrier effective mass	m_{Gr}^*	[4]	[4]
CNT			
bandgap	E_g	$(4\hbar v_0)/(3d)$	$\sim 700 \text{ meV}/d[\text{nm}]$
dispersion	$E_{\text{CNT}}(\kappa_{\parallel})$	[5]	$\pm \sqrt{\hbar^2 v_0^2 \kappa_{\parallel}^2 + E_g/4}$
Fermi velocity	v_{F}	$(1/\hbar) \frac{dE_{\text{CNT}}}{d\kappa_{\parallel}}$	$\hbar v_0^2 \kappa_{\parallel} / E_{\text{CNT}}$
carrier effective mass	m_{CNT}^*	$(1/\hbar^2) \left(\frac{d^2 E_{\text{CNT}}}{d\kappa_{\parallel}^2} \right)^{-1}$	$\sim \frac{E_g}{7.3 \text{ eV}} \times m_e$

Table 4.1: Summary of electronic properties of graphene and SWCNTs [55, 65]. [1]Obtained from tight binding calculations. [2]From binomial expansion of exact dispersion $E_{\text{Gr}}(\mathbf{K})$ around Brillouin zone corners. [3]Values taken from [55] which uses additional sources for results from numerical simulations [66–69] and experiments [70–72] to derive these numbers. [4]In the low energy (Dirac cone) approximation, linear dispersion means that charge carriers behave like massless particles. [5]Section of Dirac cone along CNT quantisation line in reciprocal space.

Limitations of the zone folding approach

When using the zone folding approach to predict a CNT’s electronic properties, we assume that the only differences between flat graphene and a nanotube are quantum confinement of electrons along the nanotube circumference and the resulting quantisation of the electron wavevector in that direction. In most experimental contexts this is a reasonably good approximation, since it accurately describes many observed properties of CNTs. Therefore, we will use this model throughout the rest of this work. Nonetheless, we shall at least mention some of the most important effects that arise from going beyond the zone folding approximation and provide some references where more detail can be found.

Rolling a sheet of graphene into a cylindrical nanotube breaks some symmetries that are found in flat graphene. The carbon-carbon bond length along the circumference gets slightly shortened [53] and the deformation due to the curvature of the nanotube surface results in re-hybridisation of the σ and π bands [53, 55, 73–76]. These additional considerations result in the opening of a small bandgap for many CNTs that were predicted to be metallic in the zone folding approach [55, 74–79]. Only nanotubes with armchair geometry remain as truly metallic [55]. Furthermore, spin-orbit coupling is strongly suppressed by symmetry in flat graphene [55, 80]. Since this symmetry is broken on the curved CNT surface, spin-orbit coupling can be observed in clean nanotubes [81].

Identification of nanotube types at room temperature

The three possible CNT types (metallic, small bandgap or semiconducting) can easily be identified in room temperature conductance measurements if the nanotube forms the conduction channel of a field effect transistor [55]. An applied gate potential shifts the CNT bandgap (if existing) relative to the Fermi level E_F . Tuning E_F into the nanotube bandgap suppresses current flow. This results in the characteristic behaviour shown in Figure 4.5 of the different nanotube types when measuring conductance as a function of gate voltage V_g . In the case of metallic CNTs no dependence on gate voltage is observed due to the absence of a bandgap (Figure 4.5(a)). For semiconducting nanotubes ($k_B T \ll E_g$), current flow is suppressed over a wide range of V_g while E_F is within the bandgap (Figure 4.5(c)). Small bandgap nanotubes ($k_B T \sim E_g$) will show a dip in conductance, but current flow is never suppressed completely (Figure 4.5(b)).

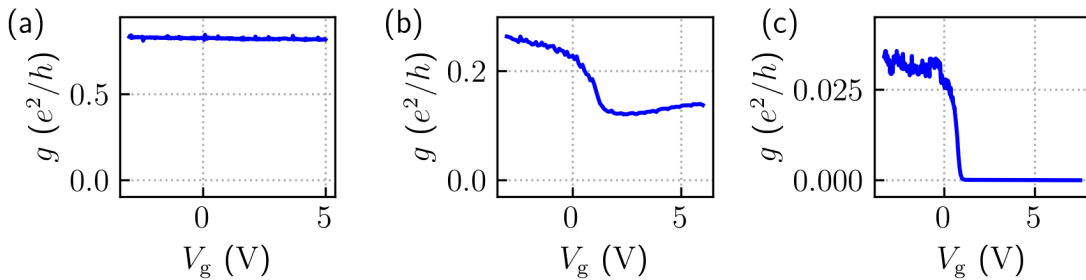


Figure 4.5: Typical room temperature conductance curves for different types of individual SWCNTs. (a) For a metallic nanotube the curve is flat. (b) A small-bandgap nanotube shows a dip in conductance. (c) For a semiconducting nanotube current flow is fully suppressed over a significant range of gate voltage. Panel (a) was measured on a CNT grown on chip over MoRe electrodes⁷, panels (b) and (c) were recorded during transfer of CNTs onto Ti/Au electrodes (see Section 4.2.3).

4.2 Device design and fabrication techniques

4.2.1 Description of the device design

As mentioned in Chapter 1, the motivation for the work presented in this thesis was developing a CNT NEMS based force sensor for MRFM. The general geometry of a CNT NEMS is a carbon nanotube segment suspended across the gap between two metal electrodes (source and drain). The suspended nanotube segment is free to vibrate as a doubly clamped cantilever. Thin finger gates underneath the nanotube or the device substrate can be used to apply gate voltages to the device. For the

⁷Device fabricated by Z. Saadi, data collected by S. Henderson.

device to have potential for being a good force sensor it needs to be built from an ultraclean nanotube, which is difficult enough on its own, as we will see in upcoming sections. For an application in MRFM, we need to attach some material (either the MRFM sample or a magnetic particle) to the suspended CNT segment, which poses an additional fabrication challenge.

We choose the magnet-on-cantilever variety of MRFM detectors for our device. With that, we can solve the issue of material deposition on a CNT only once (for forming a magnetic particle) and hopefully end up with a flexible detector that can be used on many different samples. A sample-on-cantilever configuration bears the risk of having to develop new sample preparation methods for potentially every new sample type. Additionally, a sample-on-cantilever approach would require a new CNT NEMS device for every sample, which seems highly unpractical, given the complexity of CNT NEMS fabrication.

Let us now consider possible approaches for attaching a magnetic particle to a CNT NEMS. The main challenge lies in the precision that is needed for aiming material deposition at the nanotube without affecting other parts of the device (typical dimensions of the suspended nanotube segment in a CNT NEMS are diameters on the order of 1 nm and lengths on the order of 1 μm). One option would be a lithographic method similar to the ones demonstrated by B. Witkamp *et al.* [82] or A. Barreiro *et al.* [83]. For this, CNTs would be synthesised on a substrate surface and located in scanning electron microscopy (SEM). An individual nanotube is selected, electrodes are fabricated on top with electron beam lithography (EBL) and a small metal disc is deposited on the nanotube between the electrodes in a second EBL step. Finally, the CNT is suspended in a wet etching step. One can even melt the particle on the nanotube by driving a high current through the device (or possibly via annealing in an inert atmosphere), transforming it from a disc into a sphere [83]. The main disadvantage of this method is exposure of the nanotube to high-energy electron beams (SEM and EBL) and various chemicals used for lithography and etching. This can introduce structural defects and contamination on the nanotube, likely leading to inferior device quality.

An alternative method for deposition of a magnetic particle on a CNT is focused electron beam induced deposition (FEBID). This is a high precision process for deposition of small amounts of materials, performed in a modified SEM chamber. A precursor gas is injected into the chamber close to the target surface for material deposition. Electron beam irradiation causes localised dissociation of precursor molecules and material deposition from the dissociation products. G. Gruber *et al.* [84] have demonstrated deposition of Pt nanoparticles on the apex of singly clamped CNT cantilevers in FEBID. However, the doubly clamped geometry of a CNT

NEMS is presumably less suitable for this method, since typical nanotube diameters are still much smaller than the spatial resolution of FEBID material deposition, which would likely result in unwanted deposition in the nanotube vicinity (especially underneath the nanotube). Furthermore, similar to the issues with the lithographic approach, the high-energy electron beam required to trigger material deposition could cause structural defects in the nanotube and deposition of amorphous carbon, a side product of precursor dissociation, would contaminate the area. Finally, the magnetic particle on an MRFM sensor needs to produce a strong magnetic field gradient, so ideally should be as small as possible with a high saturation magnetisation. Unfortunately, even with a carefully optimised FEBID recipe the deposited material contains significant amounts of oxygen and carbon, reducing the achievable maximum magnetisation. For example, S. Sangiao *et al.* [85] report a maximum purity of 93 at% for their deposition of Co nanospheres, with a significant drop as the particle size falls below 300 nm.

Here, a new method is proposed, where the substrate on which the device is fabricated acts as a shadow mask for deposition of magnetic material onto the nanotube. A rendering of the proposed device geometry is shown in [Figure 4.6](#). A CNT is suspended over two finger gates between a pair of source-drain electrodes, forming a NEMS. The device sits between an additional pair of electrodes on top of a mesa, facilitating deterministic placement of the CNT in a stamp transfer process (see [Section 4.2.3](#)). A trench is etched all the way through the substrate between the gate electrodes, so that during material deposited onto the back of the substrate, for example via thermal evaporation, a thin beam of material is directed onto the centre of the suspended nanotube while the rest of the device is shielded against material deposition. Considering typical dimensions of CNT NEMS (source-drain gap on the order of 1 μm), the trench can only be a few hundred nanometres wide at most while the typical thickness of Si wafers, the most commonly used substrate for CNT NEMS fabrication, is on the order of a few hundred micrometres. A trench of that aspect ratio can not be fabricated and would be impossible to align with any source for material deposition (material from a misaligned source would coat the trench wall and plug up the trench before ever reaching the nanotube). To solve this, a “funnel” is etched into the back of the substrate, reducing the aspect ratio of the remaining trench to a value close to one. Such a funnel can easily be created by exploiting the anisotropic nature of certain Si wet etching processes, for example in KOH etchant. Using the device substrate as a shadow mask for magnet deposition onto the nanotube of course means that the back of the substrate also gets coated in a film of magnetic material, which can not be removed afterwards without destroying the device. Whether this has any significant impact (positive or negative) on device parameters or MRFM detector performance remains to be

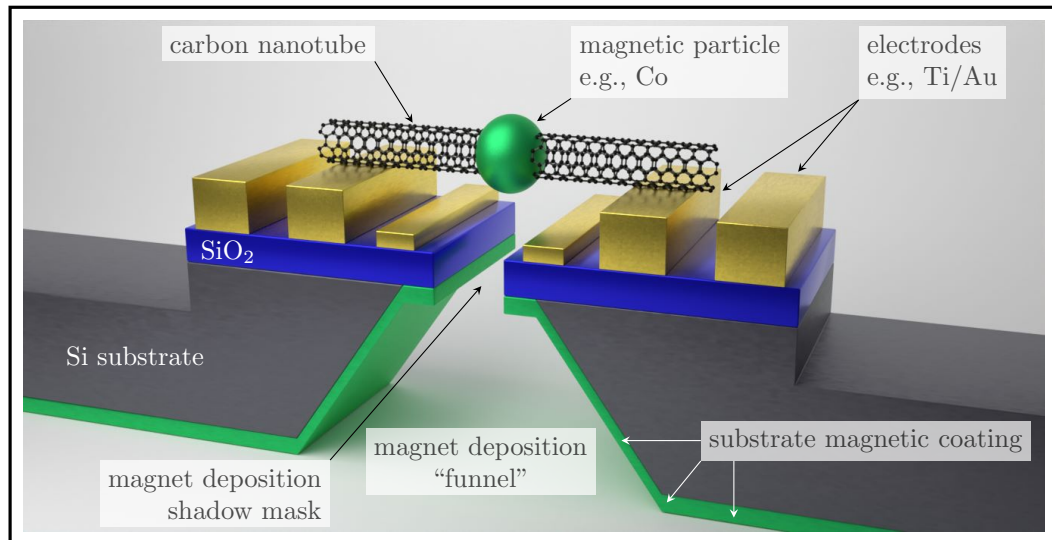


Figure 4.6: Rendering of a design proposal for a CNT NEMS based magnet-on-cantilever type MRFM sensor. See main text for details.

tested in experiments once a prototype has been fabricated.

4.2.2 Carbon nanotube synthesis

Carbon nanotubes can be created in a few different ways. A method that is mostly of historical relevance is arc discharge between graphite electrodes. A spark between the electrodes creates conditions that allows formation of CNTs. This is the method that was used when SWCNTs were first discovered in 1993 as a byproduct in the creation of fullerenes [31, 32]. Yield and purity of CNTs are generally poor with this method and the produced nanotubes tend to be multi-walled or form ropes [53]. Furthermore, the requirement of solid graphite for the starting material makes it expensive compared to more modern processes. Using laser ablation to evaporate a graphite target significantly increases the yield of SWCNTs, but many disadvantages of the arc discharge method remain [53].

Today the method of choice for CNT synthesis is typically some form of chemical vapour deposition (CVD) [53, 86–89]. The nanotubes used in this work are created in a catalytic CVD process at atmospheric pressure. Compared to other methods, catalytic ambient-pressure CVD is more economic and relatively easy to implement and maintain, which makes it one of the most common ways of synthesising CNTs in a research setting. See Figure 4.7 for a schematic and photograph of the setup used in this work.

In catalytic CVD the carbon source is a hydrocarbon gas. Most commonly used gases have low molecular weight (e.g., methane, ethane or ethylene [53, 88]), but larger molecules have also been shown to work [90]. At high enough temperatures

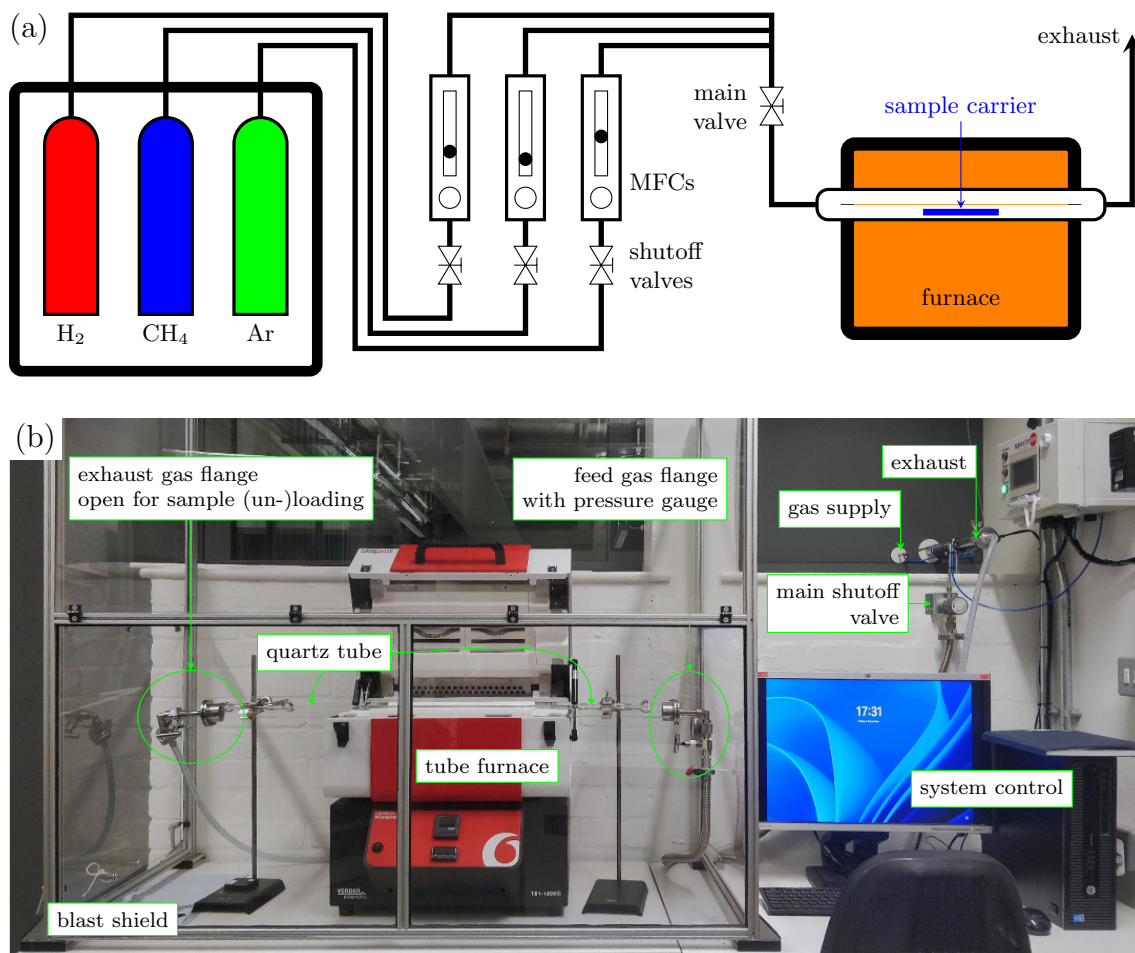


Figure 4.7: Tube furnace CVD setup for CNT synthesis. (a) Schematic of the system. Substrates are placed inside the quartz tube of a tube furnace to achieve the required process temperature. Composition and flow rate of process gas is controlled by a set of computer-controlled mass flow controllers. (b) Photograph of the system with important components marked. Mass flow controllers and gas storage are located behind the wall outside the building. This setup was planned in collaboration with S. Khan and E. A. Laird. S. Khan built the setup and established a process for on-chip growth of individual SWCNTs for CNT NEMSs. In this work the setup is used to grow CNTs for stamp transfer (see [Section 4.2.3](#)).

(typically 600–1000 °C) and in the presence of a transition metal catalyst (Fe, Co and Ni are most common) the gas thermally decomposes and the released carbon dissolves into the catalyst material [87, 88, 91]. If the catalyst is present in the form of nanoparticles, those particles will then act as seeds for CNT growth [77, 87].

When tuning process parameters for CNT synthesis, the following rules of thumb can be applied [87, 88, 92]:

- CNT diameter scales with catalyst particle size
- small catalyst particles ($d \sim 1$ nm) grow SWCNTs, medium size particles (10 nm $\lesssim d \lesssim$ 50 nm) grow MWCNTs and larger particles get encapsulated in graphite without growing any nanotubes
- higher temperatures reduce the density of CNT growth, i.e., fewer CNTs per unit area
- lower temperatures produce more MWCNTs while higher temperatures favour SWCNTs
- higher temperatures produce longer CNTs
- higher temperatures produce CNTs with fewer structural defects

4.2.3 Carbon nanotube stamp transfer

In fabrication processes for devices made of ultraclean individual SWCNTs, synthesis of the nanotube is usually the last step. Otherwise, exposure of the nanotube to other fabrication steps can lead to structural defects (e.g., from exposure to a high-energy electron beam in electron beam lithography) and contamination (e.g., residues from resists used for lithography or other chemicals), degrading device quality.

Since CNT synthesis requires the presence of a catalyst, dedicated areas for growing nanotubes on a device chip can be defined by applying the catalyst with a lithography and lift-off technique. This allows growing CNTs directly over pre-fabricated contact electrodes as a last fabrication step. However, since direction and density of CNT growth can not be precisely controlled, on-chip growth of nanotubes is a statistical process, often resulting in a low device yield. Therefore, this approach is only valid if devices can be made quickly in large numbers and with a reasonably high device count per unit area. Furthermore, we saw in the previous section that CNT synthesis requires relatively harsh conditions, severely limiting material choices for devices that need to survive this process. The temperatures required to grow clean SWCNTs are high enough to melt common electrode materials like gold with

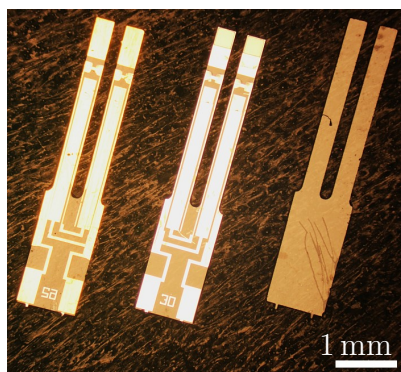


Figure 4.8: Commercially available quartz tuning forks. Left: Tuning forks are shipped with gold electrodes. Middle: Stripping the gold layer reveals another layer of silvery metal, presumably an adhesion layer of titanium. Right: Stripping the second metal layer leaves a blank quartz fork that can be used for CNT growth and transfer.

a titanium adhesion layer. Moreover, elemental carbon from the CVD atmosphere can diffuse into metallic structures on the chip, which is particularly problematic if the device has superconducting components, because the carbon contamination can suppress superconductivity in thin films [93].

To avoid problems of on-chip CNT growth, several groups have developed different approaches to nanotube transfer techniques [94–99]. Here, CNT synthesis is performed on dedicated growth substrates and nanotubes are subsequently transferred onto pre-fabricated device chips. This allows placing individual CNTs on devices as a last fabrication step without exposing the device chip to CVD conditions. Additionally, large numbers of devices are no longer required to achieve reasonable yields. Transfer of a single CNT is still a statistical process, but many attempts can be made on the same set of contact electrodes until a device is assembled successfully. In case an unsuitable nanotube is transferred, it can simply be removed by burning it off in oxygen plasma or with a pulse of high current, after which the device can be reused for more transfer attempts.

Carbon nanotube growth on carrier substrates for stamp transfer

Following the methods developed as part of my master’s thesis [97], we initially use commercially available quartz tuning forks with a gap between prongs of about $150\ \mu\text{m}$ (see Figure 4.8) as substrates for CNT growth. This allows us to begin establishing CNT stamping as part of our device fabrication without the need for also developing a fabrication process for the CVD substrate. The quartz forks are prepared for use in our process by removing the metallic electrodes with an aqueous KI/I_2 solution and hot hydrochloric acid, followed by cleaning steps of sonication in Acetone and isopropyl alcohol (IPA) and plasma ashing.

Later on, to reduce dependence on external suppliers, and to gain the ability of adjusting the CVD substrate geometry to best fit the target device chip in the future, a process for fabricating SiO_2 coated silicon combs was developed (see Figure 4.9(a) for the process flow). These comb substrates consist of a small square main body and

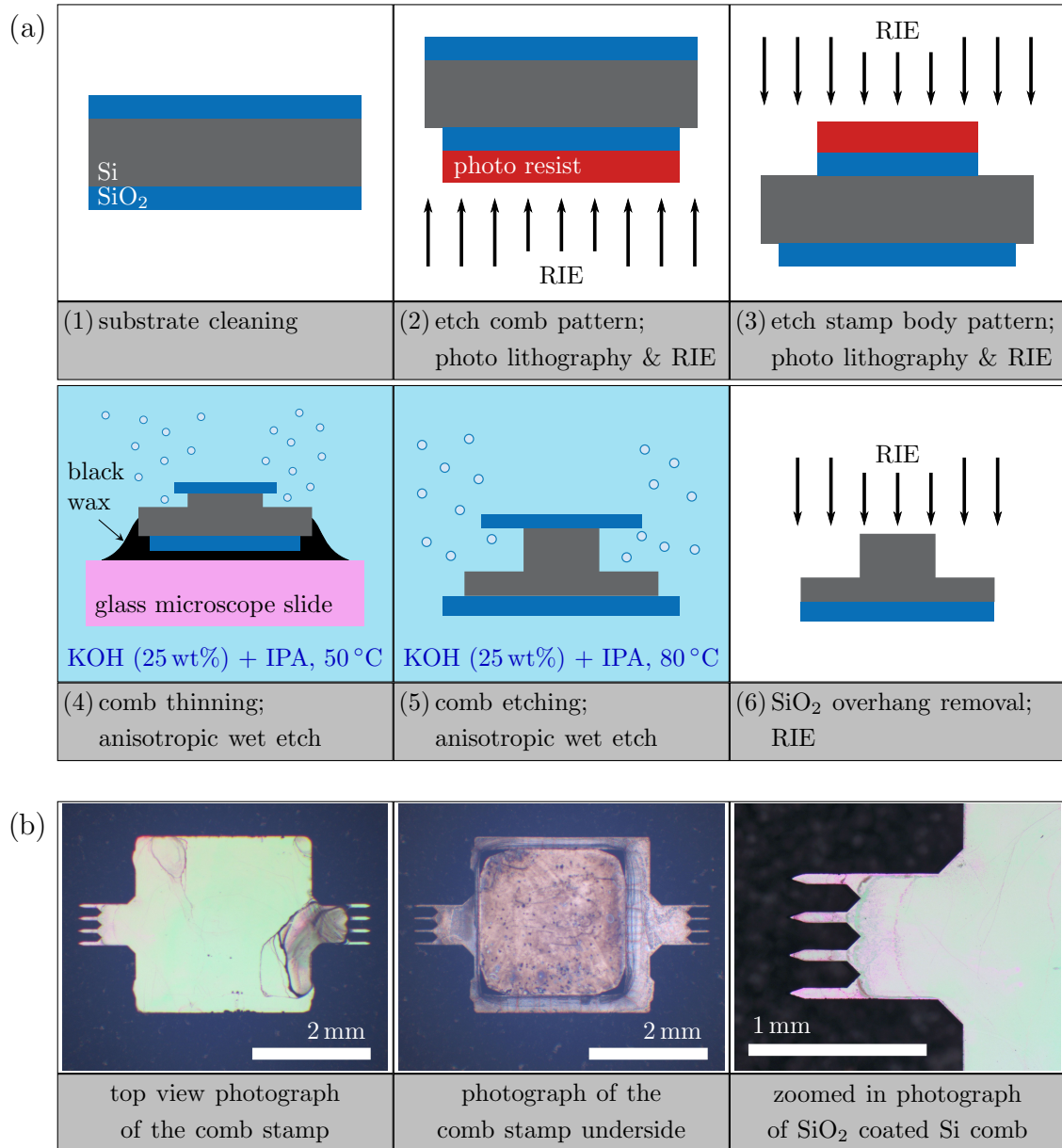


Figure 4.9: (a) Process flow for in-house fabrication of SiO₂ coated Si combs for CNT growth and transfer. See main text for more detail. (b) Photographs of Si/SiO₂ combs fabricated according to the process in (a). Photographs were taken after combs were already used for CNT growth and transfer. Stains visible on the surface are deposits from the Fe(NO₃)₃/MoO₂(acac)₂/alumina suspension catalyst.

combs with reduced substrate thickness protruding on two sides (see photographs in Figure 4.9(b)). Fabrication begins with a piece from a double-side polished (100) oriented Si wafer of 300 μm thickness with 1000 nm of SiO_2 (wet thermal oxide) on both sides. The patterns for the combs and main body are defined on either side of the substrate with photo lithography and transferred into the SiO_2 layers via reactive ion etching (RIE), making sure that the edges of the pattern are aligned with the (100) crystal plane of the Si substrate. A glass microscope slide is then glued to the comb side of the substrate with black wax⁸, exposing only the back of the substrate to the subsequent anisotropic wet etching step in KOH etchant (25 wt% aqueous solution mixed with IPA at a volume ratio of 3:1). IPA is added to the etchant as a surfactant to improve consistency and surface finish of the etch [100–102]. Once the comb area is thinned down to double the intended final thickness, the substrate is released from the microscope slide by dissolving the wax adhesive in Xylene. The wet etching is continued, now etching the comb pattern into the front of the substrate while simultaneously further reducing the substrate thickness in the comb area. Note that the sidewalls of this etch are made of the same Si crystal plane as the substrate surface, meaning that undercut and etching in the intended direction happen at the same rate. Therefore, the comb thickness can never exceed twice the distance between the comb tines, making the first wet etching step for substrate thinning necessary in order to achieve a tine spacing similar to the gap between the prongs of the quartz tuning forks. Etching is stopped with a rinse in deionised (DI) water as soon as the etches from both sides meet. Due to the substantial undercut during wet etching a brim of SiO_2 is left along the perimeter of the finished comb chip, which is removed with RIE using the bulk Si of the comb and chip body as etch mask. After final cleaning steps of sonication in Acetone and IPA and plasma ashing the comb chip is ready for use.

Two different types of catalyst have been used for growing CNTs on both the quartz forks and comb chips. The first is a suspension in ethanol or deionised water, containing transition metal compounds ($\text{Fe}(\text{NO}_3)_3$ and $\text{MoO}_2(\text{acac})_2$) and alumina nanoparticles. The catalyst storage flask needs to be placed in an ultrasonic bath for at least 20 min before every use to avoid clumping of solid components in the suspension. The catalyst is applied to the SiO_2 surface of comb substrates via dropcasting, while the prongs of quartz forks are simply dipped into the catalyst suspension. Subsequent baking on a hotplate drives off residual solvent. The second type of catalyst used is metallic cobalt. A layer of nominally 1 nm thickness is applied to substrates via thermal evaporation. When deposited at such low nominal thickness Co does not form a homogeneous film, but random nanometre sized clusters which

⁸Apiezon[®] Wax W, applied as solution in Xylene

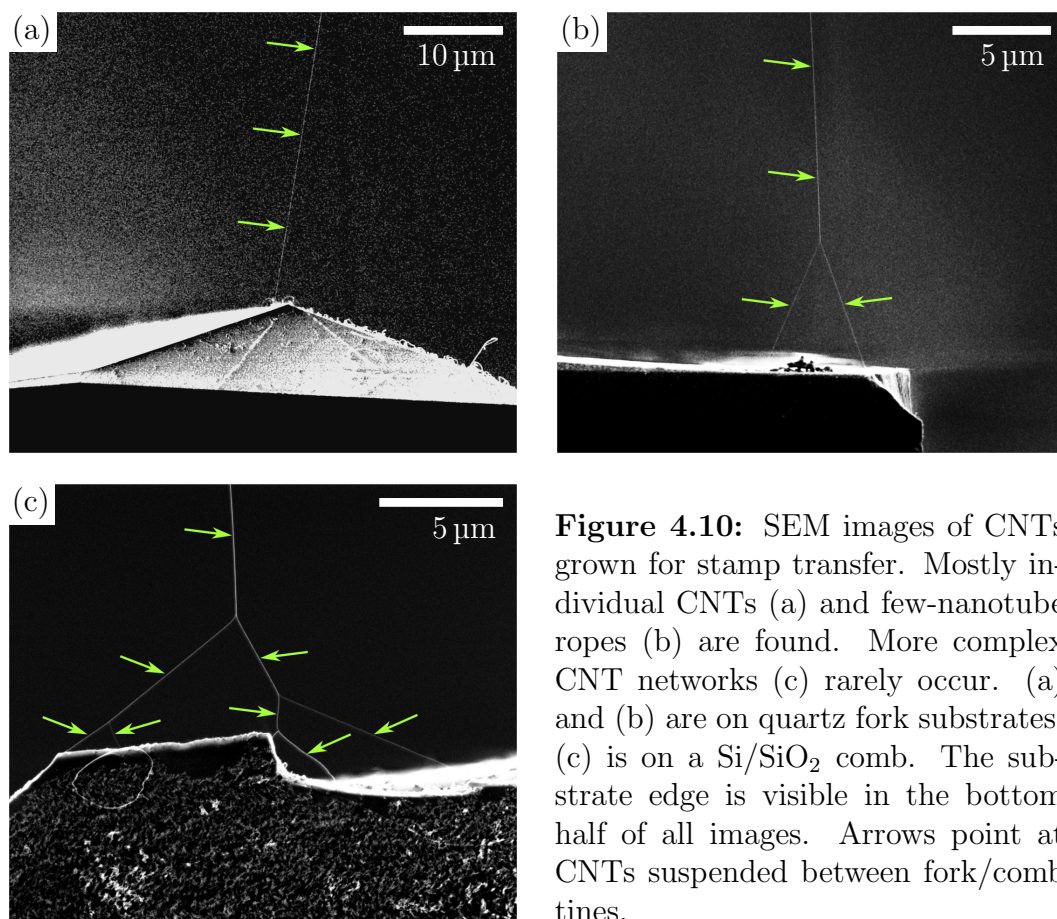


Figure 4.10: SEM images of CNTs grown for stamp transfer. Mostly individual CNTs (a) and few-nanotube ropes (b) are found. More complex CNT networks (c) rarely occur. (a) and (b) are on quartz fork substrates, (c) is on a Si/SiO₂ comb. The substrate edge is visible in the bottom half of all images. Arrows point at CNTs suspended between fork/comb tines.

then act as catalyst centres for CNT growth.

After catalyst application, substrates are placed inside the quartz tube of the CVD furnace shown in Figure 4.7(b) with tines oriented perpendicular to the gas flow direction. They are heated to 960 °C in a flow of Ar and H₂. When the target temperature is reached, the Ar is shut off and gas flow is adjusted to 20 sccm H₂ plus 10 sccm CH₄. During this phase CNTs grow from tine to tine, which is aided by nanotube growth being guided in the direction of gas flow [94, 103]. The growth phase is stopped after 30 min by switching the gas flow back to the same combination of Ar and H₂ that was used during the warm up phase. The substrates are left to cool down below ~ 100 °C in Ar+H₂ atmosphere before they are removed from the CVD furnace. Note that the additional hydrogen component in the process gas reduces metal oxides in the catalyst back to pure metals [88], increases efficiency of catalytic decomposition of the carbon feed gas [53] and suppresses the deposition of unwanted amorphous carbon [86, 87].

Inspection of substrates in SEM showed that this recipe produces CNTs suspended over the approximately 150 μm gap between tines for all combinations of the two catalysts and two substrate types. Most inspected gaps had about one to five CNT bridges across, the majority of which were either individual nanotubes or few-

nanotube ropes, with only rare occurrences of more complex nanotube networks, see [Figure 4.10](#) for examples. So far, the sample size has been too small for a proper statistical analysis of differences between the used catalysts and substrates. Note that generally only a small sample size from each CVD batch is inspected in SEM to confirm successful nanotube growth. Growth substrates used for nanotube transfer are not imaged in SEM to avoid contamination with amorphous carbon.

Both the quartz forks and the Si combs are chemically inert and relatively mechanically robust, making them reusable. If the previous cycle was done with Co catalyst, carbon residues are removed via plasma ashing followed by removal of the old catalyst with hot dilute nitric acid. After additional cleaning with sonication in Acetone and IPA and another plasma ashing step the substrate can re-enter the fabrication cycle at the catalyst deposition step. No equivalent cleaning process for substrate reuse after a run with the catalyst suspension has been found, yet. However, a first test of re-growing CNTs from old suspension type catalyst after only a cleaning step in oxygen plasma looked promising.

Description of the transfer process

The process for carbon nanotube transfer applied here follows the method developed as part of my master's thesis [97], which was in turn inspired by methods published by J. Waissman *et al.* [98] and J. Gramich *et al.* [95]. Photographs of the setup, a modified semi-automatic probe station⁹, are shown in [Figure 4.11](#). A prefabricated device chip (the *target*) is glued and wire bonded into one of the QDevil sample carrier PCBs that we use in our dilution refrigerator (cf. [Figure 2.3\(b\)](#)). The layout of the target chip needs to consist of four equally high electrodes – source (S) and drain (D) of the finished device plus two additional contacts (S2 and D2) used in the nanotube transfer process – with at least one lower gate electrode between source and drain¹⁰ and deep etched areas on both sides of the electrodes. The sample carrier is mounted onto a PCB based interface with spring loaded contact pins on the transfer setup sample stage ([Figure 4.11\(b\)](#)), which allows us to make electrical contact to the device chip electrodes and perform in-situ measurements during the CNT transfer process. A quartz fork or Si comb chip (the *stamp*) which has gone through the preparations and CVD process described in the previous section, and therefore

⁹This probe station was modified twice over the course of the work presented here. It started out as an EverBeing C-4 manual probe station, which was first equipped with motorised stages from Standa Ltd and programmed to function as a semi-automatic probe station for more efficient room temperature pre-characterisation and device selection of CNT devices fabricated with on-chip nanotube growth. Later, the setup was modified again to also accommodate the CNT stamp transfer process.

¹⁰Global gating through the device chip substrate should in principle also be possible, but makes no sense for the device design used in this work, so we will ignore it here.

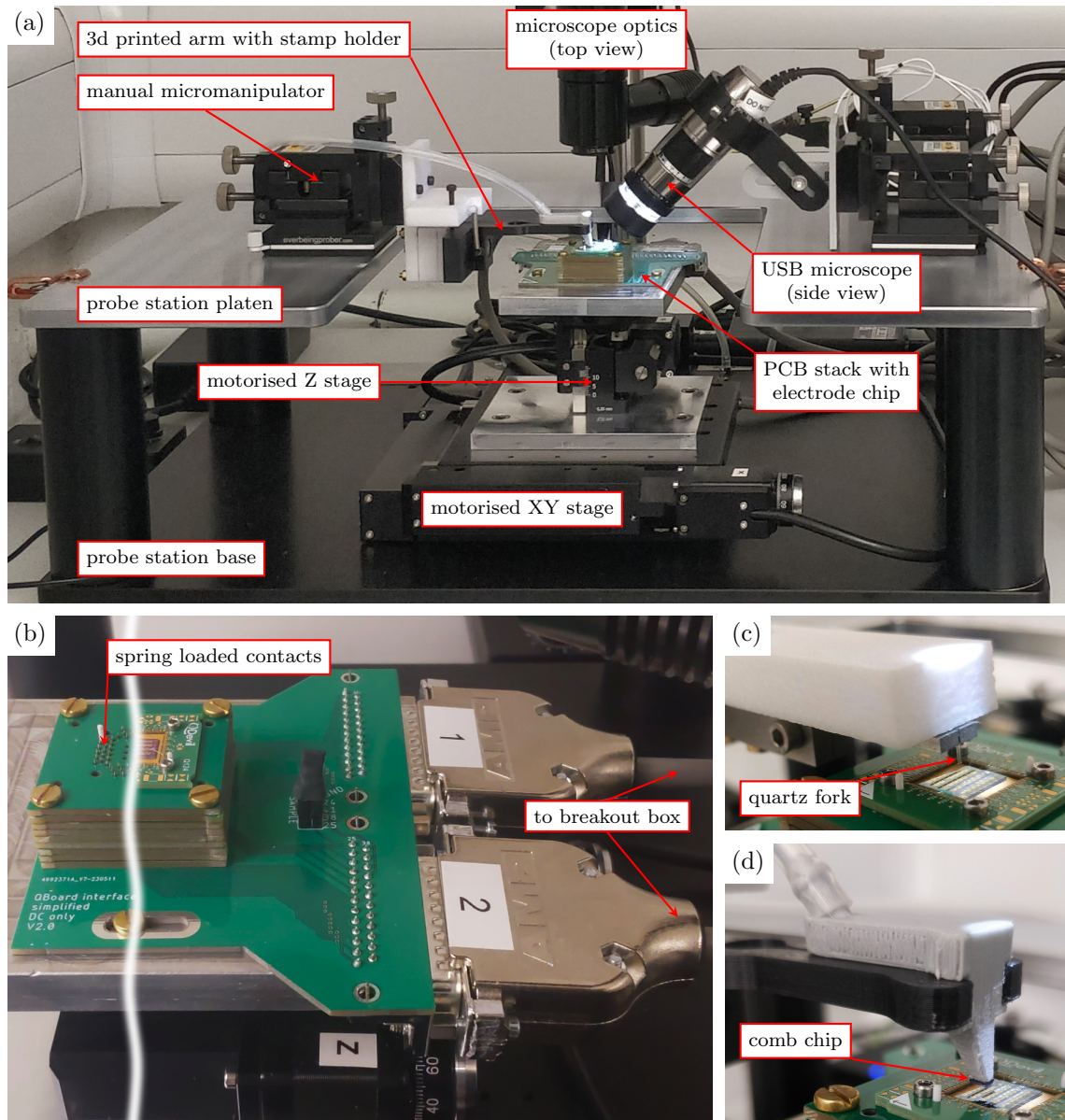


Figure 4.11: Setup for CNT stamp transfer. (a) The setup is based on a semi-automatic probe station. A prefabricated device chip is glued and wire bonded into a sample carrier PCB and loaded onto the probe station sample stage. A CNT growth substrate is attached to a 3d printed arm on a manual micromanipulator and can be aligned with and lowered onto the device chip. The process is monitored via optical microscopes and cameras (top and side view). (b) The sample carrier PCB is mounted on a PCB interface on the sample stage, which makes electrical contact to the sample carrier (and device chip) through spring loaded pins. This allows for in-situ measurements during the transfer process. (c) Quartz forks are clamped in a steel clamp on the micromanipulator arm in a nearly vertical orientation. (d) Comb chips are held nearly parallel to the device chip with a 3d printed vacuum nozzle.

should be carrying CNTs, is attached to a micromanipulator (see [Figure 4.11\(c\),\(d\)](#) for mounting interfaces). Stamp and target are aligned optically using a top view and tilted side view from camera-equipped microscopes. The sample stage is then slowly raised towards the stamp to begin the nanotube transfer process.

The steps of the transfer process are illustrated in [Figure 4.12](#) with example data from in-situ measurements shown in [Figure 4.13](#). Initially, while the target chip approaches the stamp and the stamp prongs sink into the deep etched areas on either side of the device electrodes, a voltage of typically 75 mV is applied between the outer electrodes S2 and D2 and the current is measured ([Figure 4.12\(a\)](#)). As soon as the device makes contact with a CNT on the stamp a finite current starts to flow ([Figure 4.13\(a\) and \(e\)](#)) and the movement of the target towards the stamp is stopped. By sweeping the gate voltage ([Figure 4.12\(b\)](#) and [Figure 4.13\(b\)](#)) one can attempt to identify the type of CNT that has been contacted (cf. [Figure 4.5](#)). If a nanotube with unwanted properties is detected, it can simply be rejected by moving the target chip away from the stamp. The CNT stays attached to the stamp and is lifted off the device electrodes. Unfortunately, most of our devices initially exhibit very high contact resistance and reliable identification of the nanotube type seems not possible.

To finish the transfer process, the contacted nanotube needs to be detached from the stamp. This is done by ramping up the voltage and thus current between electrodes S and S2, and subsequently between D and D2, until the nanotube segments between those electrode pairs break ([Figure 4.12\(c\)](#)). Typical currents for “cutting” a CNT are in the range 4–30 μA , roughly consistent with references [95, 97, 98]. Cutting of the nanotube can be seen as sharp drops in current flow ([Figure 4.13\(c\) and \(f\)](#)). When an individual SWCNT has been contacted, the current drops to zero in a single step. If the current breaks down in multiple steps this can be attributed to breaking individual shells of a MWCNT or individual nanotubes in a CNT rope [97]. In rare cases tails of finite current after cutting of the nanotube or no breakdown steps in the current are observed (e.g., left panel in [Figure 4.13\(f\)](#)). This can be explained by the nanotube getting ripped off the stamp (e.g., when the approach of stamp and target is not done carefully enough, or when the stamp-target alignment is slightly off). If the nanotube falls onto the exposed silicon in the deep etched area next to the electrodes, current can keep flowing through the device chip substrate.

Once the nanotube has been cut on both sides of the device, the centre segment remains on the chip, connecting the source and drain electrodes, while the rest of the CNT stays attached to the stamp and is lifted off the chip when stamp and target are separated.

The high currents flowing during the cutting step of the transfer process also

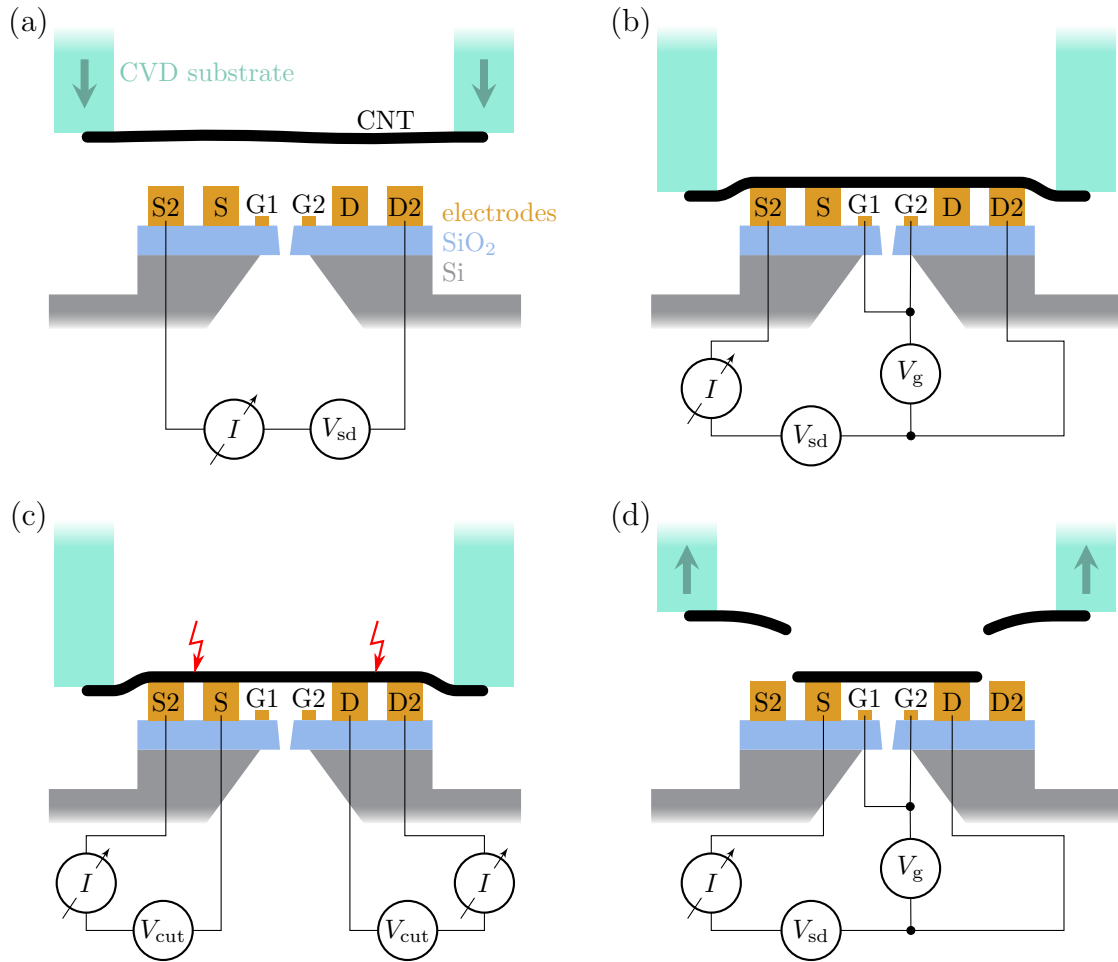


Figure 4.12: Schematics for the CNT transfer process. (a) While the CVD substrate with nanotubes is lowered onto the chip, a finite voltage is applied between the outermost contact electrodes and the current is monitored. (b) The prongs of the CVD substrate sink into the deep etched areas on the device chip and a CNT makes contact with the electrodes. In situ measurements can be performed to confirm whether the contacted nanotube is suitable for experiments. (c) When a suitable nanotube is identified, the CNT is cut between electrode pairs S-S2 and D-D2 by applying high currents, detaching the middle segment of the CNT from the CVD substrate. (d) At the end of a successful transfer process the CVD substrate is lifted away from the device chip. The cut off middle segment of the CNT stays on the device while the rest of the nanotube remains attached to the prongs of the CVD substrate. More measurements can be performed for final pre-characterisation. The device is ready for transfer into a cryostat for experiments.

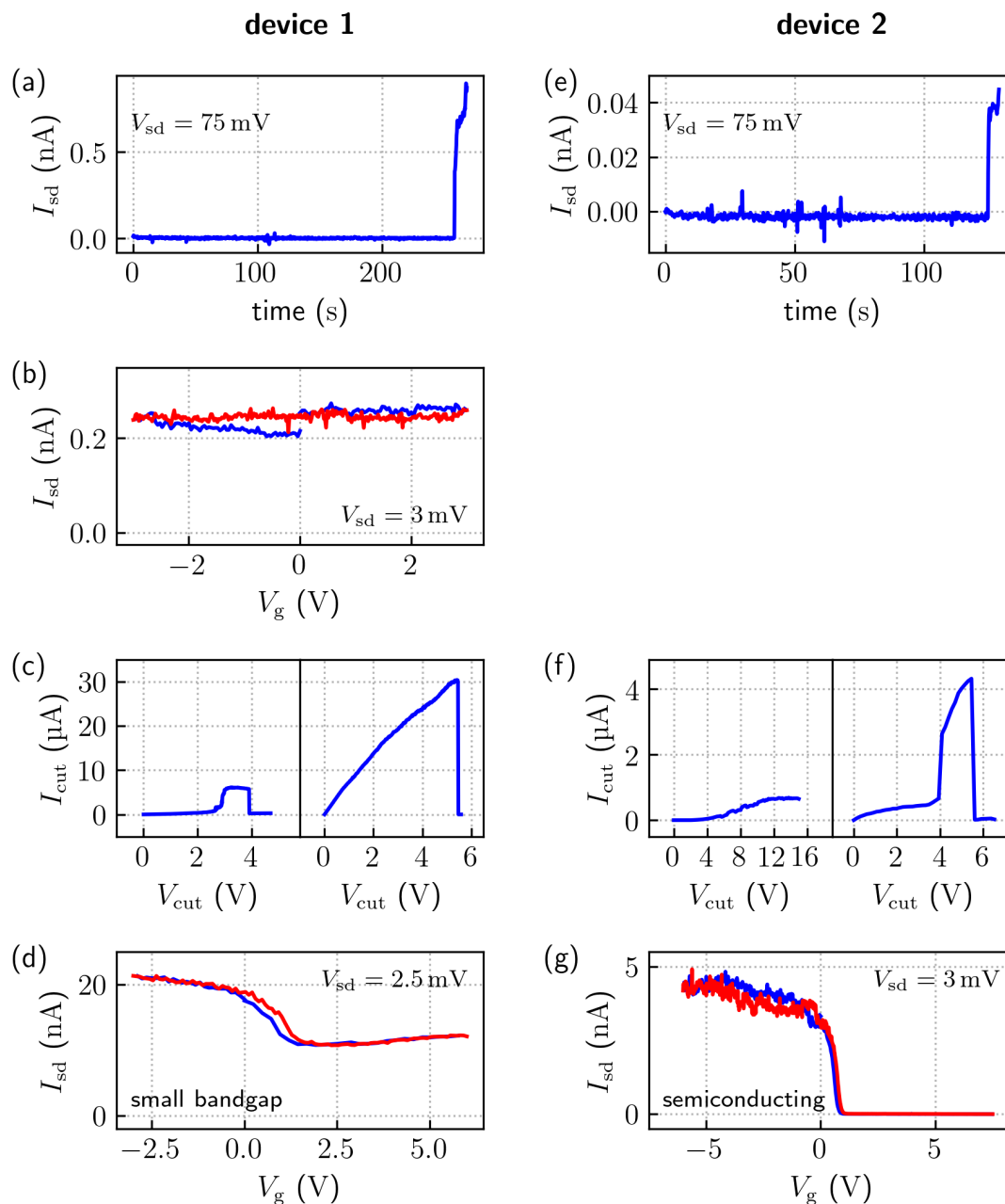


Figure 4.13: Example data from in situ measurements during CNT transfer for two devices. (a), (e) During the approach step the current jumps to a finite value as soon as a CNT is contacted. (b) In most cases reliable identification of CNT type from I - V_g -traces immediately after making contact is not possible due to very high contact resistance. No post-contact gate sweep was recorded for device 2. (c), (f) To break the CNT between the outer pairs of electrodes and fix the middle segment to the device, a voltage V_{cut} is ramped between the outer pairs of electrodes. Breaking of CNT segments is observed as sudden drops in current. The shape of the current drop allows conclusions to be drawn about the transferred nanotube, see main text. The high currents in this step have an annealing effect and reduce contact resistance of the remaining CNT segment. (d), (g) With the reduced contact resistance after cutting, another gate voltage sweep reveals the CNT type (compare to Figure 4.5). Device 1 is from a test chip used for establishing the nanotube transfer process. Device 2 is used throughout the rest of this thesis.

have an annealing effect, significantly lowering the contact resistance of devices. At the end of the transfer process another sweep of gate voltage is performed for final device type identification (Figure 4.12(d) and Figure 4.13(d) and (g)). If the device exhibits satisfactory properties in this final gate sweep it can immediately be transferred into a cryostat for experiments.

Note that device 2 in Figure 4.13 will be used for all low-temperature CNT NEMS experiments presented in this thesis. The gate voltage sweep in Figure 4.13(g) identifies it as large bandgap CNT with a relatively high resistance of about 600 k Ω in hole conduction at room temperature. Separate voltage sweeps on the two gate electrodes showed that only one of them is working. Generally this would not be considered a “good” device for low-temperature experiments, since such large bandgaps and high room temperature resistances often indicate a high risk of charge carrier freeze out at cryogenic temperatures, in which case the device is useless for low-temperature experiments. However, when a cryostat became available for cooling down devices from the first generation run of the fabrication process described in the next section, this was the best device available.

4.2.4 Device chip fabrication

We shall now go over the fabrication process that was developed for producing the device geometry proposed in Section 4.2.1. This work was carried out in the cleanroom facilities of the Lancaster Quantum Technology Centre. Throughout this section we will refer to Figure 4.14, which shows an overview of the fabrication process flow.

The process starts with a 50 mm diameter, double side polished, n-doped silicon wafer from Si-Mat Silicon Materials with a thickness of $300 \pm 25 \mu\text{m}$ and $\langle 100 \rangle$ crystal orientation. Both sides of the wafer are coated with 1000 nm SiO₂ (wet thermal oxide). The substrate is cleaned with concentrated nitric acid, sonication in Acetone and IPA and plasma ashing.

Steps (2) and (3) of the process (cf. Figure 4.14) prepare the substrate for etching the “magnet deposition funnel” into the back. The back side of the wafer is coated with a film of about 300 nm silicon nitride (SiN_x¹¹) in plasma-enhanced chemical vapour deposition (PECVD), using SiH₄ and N₂ as precursors. A layer of positive photo resist (Microposit S1813 G2) is spin coated on top of the SiN_x film and patterned with standard photo lithography. The pattern consists of rectangles

¹¹Stoichiometric silicon nitride has the chemical formula Si₃N₄. However, it was never checked if the silicon nitride films deposited in our process are stoichiometric and it seems unlikely that they would be just by coincidence. Therefore, we use the notation SiN_x to indicate the unknown ratio of Si and N atoms in the deposited film.

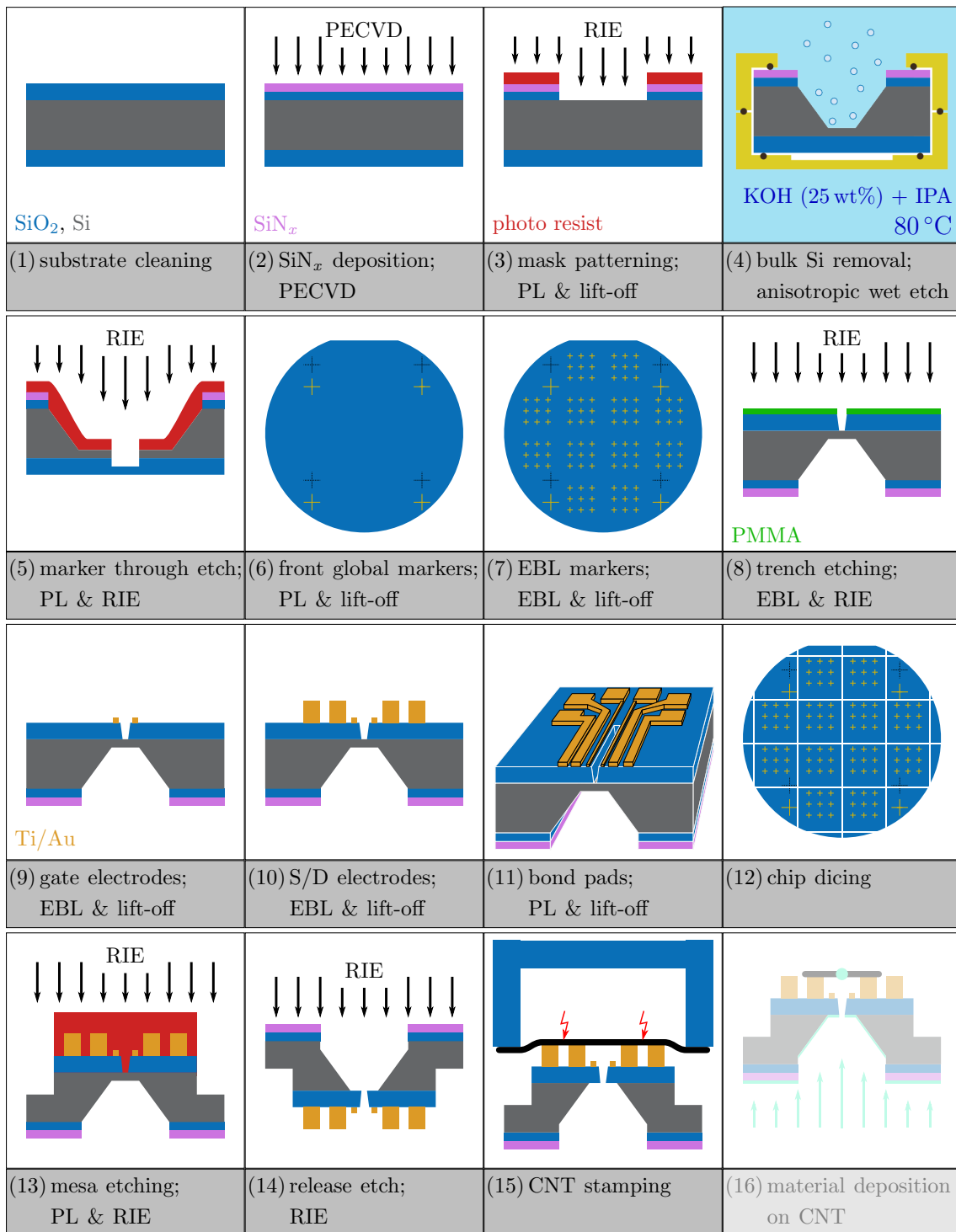


Figure 4.14: Process flow for the fabrication of a CNT NEMS with shadow mask built into the substrate for material deposition on the CNT centre. The last step (material deposition on the nanotube) has not yet been attempted. PL: photo lithography, EBL: electron beam lithography, PECVD: plasma enhanced chemical vapour deposition, RIE: reactive ion etching, S/D: source/drain.

aligned with the $\langle 110 \rangle$ crystal plane of the substrate and is transferred into the SiN_x and SiO_2 films with RIE. SiN_x is etched with a $\text{SF}_6 + \text{O}_2$ plasma, while $\text{CHF}_3 + \text{Ar}$ is used for the SiO_2 layer. After the etching, resist residue is stripped with solvents and plasma ashing.

The now patterned $\text{SiO}_2/\text{SiN}_x$ film acts as etch mask for the wet etching step in KOH solution that comes next. It should be mentioned that initially metallic hardmasks of Cr or Cr/Au were considered for this process, as this is sometimes suggested in literature (e.g., [104, 105]) and seemed convenient to work with. However, it turned out that the selectivity (i.e., the ratio of etch rates for the mask and substrate materials) of Si over Cr is not high enough for the etch depth we are aiming for here, so the required film thickness of pure Cr masks makes them impractical. Gold is chemically inert and does not get attacked by KOH. However, during testing Cr/Au masks were suffering from adhesion problems. Etchant would creep between mask and substrate, resulting in large craters underneath the mask as well as chunks of the mask flaking off the substrate. After consulting the extensive etch rate tables for different processes and materials in [106] it was eventually decided to switch to $\text{SiO}_2/\text{SiN}_x$ for the mask material.

Step (4) of the fabrication process is etching the “deposition funnel” into the back of the substrate in a wet etching process at 80°C , using a 25 wt% aqueous solution of KOH mixed with IPA at a volume ratio of 3:1 as etchant. IPA is added as a surfactant, making the etching process more reliable and improving surface finish. During this step the wafer is held in a specialised PEEK (polyetheretherketone) holder¹², protecting the wafer front and edge and only exposing the wafer back to the etchant. The anisotropic nature of this etching process creates slanted sidewalls at an angle of 54.74° , thus creating (truncated) inverted pyramids from the rectangular openings in the etch mask, giving us the funnel shapes we are aiming for. Etching takes about 4.5 hours at an etch rate of approximately $1.04\ \mu\text{m}/\text{min}$ and is stopped with a rinse in DI water. Etch time and dimensions of the etch mask are chosen so that the bottom of the etch forms a rectangle of approximately $15 \times 210\ \mu\text{m}^2$, about $10\text{--}15\ \mu\text{m}$ short of the opposite side of the wafer, to maintain some mechanical robustness and reduce the risk of damage from handling the wafer throughout the rest of the process.

Next we need a way of aligning the devices we will fabricate on the front of the wafer with the funnels we just etched into the back. Unfortunately, our equipment has no capabilities for aligning features on opposite sides of a wafer. We solve this in *step (5)* by etching markers through the substrate, using the patterns shown in [Figure 4.15\(a\)](#). Although not mentioned yet, the first layer of this marker pattern with a

¹²” wafer holder from the Single series of wafer holders for single-side etching by AMMT GmbH

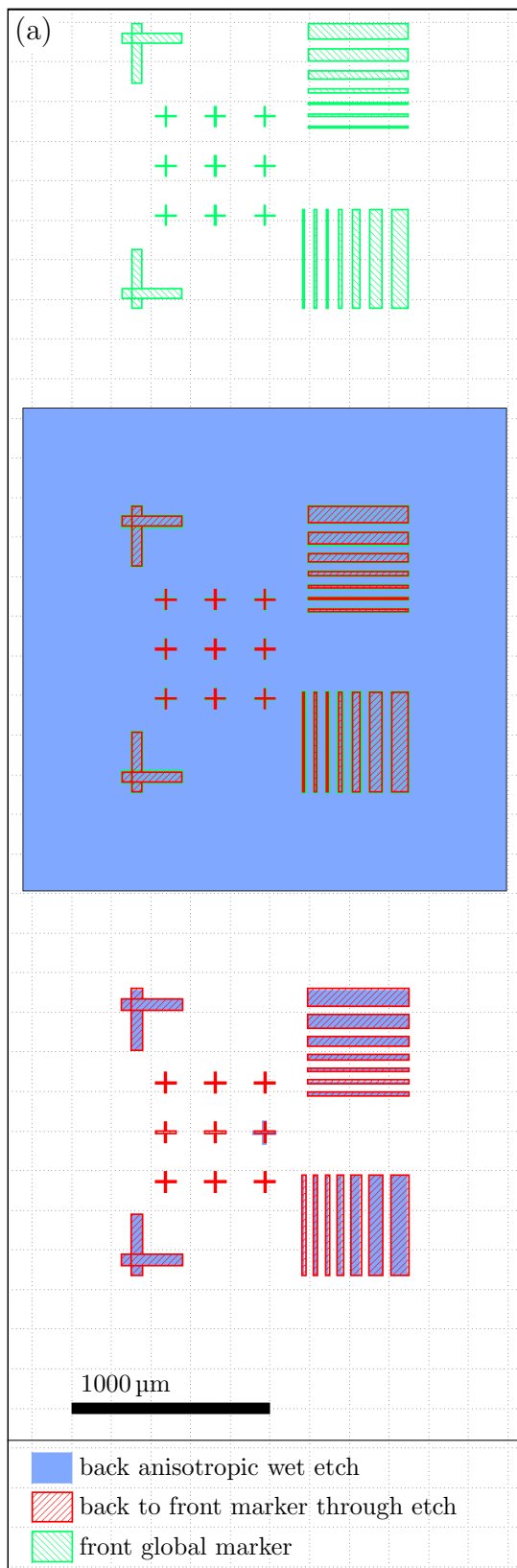


Figure 4.15: (a) Three layer lithography mask pattern for alignment of features on two sides of a Si/SiO₂ wafer via marker through etching. (b) Photograph of a through etched marker pattern (the middle section of (a)) viewed from the front side of the wafer in optical dark field microscopy. Dark areas are the top SiO₂ layer backed by a thin remaining layer of Si. The orange pattern are markers etched into the thinned down Si from the back and only consist of the top side SiO₂ film. Bright yellow lines mark the edges of a patterned photoresist layer for transferring the marker pattern to the front side of the wafer in a metal deposition and lift-off process.

large square window next to it, was also included in wet etching in *step (4)* (once on every quadrant of the wafer). We now use a photo lithography process to offset the marker patterns into the windows next to them. Using RIE with a $\text{CHF}_3 + \text{SF}_6 + \text{O}_2$ plasma we then etch the markers into the thin remaining Si layer of the windows until the material becomes thin enough to be transparent, thus making the markers visible from the front side of the wafer (see photograph in [Figure 4.15\(b\)](#)). The marker windows are now quite fragile and the wafer must be handled with utmost care during the subsequent cleaning steps to avoid damage. Resist residue after the marker through etch is removed with solvents and plasma ashing. Typically, at this point in the process both sides of the wafer have accumulated some contaminations. In order to avoid bad adhesion of deposited metal structures in upcoming steps the substrate cleaning process with nitric acid, Acetone, IPA and plasma ashing from the beginning is repeated, but this time without ultrasound treatment, as this would break the fragile marker windows.

To preserve back to front alignment in case of damage to the marker windows, we offset the markers again on the front of the wafer. For extra mechanical robustness the substrate is glued onto a spare wafer with a few drops of photoresist during this step. We then create a copy of the markers made from 10 nm Ti and 40 nm Au next to the marker window using standard photo lithography, metal deposition via thermal evaporation and lift-off (process *step 6*). The lift-off step also releases the substrate from the support wafer, which is no longer needed as the fragile marker windows are now redundant.

In order to be able to achieve the necessary alignment precision between upcoming layers of EBL, a marker pattern is laid down on the front side of the wafer, indicating the position of each individual device (*step (7)*). This is done with standard EBL, deposition of 10 nm Ti and 40 nm Au via thermal evaporation and lift-off.

Step (8) is etching the narrow trench through the front SiO_2 film, that will later be the opening in the shadow mask for material deposition onto a suspended nanotube (cf. [Figure 4.6](#)). For this, the substrate is spin coated with three layers of EBL resist (aiming for a resist layer of approximately 1000 nm PMMA 950k). Stacking resist layers does reduce feature resolution, but selectivity over EBL resist of the SiO_2 etching process is quite low and thus the extra layers are needed to achieve sufficient mask thickness. After EBL exposure, the SiO_2 trenches are etched in RIE using CHF_3 and Ar. Even with the reduced resolution from resist layer stacking, we can produce a trench as narrow as 160 nm. Resist residue is stripped with oxygen plasma.

Steps (9) and (10) define the electrode pattern of the device. First, two gate fingers (one on either side of the SiO_2 trench) are created with EBL, metal deposition

via thermal evaporation and lift-off. The same steps are then repeated to pattern the source and drain electrodes as well as the pair of additional electrodes needed for CNT cutting during the stamp transfer process (cf. [Section 4.2.3](#)). Gates are made of 10 nm Ti and 40 nm Au, 150 nm wide and spaced 500 nm apart to accommodate the SiO₂ trench. Source, drain and cutting electrodes are higher (10 nm Ti plus 190 nm Au) to keep nanotubes suspended between source and drain. The source-drain gap, and thus the designed length of suspended CNT segments, is 1.1 μm. All electrodes are about 200 μm long, chosen to be slightly longer than the thickness of the quartz forks used for nanotube transfer, in order to maximise the chances for contacting a CNT during stamping, independent of where it is located on the fork.

Step (11) adds bond pads (also made of Ti/Au) to the devices with a standard photolithography, metal deposition (thermal evaporation) and lift-off process.

The wafer is scanned for electrical shorts using the nanotube stamping setup (cf. [Figure 4.11](#)) in its original semi-automatic probestation configuration, typically revealing a device yield on the order of 90 %. Subsequently, the wafer is diced into smaller chips that fit the sample carrier PCBs in our cryostat (*step (12)*). To protect the devices from dust during the dicing process, the wafer is spin coated with a layer of photoresist. After dicing, the resist (and dust on top) is washed off with Acetone, followed by cleaning with IPA and plasma ashing.

Step (13) creates the mesa that is needed for nanotube stamp transfer. Large rectangular windows are patterned on both sides of the device electrodes with standard photolithography, using an extra thick photoresist (Merck AZ 40XT-11D). These windows are then RIE etched through the SiO₂ coating (using SF₆ and Ar) and about 25 μm deep into the Si substrate (using CHF₃, SF₆ and O₂).

Finally, *step (14)* concludes the cleanroom processing part of device fabrication. Here, the thin Si layer that was left at the bottom of the back side funnel after *step (4)* is removed in another RIE process (CHF₃+SF₆+O₂), opening up the shadow mask for material deposition onto a nanotube all the way through the entire substrate thickness. This step needs to be monitored carefully to make sure that enough Si is removed, while enough of the SiO₂ film remains to maintain sufficient mechanical device stability. Due to small local variations of etch rates, contamination and substrate thickness, typically only a handful of devices per chip will turn out to be usable, making it absolutely crucial that the yield up to this point is as high as possible. Due to its very uneven surface, the substrate front side should be protected during this last etch to avoid unwanted etching there. This can be done with a coating of photoresist, which is carefully stripped with solvents afterwards. Persistent contaminations from resist can be cleaned with oxygen plasma.

After glueing and wire bonding the device chip into a sample carrier PCB, the

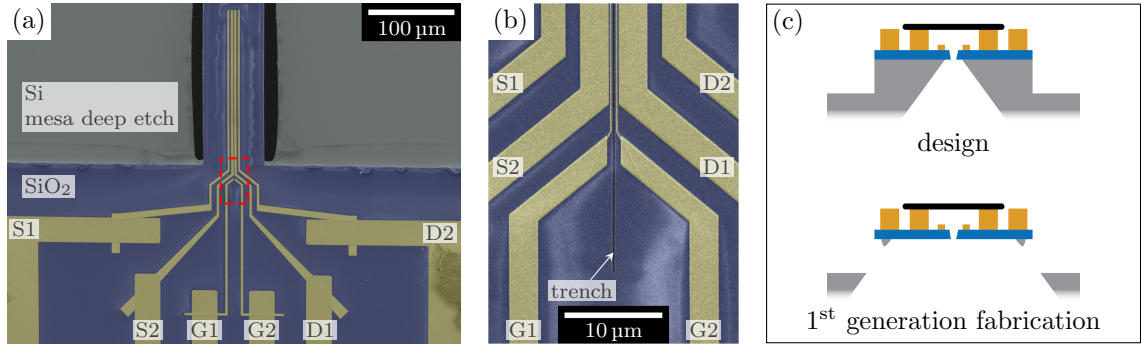


Figure 4.16: (a) SEM image of a device ready for CNT transfer. (b) Magnified view of the area inside the dashed red rectangle in (a). (c) Sketch of device cross section, comparing the desired structure with the cross section achieved from the first generation of device fabrication. The hollowed out mesa that carries the device electrodes in the design turned into a nearly unsupported bridge of SiO₂ membrane. In (a) the gaps left by missing mesa sidewalls can be seen as black areas on either side of the device.

final step (*step (15)*) in the fabrication process is placing a CNT on the device, using the stamp transfer procedure described in [Section 4.2.3](#).

[Figure 4.16\(a\)](#) and [\(b\)](#) shows SEM images of a finished device immediately *before* CNT transfer. Since nanotube devices are generally not exposed to SEM before conclusion of experiments to avoid contamination, unfortunately, at the time of writing this thesis no images of a completed device (including a nanotube across the electrodes) exist. We can see that features on the front side of the substrate turned out nicely, but the device cross section deviates considerably from the design (see sketch in [Figure 4.16\(c\)](#), more on this in the next section). Nevertheless, all features required for the device to function are present, albeit more fragile, so a device from this first generation fabrication run is used for the experiments in later sections.

After successful completion of the first 15 steps of the fabrication process, the resulting device was cooled down in our cryostat for characterisation, so that later on a direct comparison of the same device before and after deposition of a magnetic particle will be possible. Since at this point initial device characterisation was prioritised over completing a full run of the fabrication process, the final *step (16)*, deposition of a magnet onto a suspended CNT through the substrate shadow mask, has not yet been attempted at the time of writing this thesis.

4.2.5 Opportunities for process improvements

Experience with the fabrication process presented in the previous section has revealed several areas of possible improvement.

First, we shall address the difference in device cross section between design and

outcome shown in [Figure 4.16](#). This was the result of several misjudgements at the design stage due to lack of experience with some fabrication steps. Since the achievable precision of feature alignment on opposite wafer sides was unknown, a generous margin for misalignment of $7\ \mu\text{m}$ in all directions was implemented in the design. It seems that this margin can easily be reduced to less than $2\ \mu\text{m}$, reducing the initial width of the back side funnel etched in process *steps (3) and (4)*. Additionally, the horizontal etch rate in *steps (13) and (14)* was underestimated. Undercut in *step (13)* could possibly be reduced by optimising the RIE recipe. Lateral etching in *step (14)* needs to be respected in the design by further reducing the initial width of the back side funnel.

Lateral etching in *step (14)* also plays into another possible opportunity for improvement. If this step widens the funnel anyway, it might be possible to reduce the initial funnel width to a point where wet etching in *step (4)* stops on an intersection of Si $\langle 111 \rangle$ crystal planes just short of the opposite wafer side. In this case etching of the through etch marker windows could continue all the way through the entire thickness of the substrate, while the funnel etch would automatically stop before breaking through to the other side. If the size of the marker windows is then reduced appropriately, the windows themselves could become the markers, making *step (5)* of the process obsolete.

The remaining two improvement suggestions are related to CNT stamp transfer in *step (15)*. First, CVD substrates are currently selected as stamps at random, relying purely on luck for contacting favourable nanotubes. Screening growth substrates with Raman spectroscopy, a non-contact and non-invasive method that uses inelastic scattering of light and – if done right – has hardly any effect on nanotube properties, should allow detection and even type identification (metallic, semiconducting, multi-walled) of CNTs [107]. This would allow more targeted stamp selection, improving efficiency of the transfer process by avoiding attempts with empty stamps, and possibly enabling fabrication of devices with specific nanotube types. Second, the high initial contact resistance we generally observe during nanotube transfer is problematic, as it requires completion of the transfer for reliable device type identification. S. Jung *et al.* [108] have shown for their approach to nanotube stamping that contact resistance can be significantly reduced with an additional cleaning step in Ar plasma for the target chip immediately prior to nanotube stamping. Such an extra cleaning step seems easy to implement and should definitely be tested in the next fabrication run.

4.3 Low temperature electronic transport and Coulomb blockade

4.3.1 Carbon nanotube quantum dots

Carbon nanotubes are intrinsically one dimensional objects (cf. [Section 4.1.2](#)). In electronic transport measurements, segments typically on the order of $1\ \mu\text{m}$ are coupled to metallic lead electrodes, leading to further reduction of the dimensionality and formation of a quantum dot (QD) on the CNT segment between the leads. [Figure 4.17](#) shows an equivalent circuit diagram of a QD. A conductive island (the nanotube segment) couples to source and drain electrodes through emerging tunnel barriers. Barriers are represented by a parallel circuit of the tunnel junction capacitance $C_{s/d}$ and tunnel resistors $R_{s/d}$. The magnitude of current flow through the dot depends on the tunnel rates $\Gamma_{s/d}^{+/-}$ between the dot and the source/drain reservoirs. Capacitive coupling to a gate electrode, parametrised by the gate capacitance C_g , allows manipulation of the QD electrochemical potential. Parasitic contributions to the dot capacitance from coupling to the environment are summarised in C_{env} .

When both the tunnel rates to the leads $\Gamma_{s/d}^{+/-}$ and the thermal energy $k_B T$ are smaller than the electrostatic charging energy

$$E_C = \frac{e^2}{C_{\text{dot}}} \quad (4.13)$$

with the total capacitance of the QD

$$C_{\text{dot}} = C_s + C_d + C_g + C_{\text{env}} \quad (4.14)$$

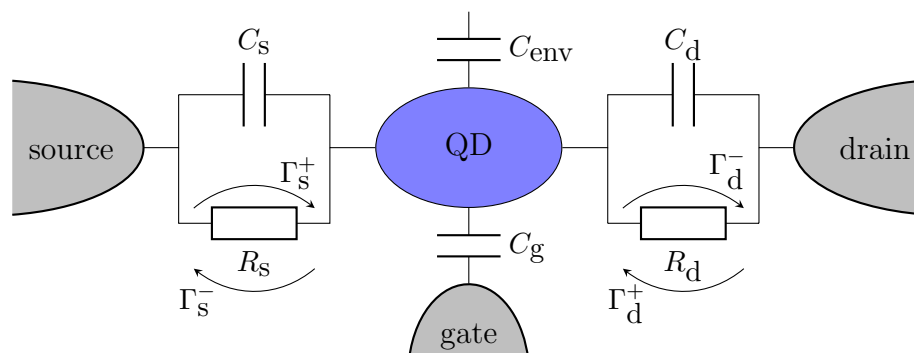


Figure 4.17: Schematic of a quantum dot. A conductive island is coupled to source and drain electrodes through tunnel junctions with tunnel rates $\Gamma_s^{+/-}$ and $\Gamma_d^{+/-}$. The junctions are drawn as equivalent circuits consisting of capacitances $C_{s/d}$ and tunnel resistances $R_{s/d}$. A gate electrode is capacitively coupled to the island through C_g . Parasitic capacitances to the environment are condensed into C_{env} .

the charge on the dot becomes constrained to integer multiples of the elementary charge, with interesting consequences for the transport characteristics.

Following [109], we outline the description of low-temperature electron transport through a quantum dot in the *constant interaction model*. The model makes two simplifying assumptions. First, all Coulomb interactions between electrons on the dot, as well as between the dot and environment, are parametrised by the single constant capacitance C_{dot} given in Equation (4.14). Second, single-particle energy levels are independent of such Coulomb interactions and thus independent of the dot's charge occupation. Under these assumptions the total energy of a QD occupied by N electrons in the ground state is given by (neglecting parasitic capacitances)

$$U(N) = \frac{[-e(N - N_0) + C_s V_s + C_d V_d + C_g V_g]^2}{2C_{\text{dot}}} + \sum_{n=1}^N E_n. \quad (4.15)$$

Here, e is the elementary charge, V_s , V_d and V_g are voltages applied to the source, drain and gate, respectively, N_0 is the charge occupancy with no voltages applied (set by fixed charges in the environment and not necessarily quantised) and E_n are the single-particle energy levels from spatial confinement on the QD.

In general, estimating the contributions E_n from single particle spectra is difficult, since they depend on a number of factors, such as the CNT bandgap and diameter, sharpness of the confinement potential and interactions [55]. However, this is not important for the work in this thesis, so we will simply acknowledge that single particle energy spectra contribute to QD transport characteristics without going into further detail.

We define the electrochemical potential of the QD with occupation N as the energy difference between ground states with N and $N - 1$ electrons:

$$\mu(N) = U(N) - U(N - 1) \quad (4.16)$$

$$= E_C \left(N - N_0 - \frac{1}{2} \right) - \frac{E_C}{e} (C_s V_s + C_d V_d + C_g V_g) + E_N. \quad (4.17)$$

Similarly, the energy for adding an electron to the leads at the Fermi level defines the electrochemical potentials of the leads

$$\mu_s = E_F - eV_{\text{sd}}, \quad (4.18)$$

$$\mu_d = E_F, \quad (4.19)$$

where E_F is the Fermi level and V_{sd} is voltage difference between the source and drain electrode.

From Equation (4.17) we can see that the QD electrochemical potential forms a

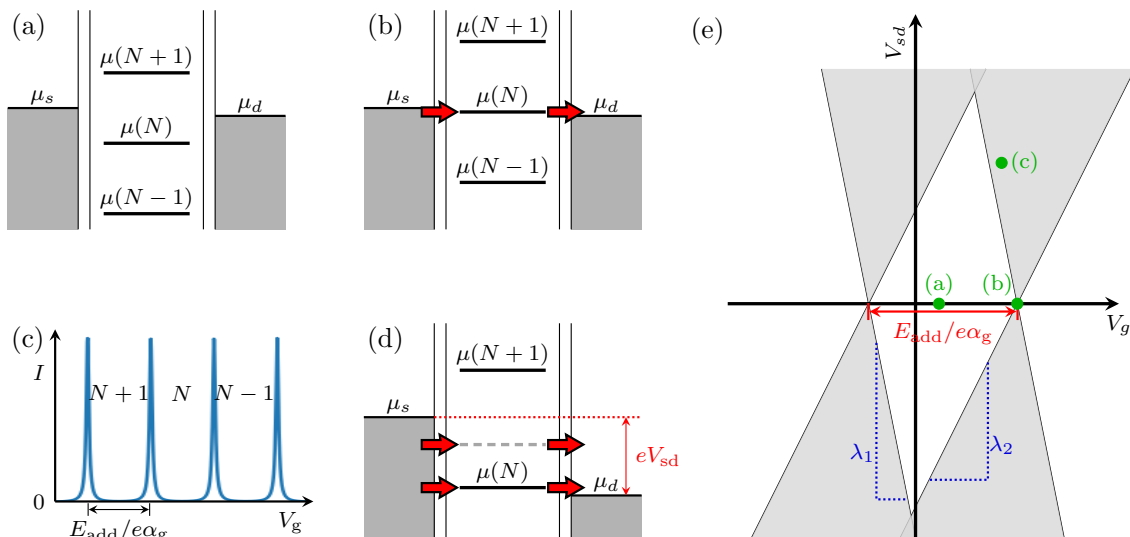


Figure 4.18: Ladder of electrochemical potentials in a quantum dot and consequences for electron transport. (a) When the levels of the quantum dot are not aligned with the chemical potential of the leads, no current can flow and the dot is in Coulomb blockade. (b) In contrast, when a dot level is tuned to align with the source-drain bias window with a gate voltage V_g , current flows via sequential tunnelling of electrons. (c) The current as function of gate voltage $I(V_g)$ shows a series of peaks, as the dot switches between Coulomb blockade and sequential electron tunnelling. (d) Tunnelling is possible as long as a quantum dot level is within the source-drain bias window. In the high-bias regime, excited states of the single-particle spectrum (dashed grey level) can contribute to transport. (e) Recording the current while sweeping both the source and gate voltage leads to a diamond shaped pattern known as Coulomb diamonds, which is characteristic for transport through a quantum dot. Dimensions of the diamonds depend on parameters of the quantum dot. (Adapted from [109])

ladder of discrete levels that can be shifted up and down continuously by applying a gate voltage. The distance between levels is the addition energy

$$E_{\text{add}} = \mu(N) - \mu(N-1) \quad (4.20)$$

$$= E_C + \Delta E(N) \quad (4.21)$$

which includes both an electrostatic term E_C and the quantum energy level spacing of the single-particle spectrum $\Delta E(N) = E_N - E_{N-1}$. Note that, since CNTs inherit the fourfold degeneracy of electronic states from graphene (twofold each for spin and valley degrees of freedom, cf. Section 4.1.2), contributions $\Delta E(N)$ will only be non-zero when N is a multiple of four, leading to fourfold periodicity in the spacing of electrochemical potential $\mu(N)$.

Current flow through the QD is only possible if all steps of the process are

energetically favourable, i.e. when the condition

$$\mu_s > \mu(N) > \mu_d \quad (4.22)$$

is fulfilled. This means that when no level of the dot electrochemical potential is aligned with the bias window between the source and drain potentials, as is the case in [Figure 4.18\(a\)](#), current flow is suppressed and the device is in *Coulomb blockade*. If the dot potential is shifted with an appropriate gate voltage, so that one of the levels lands within the source-drain bias window, current starts to flow via sequential tunnelling of electrons through the QD ([Figure 4.18\(b\)](#)). When the current through the dot is measured as a function of gate voltage, a series of peaks is observed as sketched in [Figure 4.18\(c\)](#). The distance between peaks is given by

$$\Delta V_g = \frac{E_{\text{add}}}{e\alpha_g}, \quad (4.23)$$

where $\alpha_g = C_g/C_{\text{dot}}$ is the lever arm characterising the coupling strength between the dot and gate. In the high-bias regime excited states of the single-particle spectrum, or in more extreme cases even neighbouring levels of the electrochemical potential, can also contribute to electron transport ([Figure 4.18\(d\)](#)).

The width of the current peaks in [Figure 4.18\(c\)](#) depends on the width of the source-drain bias window (i.e., on the applied source drain voltage V_{sd}). When current through the QD is recorded as function of bias voltage V_{sd} and gate voltage V_g , a plot of the corresponding *stability diagram* shows a characteristic pattern known as *Coulomb diamonds* ([Figure 4.18\(e\)](#)). Knowing that the edges of Coulomb diamonds correspond to tuning of the dot electrochemical potential so that either $\mu(N) = \mu_s$ or $\mu(N) = \mu_d$, we can use [Equations \(4.17\)-\(4.19\)](#) with $V_d = 0$ and $V_s = V_{\text{sd}}$ to calculate the slopes of the diamonds as

$$\lambda_1 = -\frac{C_g}{C_s} < 0 \quad (4.24)$$

$$\lambda_2 = \frac{C_g}{C_{\text{dot}} - C_s} > 0 \quad (4.25)$$

Similarly, the height of a Coulomb diamond ΔV_{sd} is related to the addition energy as

$$e\Delta V_{\text{sd}} = E_{\text{add}}. \quad (4.26)$$

4.3.2 Transport spectroscopy of a carbon nanotube quantum dot

In this section, results from transport spectroscopy on a CNT quantum dot are presented. The device was fabricated following the process described in [Section 4.2](#) and cooled to about 10 mK on the mixing chamber stage of our dilution refrigerator.

Schematics of the measurement setup are shown in [Figure 4.19](#). Lowpass filters of the cryostat wiring and sample carrier PCB (cf. [Sections 2.2](#) and [2.3](#)) are not shown in the figure. A source voltage is applied from an isolated low-noise voltage source module in a battery powered IVVI-DAC2 modular rack unit (“IVVI”) made by QuTech. The voltage source is regulated via the output of a PC-controlled digital-to-analogue converter (DAC) in the same IVVI rack. The output of a second DAC channel is routed through a 5x amplifier module of the IVVI and used as gate voltage. Gate voltages are applied to only one of the two gates, since the second gate was already found to be broken in room temperature measurements taken as part of the nanotube transfer process during device fabrication (cf. [Section 4.2.3](#)). Current through the nanotube is measured with a transimpedance amplifier (yet another module of the IVVI, used with a conversion factor of 10^9V/A most of the time) and Keithley 2100 digital multimeter.

Measuring the current at a small bias voltage while sweeping gate voltage ([Figure 4.20\(a\)](#)), we find that current flow is suppressed for all values of V_g in the range $-3.5 \text{ V} \leq V_g \leq 10 \text{ V}$. The wide range of suppressed current conforms with the large bandgap of the device that was already observed at room temperature (cf. [Figure 4.13](#)). For $V_g \lesssim -3.5 \text{ V}$, the characteristic peaks from alternating Coulomb blockade and sequential electron tunnelling appear. The height of current peaks is

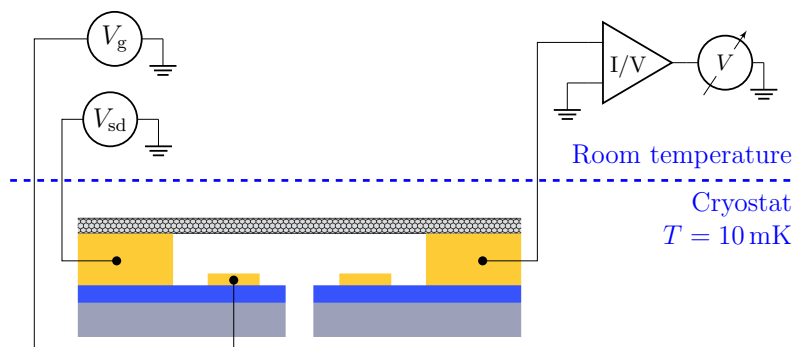


Figure 4.19: Schematics of the measurement setup for transport spectroscopy on a CNT quantum dot. The device is mounted inside the sample puck on the mixing chamber stage of our dilution refrigerator with a base temperature of about 10 mK. Bias and gate voltages V_{sd} and V_g are applied from battery powered low noise voltage sources at room temperature. The current through the device is measured with a transimpedance amplifier and digital multimeter.

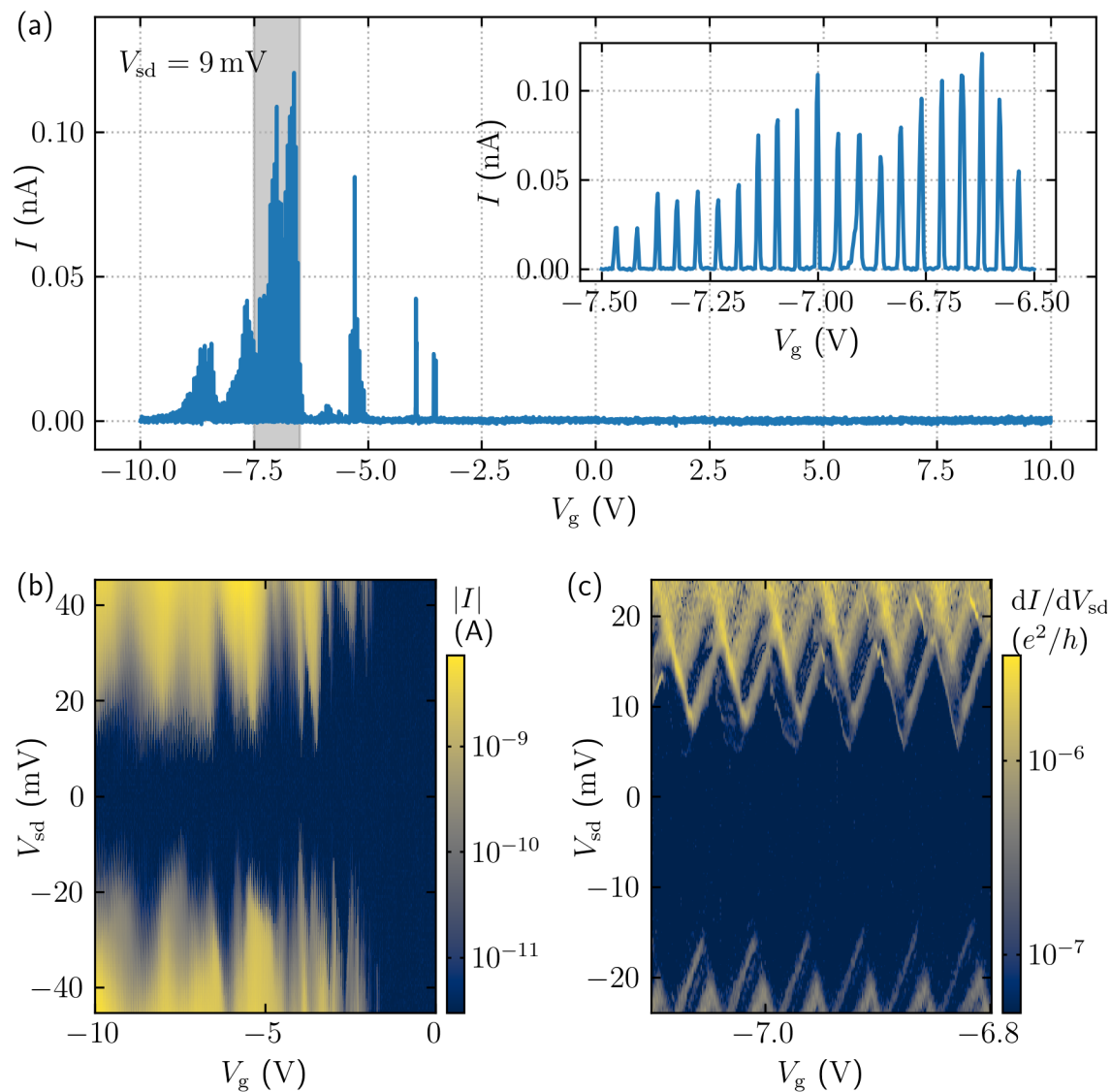


Figure 4.20: Transport spectroscopy of a large bandgap CNT quantum dot. (a) When sweeping gate voltage at a fixed bias voltage $V_{sd} = 9$ mV the device does not conduct for positive gate voltages up to 10 V. For negative gate voltages $V_g < -3$ V current oscillations typical for Coulomb blockade are observed. Inset: detailed view of the grey shaded area in the main panel. (b) Overview of current $|I(V_{sd}, V_g)|$ as function of gate voltage V_g and bias voltage V_{sd} , showing large irregular Coulomb diamonds overlaid on top of smaller more regular diamonds. (c) Detailed view of numerically obtained differential conductance in the parameter range used in later experiments. Coulomb diamonds from this device do not close at zero bias voltage.

quite irregular. A fourfold pattern in the peak spacing is not visible, suggesting that device characteristics are dominated by the electrostatic charging energy and contributions from the single-particle energy spectrum are negligible.

A stability diagram on the hole conduction side (Figure 4.20(b)) shows a pattern of regular Coulomb diamonds, overlaid with a second set of much larger and much more irregular diamonds. The diamonds do not close at zero bias. Both the overlay of multiple diamond patterns and the conductance gap near zero bias can be explained by a chain of multiple quantum dots. For example, disorder near the CNT interface to the leads could result in the formation of one or more small quantum dots in series with the main dot on the suspended segment of the nanotube.

Figure 4.20(c) shows a detail plot of Coulomb diamonds in the parameter region used in Chapter 5. Applying Equations (4.21) and (4.23)-(4.26) to this data (with $\Delta E(N) = 0$, since we do not see a fourfold pattern in the Coulomb blockade oscillations), we obtain a charging energy $E_C = 11.2 \pm 0.8$ meV, capacitances $C_s = 6.6 \pm 0.5$ aF, $C_g = 3.38 \pm 0.06$ aF and $C_{\text{dot}} = 14.4 \pm 1.1$ aF and lever arms $\alpha_s = 0.46 \pm 0.03$ and $\alpha_g = 0.24 \pm 0.02$, see also Table 4.2.

4.4 Carbon nanotube nanomechanical resonators

Carbon nanotubes can exhibit several modes of mechanical vibration. In order of decreasing energy scales, these are radial breathing modes (i.e., expansion and contraction of the nanotube in the radial direction), longitudinal stretching modes in the direction of the nanotube axis and guitar string like transversal bending modes [110]. Here we will focus exclusively on bending modes.

Unlike many other nanomechanical devices – for example Si or Al beams, Al drums or SiN membranes – which are fabricated in top-down processes, CNT devices can be assembled in a bottom-up process like the one presented in Section 4.2. With this, fabrication related structural defects and impurities can be avoided for CNT devices, resulting in reduced damping [45, 111]. Exceptional mechanical quality factors up to 5 million for suspended CNT resonators have been experimentally demonstrated [13].

The high stiffness and low mass of CNTs results in mechanical frequencies on the order of megahertz to even gigahertz [44, 45, 111] and large zero-point motion amplitudes up to 10 pm [111]. At millikelvin temperatures it is possible to achieve $\hbar\omega_{\text{mech}} \gg k_B T$, so that nearly no thermal excitation of vibrations can exist. This makes CNTs candidates for observing quantum effects in mechanical resonators.

The rest of this section, after a brief introduction to the theoretical description of CNT transverse vibrations, discusses a method for actuating and detecting the

motion of a CNT resonator, as well as some interactions with electron tunnelling through a quantum dot on the nanotube.

4.4.1 Transverse vibrations of a suspended carbon nanotube

Despite their very small diameter (only a few carbon atoms along the circumference), carbon nanotubes are well described by continuum mechanics [112]. See Figure 4.21(a) for relevant device dimensions and orientation of the coordinate system. The equation of motion for a thin beam is the Euler-Bernoulli equation

$$\rho A \frac{\partial^2 u}{\partial t^2} + \eta \frac{\partial u}{\partial t} + EI \frac{\partial^4 u}{\partial x^4} - T \frac{\partial^2 u}{\partial x^2} = F_{\text{ext}} \quad (4.27)$$

which describes displacement $u(x, t)$ as a function of time t and position along the beam axis x . The first term describes acceleration and depends on the mass density ρ and cross sectional area A of the beam. The second term is a damping term and will be neglected here. The restoring force due to bending rigidity of the beam represented by the third term depends on the product of the Young's modulus E and second moment of inertia I . An additional component of the restoring force comes from the tension T (fourth term). F_{ext} is an external force acting on the beam.

The geometry of our CNT device is that of a doubly-clamped beam. Therefore, we are looking for solutions of Equation (4.27) that fulfil the boundary conditions

$$u(0, t) = u(L, t) = 0 \quad (4.28)$$

$$\frac{\partial u}{\partial x}(0, t) = \frac{\partial u}{\partial x}(L, t) = 0. \quad (4.29)$$

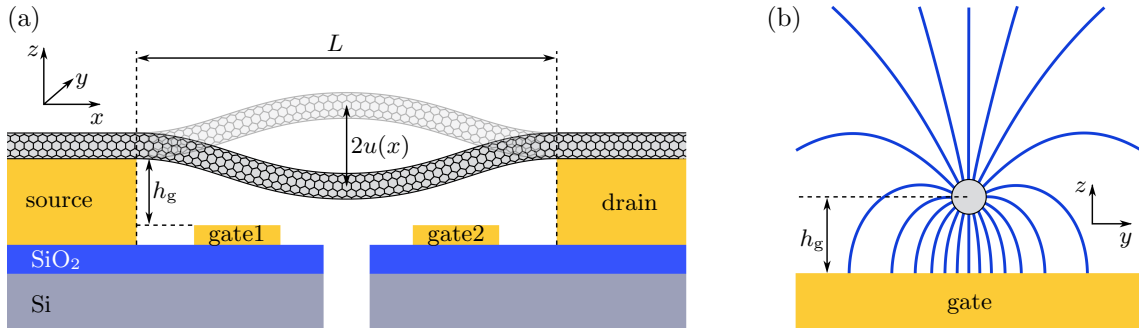


Figure 4.21: (a) Side view of a carbon nanotube mechanical resonator. A nanotube segment of length L between source and drain electrodes is suspended above gate electrodes at a distance h_g and can vibrate with position dependent deflection amplitude $u(x)$. (b) Cross section of the same CNT mechanical resonator with field lines of electrostatic potential sketched. Panel (b) adapted from [111].

The first condition simply means that the position of the nanotube is fixed to the electrode surfaces on both ends, while the second condition takes into account the nanotube's bending rigidity by enforcing a continuous slope at the clamping points.

We only mention the solutions for two edge cases here. In the first case, when bending rigidity is dominant ($EI \gg T$), the fourth term of Equation (4.27) is neglected and the CNT behaves like a *beam resonator*. Eigenfrequencies are then given by

$$f_n = \frac{\beta_n^2}{2\pi L^2} \sqrt{\frac{EI}{\rho A}} \quad (4.30)$$

where β_n has to fulfil $\cos(\beta_n) \cosh(\beta_n) = 1$. In the opposite case, where tension is dominant ($T \gg EI$), the nanotube acts as a *string resonator* with eigenfrequencies

$$f_n = \frac{n+1}{2L} \sqrt{\frac{T}{\rho A}} \quad (4.31)$$

External forces on the CNT can be applied via electrostatic interactions with the gate electrode. In a simplified model, the device can be viewed as a conductive cylindrical wire with length L and radius r (the nanotube) above an infinite metallic plane (the gate). The capacitance per unit length is then given by [111]

$$c_g(x) = \frac{2\pi\epsilon_0}{\operatorname{arccosh}\left(\frac{h_g - u(x)}{r}\right)} \quad (4.32)$$

We write the total gate capacitance as

$$C_g = \frac{2\pi\epsilon_0 l_{\text{eff}}}{\operatorname{arccosh}\left(\frac{h_g - u}{r}\right)} \quad (4.33)$$

where l_{eff} is the *effective electronic length* of the nanotube that interacts with the gate, which accounts for corrections due to geometry deviations from the wire over-plane-model. Using the results from quantum dot spectroscopy in the previous section, a CNT-gate distance $h_g = 150$ nm from the device geometry and a typical CNT radius $r = 1.5$ nm we get $l_{\text{eff}} = 322$ nm. Considering that in reality the gate electrode is not an infinite plane, but has a finite width of 150 nm, this result seems reasonable.

A change of gate capacitance due to nanotube deflection is then given by the derivative of C_g with respect to u :

$$C'_g = \left(\frac{dC_g}{du}\right)_{u=0} = \frac{2\pi\epsilon_0 l_{\text{eff}}}{\sqrt{h_g - r} \sqrt{h_g + r} \operatorname{arccosh}^2\left(\frac{h_g}{r}\right)} \quad (4.34)$$

Using the above parameters it can be calculated as $C'_g = 4.3 \times 10^{-12}$ F/m for our device.

4.4.2 Actuation and detection of vibrations

We identify the mechanical modes of our device using the experimental setup shown in [Figure 4.22\(a\)](#). This is an expansion of the setup we used for quantum dot spectroscopy in the previous section. A RF component, supplied by a Rohde & Schwarz SMBV100A signal generator, is added to the dc gate voltage through a bias tee on the sample carrier PCB. As the CNT and gate electrode form a capacitor, the nanotube experiences a force proportional to the square of the applied gate voltage

$$\begin{aligned} F_{\text{drive}} &\propto (V_g + V_g^{\text{ac}} \cos(\omega_{\text{RF}}t))^2 \\ &\propto V_g^2 + 2V_g V_g^{\text{ac}} \cos(\omega_{\text{RF}}t) + \frac{1}{2} (V_g^{\text{ac}})^2 (1 + \cos(2\omega_{\text{RF}}t)) \end{aligned} \quad (4.35)$$

The first term simply causes a static deflection of the nanotube. The second and third terms represent periodic forces on the nanotube, one oscillating at the applied RF drive frequency, the other at twice that frequency. Note that we are neglecting Coulomb blockade here, its effects on CNT mechanical resonances will be discussed in the next section. With typical values for V_g on the order of volts and V_g^{ac} on the order of millivolts or less, the drive force component at ω_{RF} is usually much stronger than the one at $2\omega_{\text{RF}}$. Therefore, resonant responses of the CNT to the $2\omega_{\text{RF}}$ drive component, if detectable at all, are much weaker and can be clearly distinguished from resonances at the applied drive frequency. Referring back to [Equation \(4.31\)](#) for resonant frequencies of an ideal string resonator, one could imagine the ω_{RF} and $2\omega_{\text{RF}}$ components of the drive force exciting two different mechanical modes of the nanotube at the same time. Remember however, that this equation is a theoretical edge case. It is very unlikely that the mechanical modes of a real device are perfectly described by this expression, and we will see in the next section that the mode frequencies of our device deviate enough from this idealised case to rule out parallel excitation of multiple modes.

To characterise mechanical resonances of the CNT we use the *rectification technique*, a method that allows electronic self-detection of the nanotube's motion by transducing deflection into an electric current. We tune the device near the base of a single electron tunnelling conductance peak by setting the dc gate voltage. Then, with a small bias voltage applied to the source, we sweep the frequency of the RF drive tone.

Since the gate capacitance depends on CNT-gate distance (cf. [Equation \(4.32\)](#)),

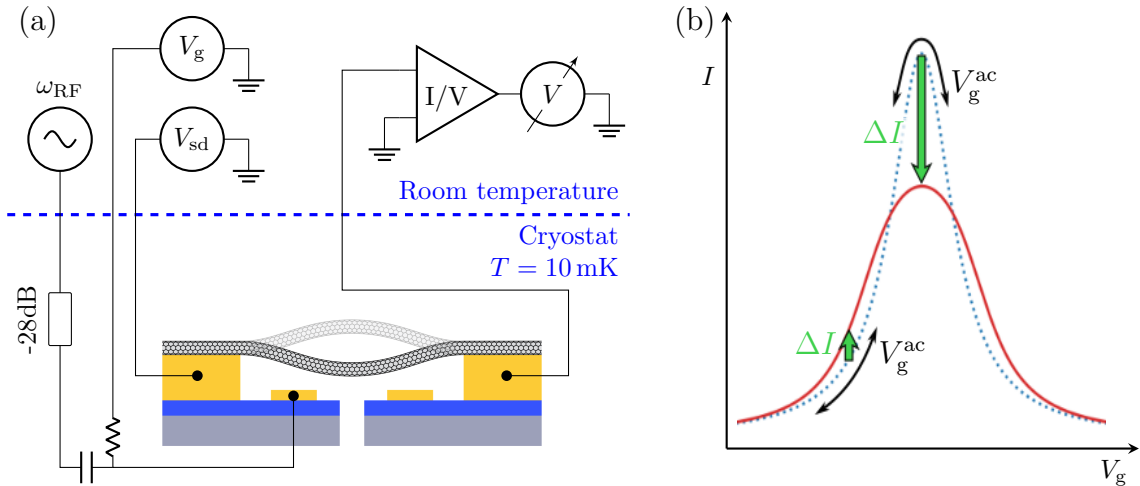


Figure 4.22: Actuation and detection of CNT vibration. (a) The setup for detection of driven CNT vibration is an expansion of the quantum dot spectroscopy setup of Figure 4.19. A RF signal generator is added to supply a drive tone for mechanical vibrations to the gate electrode. RF and dc components of the gate voltage are combined in a bias tee on the sample carrier PCB. (b) Modulations of the gate capacitance C_g^{ac} due to CNT motion can be seen as an effective ac component of gate voltage V_g^{ac} . When measuring the time averaged current near a conductance peak from single electron tunnelling, vibration of the nanotube causes a shift of the measured dc current. Panel (b) adapted from [43].

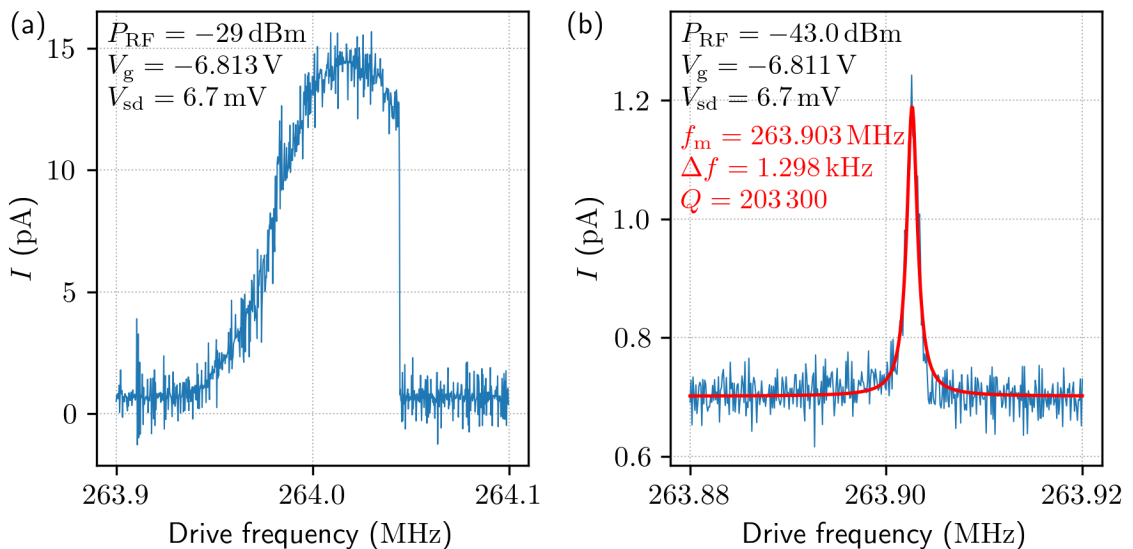


Figure 4.23: Mechanical resonance curves for high (a) and low (b) drive power. In both measurements, the drive frequency is swept across the mechanical resonance at constant gate and bias voltages. For high drive power (a), the resonance is broad and highly non-linear. At low drive power (b) the resonance fits nicely to a Lorentzian with a quality factor of $Q = 203300$.

vibrations of the nanotube add a deflection dependent ac component C_g^{ac} to the otherwise static capacitance C_g^{dc} and the total gate capacitance becomes $C_g = C_g^{\text{dc}} + C_g^{\text{ac}}$. When the nanotube motion is driven on resonance ($\omega_{\text{RF}} = \omega_m$), the vibration amplitude u_0 and thus $C_g^{\text{ac}}(t) = (dC_g/du)u_0 \cos(\omega_m t)$ becomes large.

From Equation (4.17) we can see that the tuning of the CNT quantum dot levels and thus device conductance depends on the *gate induced charge* $q_c = C_g V_g$. We use this to rewrite the modulation of gate capacitance as an effective ac component of the gate voltage $V_g^{\text{ac}} = \frac{C_g^{\text{ac}}(t)}{C_g} V_g$. A Taylor expansion of the current with respect to gate voltage then leads to [45]

$$\begin{aligned}
 I(V_g + V_g^{\text{ac}}(t)) &= I(V_g) + \frac{dI}{dV_g} \frac{V_g}{C_g} \frac{dC_g}{du} u_0 \cos(\omega_{\text{RF}} t) \\
 &+ \frac{1}{2} \frac{d^2 I}{dV_g^2} \left(\frac{V_g}{C_g} \frac{dC_g}{du} \right)^2 u_0^2 \left(\frac{1}{2} + \frac{1}{2} \cos(2\omega_{\text{RF}} t) \right) + \mathcal{O}(u_0^4)
 \end{aligned} \tag{4.36}$$

Due to the low bandwidth in our measurement of dc current, only time-averaged currents are detected in our setup. Omitting high frequency terms, we are left with a dc current shift

$$\Delta I = \frac{1}{4} \frac{d^2 I}{dV_g^2} \left(\frac{V_g}{C_g} \frac{dC_g}{du} \right)^2 u_0^2 \tag{4.37}$$

due to mechanical motion. In order to get a large mechanical signal, $\frac{d^2 I}{dV_g^2}$ must be large, which is the case for sharp conductance peaks in the Coulomb blockade regime. The current shift is negative on top of a Coulomb peak and positive near the base of a Coulomb peak, see Figure 4.22(b) for visualisation.

Example measurements of mechanical resonance are shown in Figure 4.23. A constant bias voltage of 6.7 mV is applied and the gate voltage is tuned to the flank of a Coulomb peak at about -6.81 V. We sweep the frequency of the RF drive tone at constant power and continuously measure the current. For a large drive power of $P_{\text{RF}} = -29$ dBm¹³ (see Figure 4.23(a)) the resonance peak is wide and clearly non-linear, consistent with the response of a Duffing type resonator [43]. At lower powers ($P_{\text{RF}} = -43$ dBm, Figure 4.23(b)), the resonator response becomes more linear. From a Lorentzian fit we obtain a mechanical resonance frequency of $f_m = 263.903$ MHz, a line width of $\Delta f = 1.298$ kHz, and thus a mechanical quality factor of $Q_m = f_m/\Delta f = 203\,300$.

¹³Drive powers are given as output level of the signal generator at room temperature.

4.4.3 Frequency tuning and electromechanical backaction

Just like the RF component of the gate voltage results in an oscillating force on the nanotube for driving its motion, the dc gate voltage also results in an electrostatic force which we can express as derivative of the electrostatic energy U

$$F_{\text{el}} = \frac{\partial U}{\partial z} = \frac{1}{2} \frac{dC_{\text{g}}}{dz} (V_{\text{g}} - V_{\text{CNT}})^2, \quad (4.38)$$

where V_{CNT} is the voltage on the carbon nanotube. This force pulls the nanotube towards the gate and increases tension, which allows tuning of the nanotube like a guitar string. Although the relation between mechanical frequency f_{m} and gate voltage V_{g} in general is more complex [111], it often is reasonably well described by a simple quadratic relation [113].

For the device investigated in this thesis, a number of mechanical modes were found, all of which are shown in Figure 4.24. We see pairs of strong resonances around 260 MHz, 520 MHz and 795 MHz. For very high drive powers, additional faint resonances appear in the vicinity of these modes and also around 130 MHz and 65 MHz. No resonances below 65 MHz were found. Since the fainter resonances are only visible at very high drive powers, they likely are parametric excitations of other modes or resonant responses to the $2\omega_{\text{RF}}$ component of the drive force, although this has not been investigated in detail, yet. Therefore, we assume that the 260 MHz mode is the fundamental resonance.

Interestingly, all resonances seem to appear as pairs of modes. Similar “twin mode” behaviour has been observed by others (e.g., [12, 48]), and is usually attributed to the same mode shape oscillating in two orthogonal directions (one mostly parallel to the gate electrode, the other mostly towards the gate).

All modes fit nicely to a parabolic dispersion of the form

$$f_i(V_{\text{g}}) = a_i (V_{\text{g}} - V_{\text{g}0,i})^2 + f_{0,i} \quad (4.39)$$

Fit results are overlaid as dashed lines on the plots in Figure 4.24(a)-(e) and results for the fit parameters are summarised in Table 4.3. One might intuitively expect a centre gate voltage of $V_{\text{g}0} = 0$ V for all modes, but a common offset can be explained, for example, by static charges on the substrate surface. The obtained centre gate voltages for this device are scattered over quite a large range. This may to some degree be an error from extrapolation, since we can only see one side of the parabolic dispersion (we cannot see mechanical resonances for positive gate voltages, because the device does not conduct there). A similar relative shift of mechanical modes in V_{g} was observed in Ref. [48], also with no straightforward explanation.

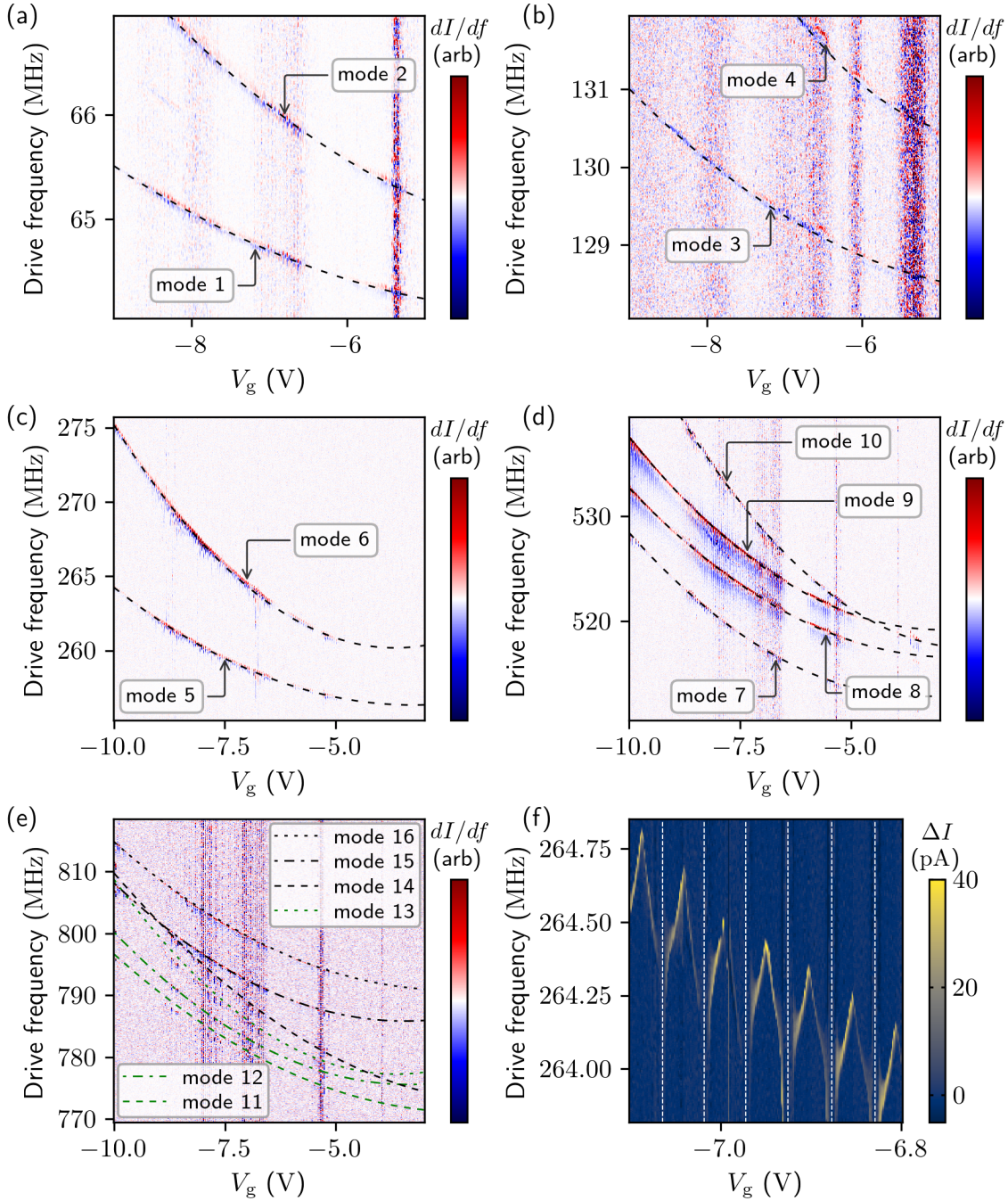


Figure 4.24: (a-e) Large scale plots of all detected mechanical resonances of the device. At fixed bias voltage, time averaged current through the device is recorded as function of gate voltage and frequency of a strong drive tone. Resonances appear as current shift. Resonance frequencies were extracted and fitted to Equation (4.39) (dashed lines, see Table 4.3 for fit parameters). (To make resonances clearer, data has been lowpass filtered and numerically differentiated with respect to drive frequency in each column.) (f) Detail plot of mode 6 in a smaller gate voltage range covering six Coulomb blockade oscillations (dashed lines). Going across each conductance peak, the mechanical mode exhibits spring softening and a reduction of quality factor from interaction with single electron tunnelling. (To make the resonance clearer, data in each column was lowpass filtered and the average of each column has been subtracted.)

With our assumption that mode 5 is the fundamental resonance, we can use the fit result for the extremum of the dispersion $f_{0,5} = 256.33$ MHz together with Equation (4.31) to estimate the imprinted tension of the device. Using $L = 1.1$ μm (source-drain electrode distance) and $\rho = 1350$ kg/m^3 , $A = 7.1$ nm^2 (typical values for CNTs [45]) we obtain a tension of $T = 3.05$ nN, most likely resulting from the CNT stamp transfer step in the fabrication process.

A detailed measurement of mode 6, shown in Figure 4.24(f), reveals another distinct feature of CNT NEMS mechanical resonances, namely *electromechanical backaction* from coupling between nanotube motion and the quantum dot on the nanotube. To understand this, we use Equation (4.38) to calculate the change of spring constant due to single electron tunnelling. Following Ref. [45], we use $V_{\text{CNT}} = (C_g V_g + q_{\text{CNT}})/C_{\text{dot}}$ with the charge on the CNT $q_{\text{CNT}} = -e \langle N \rangle$ and obtain

$$\Delta k = -\frac{dF_{\text{el}}}{dz} \approx \frac{V_g(V_g - V_{\text{CNT}})}{C_{\text{dot}}} \left(\frac{dC_g}{du} \right)^2 \left(1 - e \frac{d\langle N \rangle}{dq_c} \right) \quad (4.40)$$

where $q_c = C_g V_g$ is the gate induced charge (i.e., the charge on the nanotube if it were a simple conductive wire without Coulomb blockade) and terms slowly varying with $d^2 C_g / du^2$ have been neglected. Using $\Delta k = 2m\omega_m \Delta\omega_m$ we arrive at the frequency shift due to single electron tunnelling

$$\Delta\omega_m = \frac{V_g(V_g - V_{\text{CNT}})}{2m\omega_m C_{\text{dot}}} \left(\frac{dC_g}{du} \right)^2 \left(1 - e \frac{d\langle N \rangle}{dq_c} \right) \quad (4.41)$$

When the device is in Coulomb blockade, the average charge occupancy is fixed and $\frac{d\langle N \rangle}{dq_c}$ is zero. The remaining first term of Equation (4.40) represents the tension that gives rise to the large scale frequency tuning previously discussed. When Coulomb blockade is lifted at a charge transition, $\frac{d\langle N \rangle}{dq_c}$ becomes positive, leading to spring softening and reduced resonance frequency. The effect is stronger for sharper charge transitions with steeper $\frac{d\langle N \rangle}{dq_c}$.

The stochastic electrostatic force from electrons hopping on and off the quantum dot at a charge transition can also cause damping of the mechanical motion [45]. This can also be observed in Figure 4.24(f) as broadening of the resonance peak in the vicinity of conductance peaks.

CB diamond edge slopes	λ_1	[1]	-0.52 ± 0.05
	λ_2	[1]	0.44 ± 0.05
Gate lever arm	α_g	$(1/ \lambda_1 + 1/ \lambda_2)^{-1}$	0.24 ± 0.02
Source lever arm	α_s	$\alpha_g/ \lambda_1 $	0.46 ± 0.03
Gate capacitance	C_g	$e/\Delta V_g$	3.38 ± 0.06 aF
Total capacitance	C_{dot}	C_g/α_g	14.4 ± 1.1 aF
Source capacitance	C_s	$\alpha_s C_{\text{dot}}$	6.6 ± 0.5 aF
Charging energy	E_C	e^2/C_{dot}	11.2 ± 0.8 meV
Effective electronic length	l_{eff}	Eq. (4.33)	~ 322 nm
C_g change from deflection	C'_g	Eq. (4.34)	~ 4.3 pF/m

Table 4.2: Overview of CNT device parameters extracted from Coulomb blockade and mechanical resonance data. ^[1] From Coulomb blockade data near $V_g = -7$ V.

mode #	mode curvature a_i [kHz/V ²]	mode centre voltage $V_{g0,i}$ [V]	mode centre frequency $f_{0,i}$ [MHz]
1	43.5 ± 1.2	-3.35 ± 0.10	64.122 ± 0.016
2	67 ± 4	-2.6 ± 0.3	64.81 ± 0.07
3	98 ± 6	-3.86 ± 0.19	128.40 ± 0.06
4	270 ± 50	-4.4 ± 0.3	130.40 ± 0.13
5	174 ± 2	-3.26 ± 0.06	256.33 ± 0.04
6	374 ± 5	-3.67 ± 0.05	260.18 ± 0.07
7	362 ± 5	-3.43 ± 0.07	512.79 ± 0.11
8	305 ± 7	-2.72 ± 0.12	516.54 ± 0.17
9	371 ± 4	-2.97 ± 0.05	519.17 ± 0.08
10	510 ± 50	-2.3 ± 0.4	517 ± 1
11	400 ± 110	-2.0 ± 1.5	771 ± 3
12	560 ± 110	-3.3 ± 0.8	775.6 ± 1.8
13	770 ± 80	-3.6 ± 0.4	777.3 ± 1.2
14	460 ± 110	-1.0 ± 1.6	773 ± 5
15	520 ± 40	-3.4 ± 0.4	785.8 ± 0.7
16	420 ± 60	-2.4 ± 0.8	790.9 ± 1.6

Table 4.3: Summary of fit parameters from fitting extracted resonance frequencies from Figure 4.24(a)-(e) to Equation (4.39).

Chapter 5

Carbon nanotube vibration readout with a Josephson travelling wave parametric amplifier

The aim of this thesis is taking steps towards improving the sensitivity of MRFM experiments. Exploring different detector architectures, like the CNT NEMS based one introduced in the previous chapter, is only one contribution towards that goal. Since noise in the rest of the system can also have a tremendously negative impact on measurement sensitivity, it is equally important to implement a low-noise readout scheme for any given detector.

Vibration detection of a CNT via the rectification technique used in the previous chapter is therefore possibly the worst choice. The tiny shifts in dc current from small amplitude vibrations are easily drowned in $1/f$ noise. Reasonably sensitive measurements can only be achieved with low measurement bandwidths and long integration times. For example, mechanical resonance data in the previous chapter was recorded with integration times on the order of 60–200 ms per data point, which was barely enough to resolve resonances of the fundamental mode (the one with the strongest response signal) without pushing the resonator into the non-linear regime by applying excessive driving forces.

Having a nearly quantum limited amplifier installed in our cryostat (the TWPA, see [Chapter 3](#)), it seems only natural to try and use it as primary amplifier for our CNT vibration readout. To the best of the author's knowledge, detection of nanotube motion with a TWPA has not been attempted before. In this chapter we begin exploring whether readout in the MW regime with a TWPA as primary amplifier is a viable option for a CNT NEMS based force detector.

5.1 A carbon nanotube as an electromechanical mixer

The first issue with CNT vibration readout through our TWPA is immediately obvious. Typical mechanical frequencies of CNTs are on the order of tens to hundreds of MHz with only few exceptional devices or higher resonator modes reaching the GHz range, and our device is no exception, as we have seen in the previous chapter. However, our TWPA and MW readout electronics only work in the frequency band between 4–7.5 GHz (cf. [Chapters 2 and 3](#)), which means we cannot detect nanotube motion directly at the resonance frequency.

We can solve this by switching to another commonly used electronic self-detecting readout method, the *electromechanical mixing technique*. To understand this technique, we again consider the current $I = GV_{\text{sd}}$ flowing through the nanotube, where G is the device conductance and V_{sd} is the bias voltage applied across the source and drain electrodes. As previously discussed, the conductance depends on the gate induced charge $q_c = C_g V_g$. An oscillating component V_g^{ac} of the gate voltage (e.g., for driving nanotube vibrations) directly modulates the gate induced charge, $q_c^{\text{el}}(t) = C_g V_g^{\text{ac}}(t)$. Additionally, mechanical motion of the nanotube changes q_c via a modulation of the gate capacitance, $q_c^{\text{mech}}(t) = C_g^{\text{ac}}(t) V_g$ with $C_g^{\text{ac}}(t) = \frac{dC_g}{du} u_{\text{ac}} \cos(\omega_{\text{RF}} t)$, where u is the nanotube deflection and ω_{RF} is the frequency of the drive signal and mechanical motion. Combining these two contributions, we get the time-dependent component of the conductance

$$G^{\text{ac}}(t) = \frac{dG}{dV_g} \left(V_g^{\text{ac}}(t) + \frac{C_g^{\text{ac}}(t)}{C_g} V_g \right) \quad (5.1)$$

When the bias voltage is also modulated, but at frequency ω_{MW} , the current at the drain electrode contains a component $I_{\text{mix}} = G^{\text{ac}}(t) V_{\text{sd}}^{\text{ac}}(t) \propto \cos(\omega_{\text{RF}} t) \cos(\omega_{\text{MW}} t)$. The input signals are mixed and the drain current contains components at the sum and difference frequencies of the inputs. This scheme is often used to *down convert* mechanical frequencies into a range that can be conveniently measured with a lock-in amplifier (typically a few kHz), see for example [[82](#), [110](#), [114](#)]. Here we use the same approach to *up convert* the frequency of mechanical vibrations into the frequency band of our TWPA and MW readout circuitry. We pick a frequency $f_{\text{MW}} = 2\pi\omega_{\text{MW}} = 5$ GHz for the *probe tone* applied to the source electrode. Mixing with the mechanical modes identified in the previous chapter, actuated by a *drive tone* with frequency $f_{\text{RF}} = 2\pi\omega_{\text{RF}}$, creates sidebands at the sum frequencies between 5–6 GHz, within the frequency band of the TWPA and MW readout.

5.2 Build-up of experimental setup

All terminals of our CNT NEMS device connect to bias tees on the sample carrier PCB. Thus, in a first naive attempt of implementing the mixing technique for CNT vibration detection, the previous setup in [Figure 4.22\(a\)](#) was expanded by adding a MW probe tone from a second signal generator to the bias voltage through the bias tee connecting to the source electrode. The RF branch of the bias tee on the drain electrode was then fed into the MW readout electronics with the TWPA as first amplifier. A small fixed dc bias voltage of $V_{sd} \lesssim 10$ mV was set and the frequency of the drive signal f_{RF} on the gate electrode and the dc gate voltage V_g were swept across parameter regions where we expect mechanical resonances from the device characterisation in the previous chapter. The output of the MW readout line was monitored with a spectrum analyser at the sideband frequency $f_{RF} + f_{MW}$. A strong signal was detected at the sideband, however, the received power was more or less constant across the swept ranges of V_g and f_{RF} and did not show any characteristic features of the CNT device (Coulomb blockade or mechanical resonances).

Setting the spectrum analyser to record at the frequencies of the input signals f_{RF} and f_{MW} , it was found that substantial parts of both of these signals are transmitted to the MW readout. Considering that the source, drain and gate electrodes in our device design are long parallel strips of metal, transmission of input signals to the drain is facilitated by large amounts of capacitive and inductive crosstalk between electrodes.

Here we have to remember that, besides the CNT device, we have a second non-linear component in the setup, namely the TWPA (cf. [Chapter 3](#)). Parts of the input signals that leak into the MW readout can also mix in the amplifier, producing a signal at the same sideband frequency as electromechanical mixing in the CNT. Mixing in the TWPA can be confirmed by coupling the drive and probe tones into the TWPA pump line, so that they can still interact with the amplifier, but not with the nanotube. With the power levels of input tones set to reproduce the levels received by the spectrum analyser in the original setup, the power received at the mixer sideband is also roughly reproduced, indicating that the vast majority of mixing is happening in the TWPA. In hindsight, this should not come as a surprise, since the nanotube is a tiny high-impedance link between electrodes with likely large capacitive and inductive coupling, which means only a small fraction of input signals will travel through and interact in the nanotube while a much larger portion will be directly transmitted to the readout circuit and mix there. Furthermore, for strong drive or probe tones the power level of transmitted input tones could be high enough to saturate the TWPA (the datasheet states a 1 dB compression point at only -100 dBm input power, although this has never been confirmed in

our system). Thus, any weak signals from CNT electromechanical mixing that we might be receiving are drowned out by mixing in the TWPA of input tones leaked past the nanotube.

In order to have a chance of observing the signal from electromechanical mixing, we need a way of stopping the leaked input signals from reaching the TWPA. One could imagine adding a cryogenic highpass filter between the device and amplifier to filter out the RF drive tone. Finding a similar filter for the MW probe tone would be more difficult, simply because suitable filters in that frequency range are much harder to find, especially considering that our signal of interest, the mixer sidebands, can be relatively close to the probe tone in frequency space, which means the filter would need a very steep roll-off to achieve sufficient suppression of probe tone leaks. An on-chip bandstop or notch filter might be a more suitable solution [115]. However, adding new circuit components to the cryostat wiring requires identifying and buying suitable components, as well as a thermal cycle of the cryostat for installation. Implementation of on-chip filters needs a new iteration on device design and another run of the quite lengthy device fabrication process (cf. Section 4.2). Both options are quite time consuming and require careful planning in advance, which would cause significant delay to the experiment. Thus, these approaches should be considered long-term solutions for future runs of the same or a similar experiment.

In the current run of the experiment we solve the issue of input tone mixing in the TWPA by adding complexity to the room temperature circuitry. The full setup is shown in Figure 5.1.

The sections for supplying dc voltages (V_{sd} and V_g) and measuring dc current are identical to the setup in Section 4.3.2, using modules of a QuTech IVVI-DAC2 rack and a Keithley 2100 digital multimeter.

Similar to the setup for CNT vibration detection via the rectification method in Section 4.4.2, the RF drive tone comes from a Rohde & Schwarz SMBV100A signal generator and is added to the gate voltage through a bias tee on the sample carrier PCB. However, the signal generator output is now split into two branches by a Mini-Circuits ZESC-2-11+ power splitter. We will refer to the RF branch that connects to the gate as *RF drive* and the second branch as *RF cancel*, more on that in a moment. In a similar configuration, a second signal generator (Rigol DSG3136B) supplies a MW tone, which is split into *MW probe* and *MW cancel* branches by a Mini-Circuits ZFRSC-183-S+ power splitter. The MW probe branch connects to the device's source electrode through a bias tee on the sample carrier PCB.

A third bias tee of the sample carrier converts any high frequency components of the drain current into voltage signals and couples them into the cryostat's MW readout line. The configuration of the MW readout electronics is identical to the

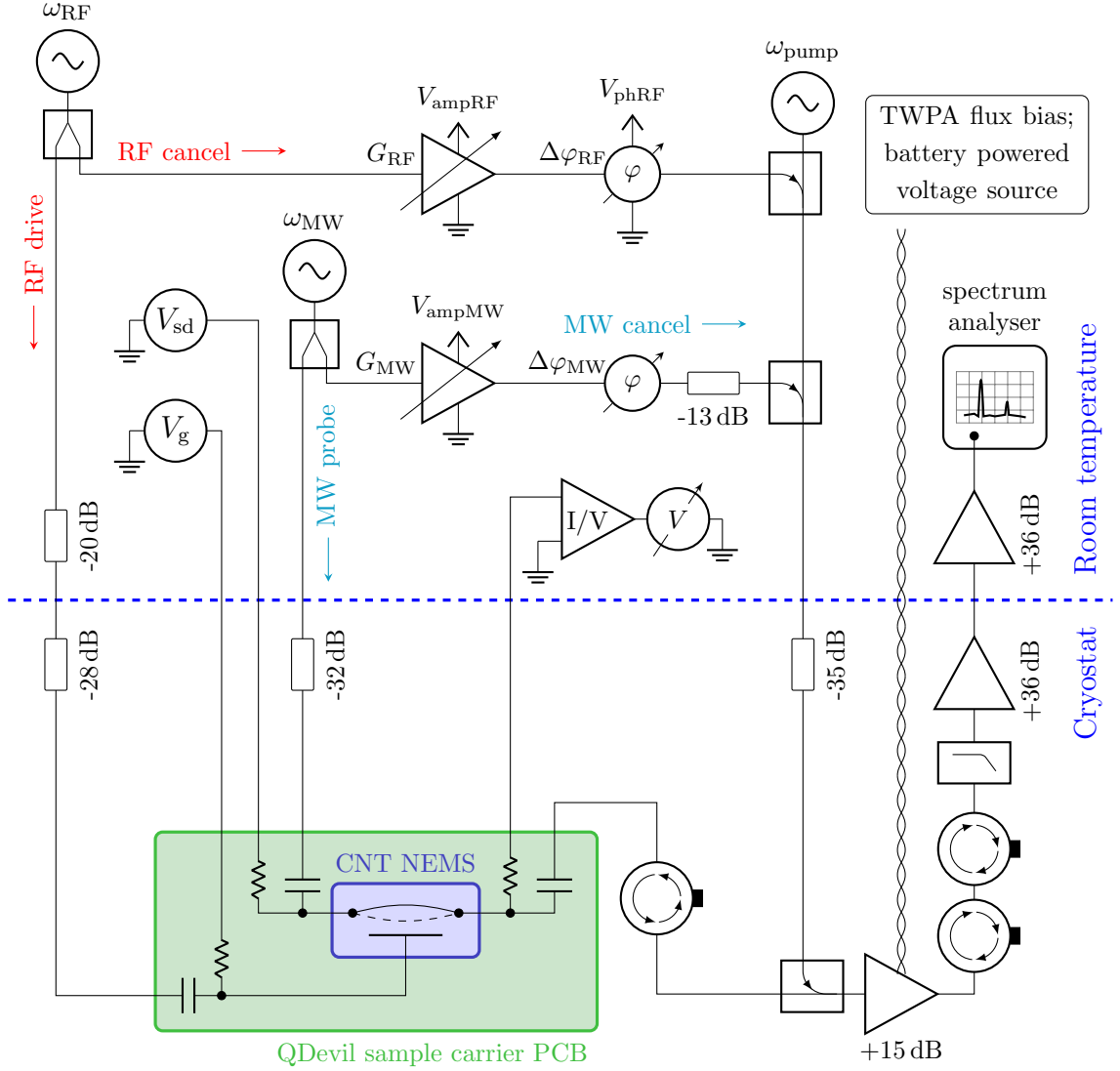


Figure 5.1: Measurement setup for CNT electromechanical mixing readout with a TWPA. Bias and gate voltages are supplied from battery powered low-noise voltage sources and dc current through the device is measured with a transimpedance amplifier and digital multimeter. RF and MW input tones from two signal generators are split into drive/probe and cancel branches. The RF drive and MW probe are added to the gate and bias voltage through bias tees on the sample carrier PCB. A third bias tee connected to the drain electrode couples high frequency components of the drain current into the MW readout electronics where they are amplified by the TWPA at 10 mK, a HEMT amplifier at 4 K and an additional low-noise amplifier at room temperature before being detected with a spectrum analyser. The TWPA is pumped from a third signal generator and the dc flux bias is supplied from a battery powered voltage source. Amplitude and phase on the RF and MW cancel branches can be tuned with amplifiers and phase shifters. Cancel branches are coupled into the TWPA pump line to suppress transmitted drive/probe tones via destructive interference before they reach the amplifier. Additional room temperature attenuators balance the input and cancel branches for optimal signal suppression before the TWPA. Attenuators inside the cryostat are shown as total line attenuation, see Section 2.3 for details.

setup used for characterisation of the TWPA in Section 3.4. The first amplifier at 10 mK is the TWPA, operated with a pump tone (12 GHz, -2.6 dBm) from a Windfreak SynthHD signal generator and flux bias current (819 μ A) from a battery powered voltage source. Additional amplification is provided by a Low Noise Factory LNF-LNC0.3_14A HEMT at 4 K and a Narda LNA-30-04001200-15-10P low-noise amplifier at room temperature. Signals in the MW readout line are detected with a Rohde & Schwarz FSV3044 spectrum analyser.

Coming back to the RF and MW cancel branches, the amplitude and phase on both these paths can be tuned with amplifiers (Mini-Circuits ZX60-33-LN-S+ for RF, Mini-Circuits ZX60-24A-S+ for MW)¹⁴ and phase shifters (Mini-Circuits ZXPHS-431-S+ for RF, ARRA Inc. 9428A mechanical phase shifter for MW). The cancel branches are then coupled into the TWPA pump line via directional couplers (Pasternack PE2210-10 for RF, Pasternack PE2210-20 for MW). Signals from the sample space and the TWPA pump are combined via a directional coupler and enter the amplifier through the same port. Therefore, by appropriately tuning the amplitude and phase on both cancel branches, components of the RF drive and MW probe tones that leaked into the readout circuit can be suppressed by destructive interference before reaching the amplifier. Amplitude and frequency of the MW probe tone will be constant within each measurement, meaning that the MW cancel branch only needs to be tuned once at the beginning, which makes manual tuning of the mechanical phase shifter and amplifier supply voltage V_{ampMW} (supplied by a Keithley 2280S power supply) acceptable. In contrast, the RF drive frequency is a varying parameter in most experiments, thus requiring constant retuning of the RF cancel branch. Therefore, the amplifier supply voltage V_{ampRF} and phase shifter control voltage V_{phRF} come from a Keithley 2450 SourceMeter and IVVI DAC channel, respectively, and can be adjusted as part of the measurement automation. Additional fixed attenuators are added at room temperature to balance the drive/probe and cancel branches for optimal signal suppression.

We will see in the next section that with this setup transmission of input signals and mixing in the TWPA can be suppressed enough to reveal features of the CNT NEMS device in the mixed signal as well as in the transmission of the drive and probe tones.

¹⁴These amplifiers are low noise linear amplifiers, not designed for applications like the one presented here, where signal amplitudes need to be precisely tuned. In the future, these should be replaced with proper variable gain amplifiers or chained with variable attenuators.

5.3 Mechanical resonances detected through electromechanical mixing

The procedure for a measurement run with the above described setup is as follows. First, a power P_{MW} and frequency f_{MW} for the MW probe tone is chosen. In the work presented here we always use $f_{\text{MW}} = 5 \text{ GHz}$. P_{MW} may vary between measurements to achieve best SNR, but always remains constant within a measurement run. Additionally, we chose an amplitude P_{RF} ¹⁵ for the RF drive tone and a range of frequencies for sweeping the drive frequency f_{RF} .

Before the measurement itself can begin, both cancel branches need to be tuned for the chosen set of experimental parameters. For this, the bias voltage is set to $V_{\text{sd}} = 0 \text{ V}$ and the gate voltage is set so that the device is in Coulomb blockade and no mechanical resonances are in the chosen range of f_{RF} . Now any signals detected by the spectrum analyser at frequencies f_{RF} and f_{MW} must have travelled through parasitic paths from crosstalk between device electrodes, and any signal at $f_{\text{mix}} = f_{\text{RF}} + f_{\text{MW}}$ must be from mixing in the TWPA. While observing the power received by the spectrum analyser at f_{MW} , phase and amplitude on the MW cancel branch are adjusted to minimise the transmitted signal. Similarly, the RF cancel branch is calibrated to minimise transmission of signals at f_{RF} for a few points within the range of the experiment. Parameters for RF cancellation for every setpoint of the experiment are later obtained by interpolation. Old calibration data can be reused when measurements are repeated within the same parameter range.

For the actual experiment, a small bias voltage is set ($V_{\text{sd}} = 7 \text{ mV}$ for all experiments in this chapter) and V_{g} and f_{RF} are swept. The spectrum analyser records the power at the mixer sideband $f_{\text{mix}} = f_{\text{RF}} + f_{\text{MW}}$, while the dc current through the device is also simultaneously measured. Example data for the higher frequency branch of the twin fundamental mechanical mode (cf. [Section 4.4.3](#)) near $V_{\text{g}} = -6.9 \text{ V}$ is shown in [Figure 5.2](#).

Transmission of the RF and MW tones in [Figure 5.2\(a\)](#) and [\(b\)](#) were recorded in separate repetitions of the experiment and are only shown for reference. We see a very faint signature of the CNT mechanical resonance at f_{RF} ([Figure 5.2\(a\)](#), compare to [Figure 4.24\(f\)](#)) due to conductance modulation caused by the nanotube motion (cf. [Equation \(5.1\)](#)). It is somewhat surprising that this can be observed in our setup, since the mechanical frequencies of the device are far outside the designed frequency band of the MW readout line. Luckily, looking at system characterisation

¹⁵To keep numbers directly comparable with the previous chapter, RF drive powers are given as they enter the cryostat, subtracting losses of about 24 dB caused by the added room temperature circuitry from the signal generator output level.

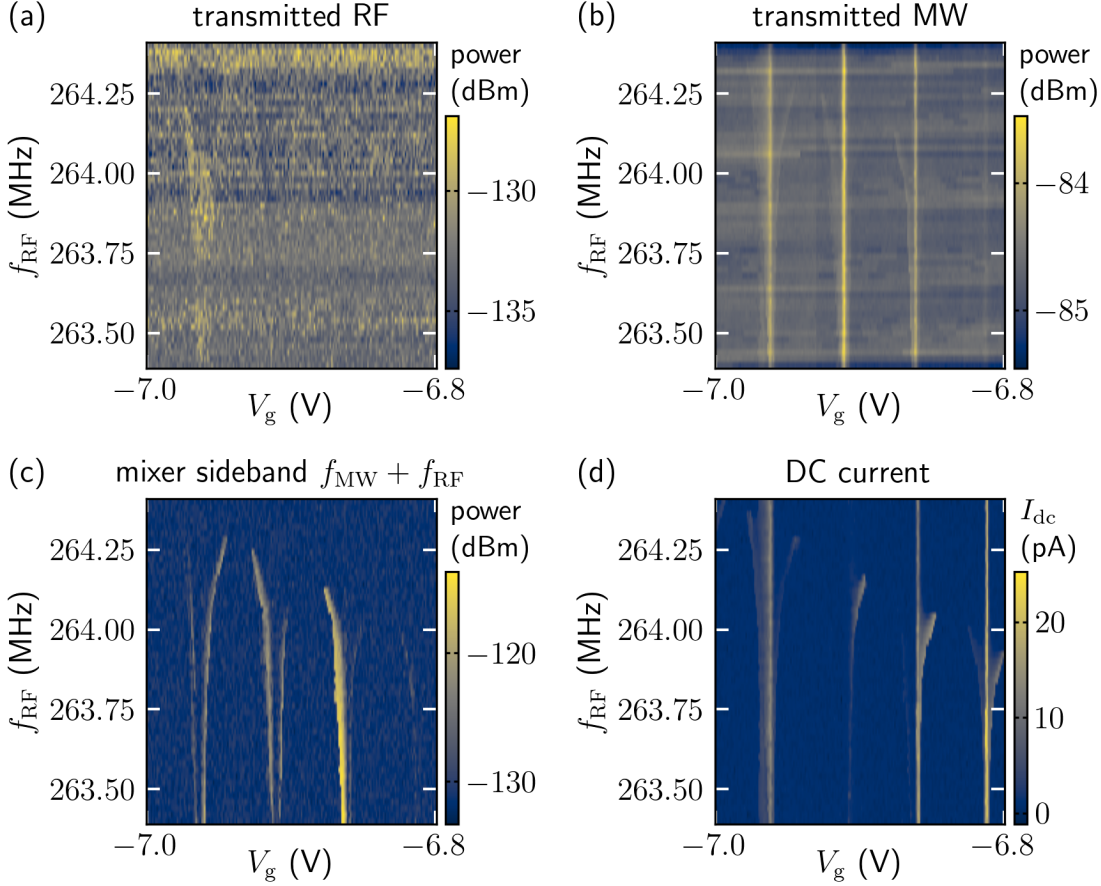


Figure 5.2: Signal components at different frequencies in the CNT electromechanical mixer experiment. (a) Despite being far outside the frequency band of the MW readout electronics, a faint signature of CNT mechanical resonance is visible in the transmitted RF drive tone. (b) Transmission of the MW probe tone increases when Coulomb blockade is lifted and the device becomes conductive. The mechanical resonance can also be seen, but is much more faint. (c) Electromechanical mixing produces a clear signal of the nanotube mechanical resonance at the sum frequency $f_{\text{RF}} + f_{\text{MW}}$. (d) A simultaneous measurement of the dc current reproduces the results from the previous chapter, showing both Coulomb blockade and mechanical resonance. Features in the dc and high frequency signals align nicely. Panels (c) and (d) were recorded simultaneously, panels (a) and (b) were recorded for reference in separate measurement runs. Experimental parameters were: $V_{\text{sd}} = 7$ mV, $P_{\text{RF}} = -28$ dBm, $P_{\text{MW}} = -30$ dBm, $f_{\text{MW}} = 5$ GHz and integration times of 100 ms for both dc and high frequency signals.

data in [Figure 2.4\(b\)](#), signal transmission is still possible at lower frequencies, even with some positive gain below 1 GHz.

Transmission at f_{MW} ([Figure 5.2\(b\)](#)) also shows characteristics of the device, and since this tone lies within the MW readout frequency range features are much clearer. Switching of the quantum dot between Coulomb blockade and finite conductance can clearly be seen as vertical lines of increased signal transmission. Evidence of mechanical resonance is also present, albeit much more faint.

[Figure 5.2\(c\)](#) shows our signal of interest, the power at the mixer sideband frequency $f_{\text{mix}} = f_{\text{RF}} + f_{\text{MW}}$. The mechanical resonance is clearly visible, with a much higher SNR than any features in other frequency bands, confirming that electromechanical mixing in our device works. In addition to lining up with one of the mechanical modes observed in [Section 4.4.3](#)¹⁶, frequency tuning with V_g and mode softening when Coulomb blockade is lifted confirms that the observed features are indeed mechanical resonances of our CNT device.

For reference, the dc current simultaneously recorded with the sideband signal of [Figure 5.2\(c\)](#) is shown in [Figure 5.2\(d\)](#). The results from [Figure 4.24\(f\)](#) are reproduced (except for a small drift in gate voltage over the course of several months that separate the two measurements), showing both features of Coulomb blockade and CNT mechanical resonance. All features observed in the different frequency bands nicely line up with their corresponding counterparts observed at other signal frequencies.

Note that the areas of strongest signal from mechanical resonance are different for the two detection methods. This should be expected, since according to [Equation \(4.37\)](#) the rectification technique produces the strongest signal where d^2I/dV_g^2 is large, i.e., at the base and apex of Coulomb oscillations. In contrast, as can be seen from [Equation \(5.1\)](#), the signal in the mixing technique is strongest for large dG/dV_g , which is the case on the flanks of Coulomb oscillations.

We now pick the Coulomb oscillation near $V_g = -6.86$ V, around which the mechanical resonance signal is particularly strong in both detection methods, and repeat the previous experiment over a smaller parameter range, but with higher resolution, recording both dc current and power at the mixing sideband. A comparison of two measurements, one with a strong RF drive tone and one with weak driving, is shown in [Figure 5.3](#). As expected for the strong drive ([Figure 5.3\(a\)](#) and [\(b\)](#)), the nanotube mechanical resonance is clearly visible in both detection methods and the resonator response looks non-linear. For the low drive power, the mechanical

¹⁶Due to a small drift in gate voltage over the course of a few months between the measurements, Coulomb blockade features are slightly shifted and parameters for achieving the strongest signal from mechanical resonances have slightly changed. Mechanical frequencies still match.

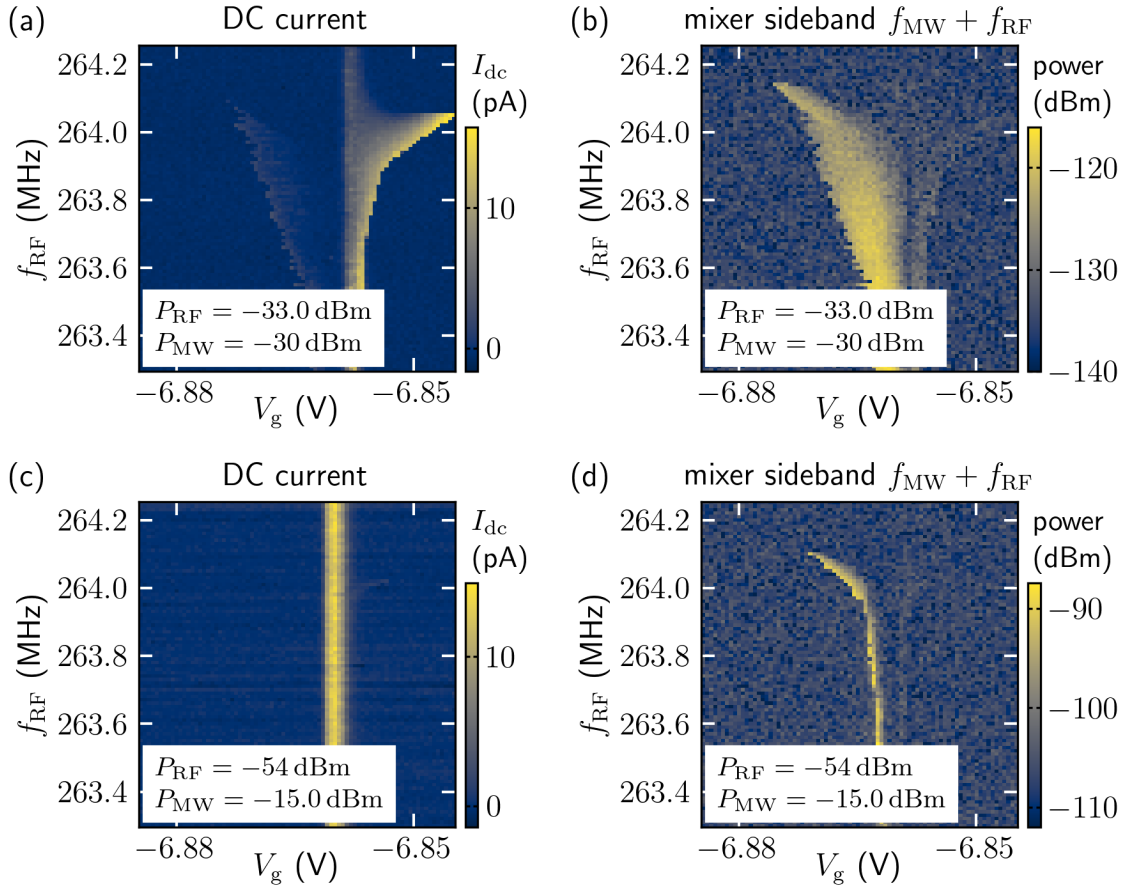


Figure 5.3: Comparison of CNT vibration detection in the rectification and mixing techniques at high ((a) and (b)) and low ((c) and (d)) drive powers. For high drive power the response of the mechanical resonator is clearly non-linear and visible in both the dc current (a) and the mixing sideband (b). At low drive power, the dc current shows mainly the Coulomb blockade conductance peak and only the faintest hint of mechanical resonance (c), while the (now much more linear) mechanical signal is still very prominent in the mixing sideband (d). All panels were recorded with $V_{sd} = 7$ mV, $f_{MW} = 5$ GHz and integration times of 100 ms. Qualitatively, the mixing method detects nanotube motion with significantly higher sensitivity than the rectification method.

resonance is barely picked up in the dc current. However, with increased MW probe tone power, it is still detectable in the mixing technique with a reasonably good SNR of up to about 10–15 dB.

It was made sure that all panels of [Figure 5.3](#) were recorded with identical integration times of 100 ms per point. This suggests, for a preliminary conclusion anyway, that the mixing technique combined with readout through a TWPA can detect mechanical oscillations of a CNT with significantly higher sensitivity than the rectification technique. A more thorough and quantitative analysis of the measurement sensitivity requires collection of more data, but seems worth doing in the future.

5.4 Carbon nanotube oscillation without external drive

While testing the limits for detecting small amplitude (i.e., weakly driven) CNT mechanical resonance, it was found that – at least for some narrow parameter regions around the fundamental mode where the resonance is sharp and bright – with high enough probe tone power of $P_{\text{MW}} \approx -18$ dBm a peak at the electromechanical mixing sideband could still be detected in the power spectral density (PSD) of the MW readout, even without any RF drive signal (see [Figure 5.4\(a\)](#)). In this section we discuss a first attempt of studying the temperature dependence of these non-driven oscillations, which was made hoping that it would allow conclusions on the origin of the oscillations or reveal device parameters that otherwise have to be roughly estimated from typical device dimensions.

Effect of temperature on the MW readout

Before we begin the discussion of nanotube oscillations, another aspect of the experiment needs to be addressed. Over the course of the experiment, while data similar to [Figure 5.4\(a\)](#) was recorded for temperatures up to 4 K, a weak reference tone at $f_{\text{ref}} = 5.266$ GHz, close to the electromechanical signal, was included in the measurement. The reference tone was injected into the TWPA pump line, so it would not interact with the CNT device, and was intended for monitoring the MW readout gain, enabling corrections of small gain fluctuations during data analysis if necessary. Surprisingly, a significant reduction of the probe tone power is observed in the 0.05–4 K temperature range of the experiment, indicating a loss of gain of almost 4 dB, see [Figure 5.4\(b\)](#).

Simultaneously, the background noise PSD S_{bg} of the experiment rises with tem-

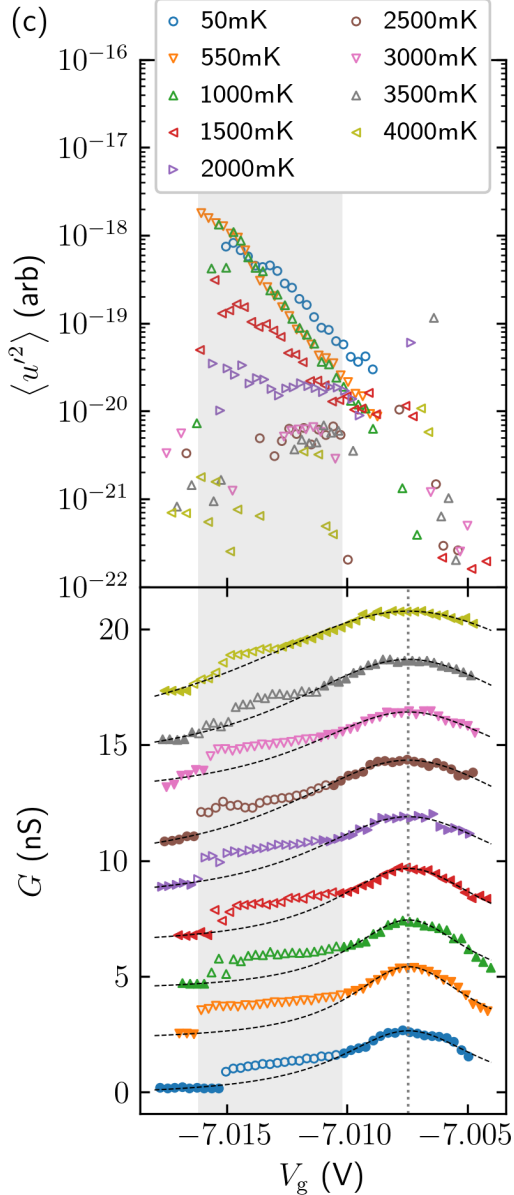
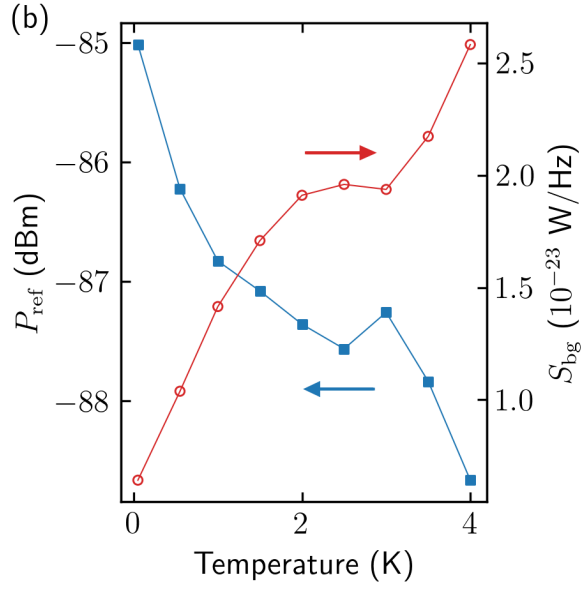
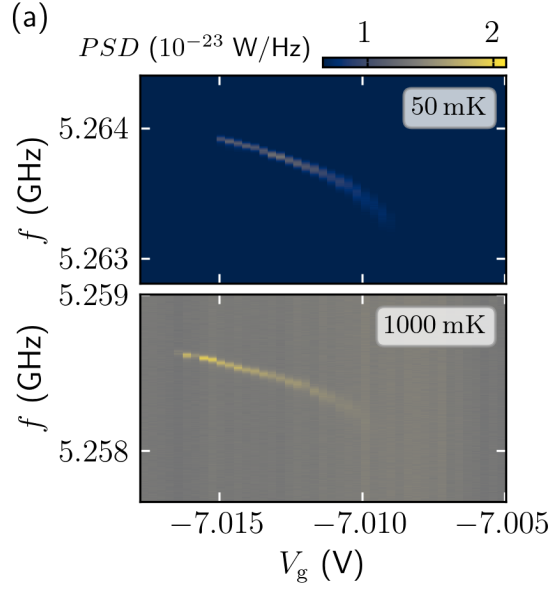


Figure 5.4: (a) Power spectral densities at the mixing sideband at 50 mK and 1 K as function of frequency and gate voltage, but with no RF drive. A peak from electromechanical mixing is still present, indicating non-driven nanotube oscillation. (b) During measurements at different temperatures the MW readout gain was monitored via a weak reference tone injected into the TWPA pump line. Reduction of transmitted power P_{ref} (blue) indicates loss of gain with temperature. Simultaneously, the background noise increases with temperature (red). (c) Bottom: conductance for different temperatures (a systematic offset was subtracted, and consecutive traces are offset by 2 nS for better visibility). Fits to a Lorentzian are overlaid as dashed lines. Shoulders of elevated current on the left flank of conductance peaks were masked out for fitting (empty markers). Top: variance of nanotube displacement for different temperatures extracted from PSD at the electromechanical mixing sideband using Equation (5.10) with results from fitting of conductance peaks and parameters from Table 4.2, see main text for details. Fit results for the centre of conductance peaks were used to subtract a slow drift with respect to V_g .

perature, also shown in Figure 5.4(b). An increase in background noise should be expected due to Johnson-Nyquist noise in the system, the PSD of which is given by

$$S_{\text{JN}}(f) = 4k_{\text{B}}T_{\text{eff}}R\Lambda(f) \quad (5.2)$$

Here, the cryostat temperature has been replaced with an effective temperature T_{eff} , applying the quantum correction of Equation (3.2) since we are operating in a regime where $k_{\text{B}}T \lesssim hf$. $\Lambda(f)$ is an unknown frequency dependent attenuation factor that accounts for losses in the sample carrier. With the observed values of S_{bg} , assuming that background noise is dominated by the 50 k Ω resistor of the sample carrier bias tees leads to a rough approximation of $\Lambda \approx -7$ dB for temperatures below 1 K.

The frequency band for signal transmission between the sample space and TWPA is limited to about 4–12 GHz by a circulator. Under the assumption that $\Lambda(f)$ does not change much in that frequency range and that power limits stated in the TWPA datasheet are accurate¹⁷, the Johnson-Nyquist noise of the bias tee alone is enough to reach the 1 dB compression point of the amplifier at a temperature of about 1 K.

The temperature dependence of gain was spotted early on and compensated for in data analysis, using the measured power level of the reference tone as mentioned above. Unfortunately, the possible connection to Johnson-Nyquist noise and amplifier compression was only noticed after the experiment and most of the data analysis was already completed. Therefore, the analysis presented on the following pages and conclusions drawn from it should be taken with a grain of salt. This issue needs to be carefully investigated before similar experiments are carried out in the future.

An additional concern is that Johnson-Nyquist noise in the system will also exert electrostatic force noise on the nanotube. A rough estimate using parameters of our device yields an electrostatic force noise of $S_{\text{F,JN}} = 4k_{\text{B}}TR(C'_{\text{g}}V_{\text{g}})^2 \approx 10 \text{ zN}/\sqrt{\text{Hz}}$ [12] at 1 K, which is uncomfortably close to the best demonstrated force sensitivity ($12 \text{ zN}/\sqrt{\text{Hz}}$) of similar devices [12]. This can only be reduced by restricting experiments to lower temperatures, or reworking the sample carrier to use smaller resistors.

Possible origin of nanotube oscillations, option 1: Brownian motion

It can be shown that for small displacements each mode of a mechanical resonator is well described as a harmonic oscillator [111]. Considering the tiny mass of a SWCNT, it seems reasonable to use a quantum mechanics approach, where a

¹⁷The TWPA datasheet states 1 dB compression at 15 dB gain for 100 dBm input power.

harmonic oscillator satisfies the time-independent Schrödinger equation

$$\hat{H}\psi = \frac{\hat{p}^2}{2m}\psi + \frac{1}{2}m\omega_m^2\hat{u}^2\psi = E\psi \quad (5.3)$$

with the classical displacement u and momentum p replaced by operators \hat{u} and $\hat{p} = -i\hbar \cdot \partial/\partial u$. It is well known that the eigenenergies of such oscillators are $E_n = \hbar\omega_m(n + \frac{1}{2})$, where n is the phonon occupation of the oscillator. Therefore, even the lowest possible eigenstate ($n = 0$) still has a finite *zero-point energy* $E_0 = \frac{1}{2}\hbar\omega_m$ and *zero-point motion* $u_0 = \sqrt{\hbar/2m\omega_m}$. The latter is typically on the order of a few picometre for a carbon nanotube.

In practice, zero-point motion of the oscillator is usually overwhelmed by thermal noise. The nanotube permanently feels random kicks of stochastic external forces, for example from substrate phonons coupled through the resonator clamping points or fluctuating charges in the nearby environment. This force noise causes resonator displacement known as *Brownian motion*. It is typically assumed that the force noise is white within the bandwidth of the resonator, in which case the power spectral density of displacement S_{uu} takes the shape of a bell curve that is often approximated as a Lorentzian for a high- Q resonator [111]. Moreover, the variance of the displacement can be calculated from the PSD as [111]

$$\langle u^2 \rangle = \int_0^\infty S_{uu}(f) df \quad (5.4)$$

The force noise depends on temperature, which in equilibrium is related to the variance of the displacement by the equipartition theorem [111]

$$\frac{1}{2}k_m \langle u^2 \rangle = \frac{1}{2}k_B T \quad (5.5)$$

With the mechanical spring constant $k_m = m\omega_m^2 = 4\pi^2mf_m^2$, this can be rewritten as

$$4\pi^2f_m^2m \langle u^2 \rangle = k_B T \quad (5.6)$$

This expression is incredibly useful, since all quantities except the resonator mass m (including $\langle u^2 \rangle$, as we will see in a moment) are directly accessible in experiments. Therefore, when Brownian motion of a resonator can be detected, it allows calibration of the resonator mass, which otherwise has to be estimated from typical CNT properties, leading to large errors.

Since in a CNT NEMS device nanotube deflection is transduced into a current signal (we used this in our detection methods for mechanical resonance), the variance of displacement can be obtained by measuring the power spectral density of electromechanical current fluctuations S_{II} from the CNT device and applying an

appropriate rescaling factor:

$$\langle u^2 \rangle = \int_0^\infty S_{uu}(f) df = \frac{1}{\beta^2} \int_0^\infty S_{II}(f) df \quad (5.7)$$

From Equation (5.1) we can deduce that the scaling factor is

$$\beta = \frac{1}{2} \frac{dG}{dV_g} V_g V_{sd}^{ac} \frac{C'_g}{C_g} \quad (5.8)$$

(For a more thorough derivation of the results summarised in the above paragraph see Supplementary information of [12].)

We now have all the necessary tools for a preliminary evaluation of datasets like the ones in Figure 5.4(a). We extract S_{II} by fitting the measured PSD S_{tot} for each V_g to the equation

$$S_{tot} = [S_{II} + S_{bg}] \cdot G_{MW} \quad (5.9)$$

where the PSD of electromechanical current fluctuations S_{II} takes the form of a Lorentzian and S_{bg} summarises amplifier noise in the MW readout electronics and Johnson-Nyquist noise of the bias tee resistor (see above). Since the background noise within the window of the experiment is reasonably flat, we approximate it as $S_{bg} = af + b$ without particular consideration of the origin of the background. The gain G_{MW} is known from characterisation of the MW readout electronics in Chapters 2 and 3. It is rescaled for each temperature setpoint to account for temperature dependent changes observed in the previously mentioned reference tone power (Figure 5.4(b)).

To obtain values for β , we use the results for C_g and C'_g from the previous chapter, see Table 4.2. V_g is a parameter set in the experiment. The transconductance dG/dV_g can in principle be calculated from the dc current measured simultaneously with the PSD of the electromechanical signal (Figure 5.4(c), bottom), however, the measurement was too noisy to get usable results directly from numerical differentiation. Instead, the measured conductance peaks are fitted to a Lorentzian and dG/dV_g is calculated by inserting the fit parameters and gate voltages into the derivative of a Lorentzian. Note that all conductance peaks have a shoulder of higher-than-expected conductance on the left flank which prevents a good fit to a Lorentzian. When the shoulders are masked out for fitting (empty markers in bottom of Figure 5.4(c)), fits to the remaining data produce nice results (dashed lines overlaid in Figure 5.4(c)), but results from areas removed for fitting (shaded areas in Figure 5.4(c)) should be viewed with scepticism. The fit results for centres of the conductance peaks are used to subtract small drifts with respect to V_g between datasets at different temperatures. With this, since we do not know the losses in-

volved in supplying the MW probe tone to the source electrode, $V_{\text{sd}}^{\text{ac}}$ is the only unknown remaining, but since it is constant throughout the experiment we treat it as an arbitrary rescaling factor. Putting everything together, we get a rescaled result for the variance of CNT displacement:

$$\langle u'^2 \rangle = (V_{\text{sd}}^{\text{ac}})^2 \langle u^2 \rangle = \frac{1}{\beta'} \int_0^\infty S_{II}(f) df \quad (5.10)$$

with

$$\beta' = \frac{\beta}{V_{\text{sd}}^{\text{ac}}} = \frac{1}{2} \frac{dG}{dV_g} V_g \frac{C'_g}{C_g} \quad (5.11)$$

Results for $\langle u'^2 \rangle$ are plotted in the top panel of [Figure 5.4\(c\)](#). Outside the area of elevated conductance (shaded area), few PSD traces produced nice Lorentzian fits for the electromechanical peak. Therefore, data points are sparse and no clear trend for a temperature dependence can be identified. Within the region of elevated conductance we find more usable data points. However, the overall trend seems to be a decrease of $\langle u'^2 \rangle$ with temperature, the opposite of what we expect according to [Equation \(5.6\)](#).

J. Moser *et al.* [12] find in their measurements of Brownian motion of a CNT, that an excessive amplitude of $V_{\text{sd}}^{\text{ac}}$ can lead to overestimation of $\langle u^2 \rangle$ due to artificial (Joule) heating of the mechanical oscillator. S. L. de Bonis *et al.* [116] find that at higher cryostat temperature a wider range of probe tone amplitudes can be applied before artificial heating becomes a problem. Given that the probe tone power arriving at the device in our experiment is potentially significantly higher than the equivalent limits of V_{sd} found in these two references, this could explain the discrepancy in our temperature dependence of $\langle u'^2 \rangle$.

More data is required for estimating the amplitude of $V_{\text{sd}}^{\text{ac}}$ in our setup and finding appropriate limits to exclude any impact of the probe tone on the outcome of the experiment.

Possible origin of nanotube oscillations, option 2: Self-driven oscillation

It is known that suspended CNTs can sustain self-driven (also referred to as current-driven) oscillations. Evidence of this has been observed in experiments [117–120] and theoretical descriptions have been developed [119, 121]. Conditions for observing self-oscillations include low temperatures, a high mechanical quality factor, strong coupling between the mechanical resonator and single electron tunnelling and energy-dependent tunnel barriers between the nanotube quantum dot and the leads.

Interestingly, experimental observations and a corresponding theoretical model for self-driven oscillations based on energy dependent electron tunnelling presented

by K. Willick and J. Baugh [119] is a good qualitative match to the data from our experiment. They observe areas of finite conductance in low-bias transport that should normally be Coulomb blockaded. In I - V_g -traces these look very similar to the shoulders of elevated conductance we observe in our experiment (cf. Figure 5.4(c)). Additionally, they see strong evidence of self-oscillation at low temperature (30 mK) and a weaker effect at higher temperature to the point where they barely detect any evidence of self-oscillation at 1.4 K. Thus, the trend of reduced $\langle u'^2 \rangle$ with increased temperature we observe also seems to match the behaviour of self-oscillations.

Despite this apparent qualitative match between these two experiments, we shall not jump to conclusions here. To unequivocally identify our signal as self-oscillation of the CNT resonator, additional data is required. New data should be acquired in time domain rather than PSD. If coherence is found in a time series of the electromechanical signal, self-oscillations will be confirmed as source of our non-driven oscillations.

BLANK PAGE

Chapter 6

Conclusion and Outlook

In this thesis initial work on steps towards a CNT NEMS magnet-on-cantilever type MRFM detector was presented, addressing several aspects of the experiment.

At the start of the project, two nearly identical commercially available dilution refrigerators were installed in our lab. Both of these cryostats were equipped with custom wiring as described in [Chapter 2](#). As such, they are now suitable experimental platforms for low noise measurements at millikelvin temperatures involving dc and low-frequency (up to few kHz, convenient for lock-in amplifiers) signals, as well as high frequency signals in the RF and MW range. This allows not only performing the experiments on quantum transport and nanomechanics presented in this work, but also enables studying of quantum devices like Josephson junctions, SQUIDs, qubits and parametric amplifiers. Current projects hosted in our cryostats, besides the work presented here, include parametric amplification and impedance tunable circuits using quantum paraelectricity (carried out by D. Das), as well as probing the properties of superfluid helium with an immersed CNT mechanical resonator (carried out by S. Henderson, previously S. Khan [[122](#)]). The installed wiring and components, particularly the high frequency sections, were characterised in order to provide calibration data for cryostat characteristics which may help with data analysis of ongoing and future experiments.

Our MW readout electronics include a Josephson TWPA, a relatively new amplifier technology for low-noise signal readout in the GHz range (initially, these amplifiers were primarily developed for efficient qubit readout), which is just beginning to become commercially available. Our TWPA is designed for a signal frequency range of 4–9 GHz and was an early sample sent to us by our collaborators at VTT. Therefore, it was given particular attention during performance characterisation of our cryostat and the results were presented in [Chapter 3](#). The operating point of the amplifier, which is set by a pump tone at about twice the signal frequency and a dc current for providing a magnetic flux bias, was tuned for optimal broadband gain

in our system, leading to additional gain of about 10–15 dB and SNR improvement of approximately 9 dB for our MW readout electronics. The amplifier was installed inside two layers of shielding against magnetic fields, an outer layer of mu-metal followed by an inner layer of Al tubing. It was confirmed that amplifier gain is not affected by magnetic fields from a 3-axis superconducting vector magnet installed in the cryostat for up to about 2 T in the sample space.

Noise performance of the TWPA was studied in a Y-factor measurement using a Lancaster built cryogenic noise source. It was found that noise from the TWPA is less than a factor of two above the standard quantum limit for almost its entire bandwidth, with only a few spikes at specific frequencies, presumably from unwanted non-linear processes in the amplifier. The experiment also confirmed that the total noise of the MW readout is now dominated by the TWPA noise, reducing the total system noise temperature by about a factor of 5 compared to a setup where the primary gain stage is a HEMT amplifier at 4 K.

Subsequently, the focus in [Chapter 4](#) was shifted towards a detector for MRFM. Since NEMS formed by suspended CNTs are known to be excellent force detectors [12], a new detector design based on that device geometry was proposed. The major challenge identified for fabrication of such a device is deposition of a magnetic particle (or sample, depending on the geometry of a future MRFM implementation) onto a doubly clamped cantilever formed by an individual CNT, which requires essentially nanometre precision, without degrading device quality through fabrication induced defects or contamination. In the proposed device design, this issue is addressed by a narrow trench through the substrate underneath the nanotube, which opens up into a “funnel” on the back. This should allow elimination of any needs for alignment of a deposition process onto the nanotube. Instead, the device substrate itself acts as a shadow mask when material is deposited onto the nanotube through the trench from the back of the chip.

A 16 layer fabrication process for the proposed device design was laid out, that aims for ultraclean nanotube devices by placing a CNT on the device via stamp transfer in the second to last step. The last step is then deposition of a magnetic particle on the nanotube through the substrate shadow mask. The fabrication process was successfully implemented to the point of nanotube transfer. It was then decided to characterise a device at cryogenic temperatures before attempting deposition of the magnet, so that later on device parameters before and after deposition could be directly compared. Unfortunately, since the investigated device is still in the cryostat at the time of writing this thesis, this means that the final, and arguably most crucial for the intended application, fabrication step of magnet deposition through a shadow mask substrate has not yet been attempted.

A device fabricated following the above process was characterised at millikelvin temperatures in one of the previously customised dilution refrigerators. Quantum dot spectroscopy revealed properties of a large bandgap semiconducting nanotube and formation of a rather opaque quantum dot that does not conduct in electron conduction and exhibits Coulomb blockade on the hole conduction side. Some irregularity and a gap in conductance near zero bias was observed in the Coulomb blockade stability diagram, likely indicating the formation of a series of quantum dots rather than just a single dot, presumably due to disorder near the interface to the leads. The characteristic fourfold shell filling of CNT quantum dots was not observed, suggesting that energy contributions from the single particle spectrum are small in this device.

Mechanical resonances of the device were characterised in the rectification technique and 16 mechanical modes with frequencies between approximately 65–800 MHz and quality factors up to 203 300 were found. Several modes only appear for very high drive powers and are therefore suspected to be parametric excitations of other modes. A mode at 256 MHz was identified as fundamental resonance, as it is the lowest mode with a bright response at lower drive powers. All resonances seem to appear as “twin” modes with another resonance close by. In literature, this behaviour is generally attributed to one mode shape oscillating in orthogonal directions [12, 48]. Frequency tunability of mechanical modes for gate voltages $-10\text{ V} < V_g < -3\text{ V}$ ranges from a few MHz up to about 30 MHz for some of the higher modes. The characteristic spring softening from interaction with single electron tunnelling through the quantum dot is observed.

In the final [Chapter 5](#) a new detection scheme for CNT mechanical resonances was presented. Electromechanical mixing with a MW probe tone is used to upconvert mechanical resonance frequencies into the GHz range and the signal is detected with our TWPA as primary amplifier. Overall, this approach produced promising first results. Mechanical resonances clearly show up in the data and, although not properly quantified yet, measurement sensitivity seems to outperform at least the rectification technique significantly.

Unfortunately, the experiment in its current form comes with some inconveniences. Leakage of input tones into the readout electronics, if left unaddressed, leads to a complete failure of the experiment. Suppression of leaked signals via destructive interference as presented in this thesis does work, but is inconvenient and time consuming. Particularly, sweeps of the drive frequency have to be slowed down significantly, since every change of f_{RF} requires retuning of the cancellation tone. Additionally, this approach only works for low and intermediate input powers, since at high power levels the finite tuning accuracy of the cancel tones eventually leads

to insufficient cancellation and significant mixing in the TWPA. This is made worse by the fact that tuning accuracy of the cancel branches (especially the MW cancel) is affected by room temperature fluctuations due to a temperature dependent phase shift of the amplifiers and phase shifters. At higher powers a temperature change of about 1 °C (less than the temperature swing of air conditioning in our lab!) can already disrupt the experiment.

For future experiments, efforts should be made to reduce the importance of cancelling of leaked input tones, or even replace it with other solutions entirely. One big advantage of the mixing technique is that the signal of interest is separated from the drive and probe tone in frequency space. Options that could be explored as additions to the experimental setup inside the cryostat are highpass or bandstop filters (on-chip or as cryogenic circuit components) or a tank circuit or resonant cavity between the device and amplifier, so that only the electromechanical mixing signal is transmitted to the MW readout and other frequency components are rejected. Additionally, the device design should be reworked with the aim of reducing parasitic signal paths, which in the first instance should be achievable by just shortening the electrodes [115].

It was found that the mixing technique with TWPA readout is sensitive enough to detect non-driven nanotube oscillations, at least within a narrow parameter space for the device investigated. Initially it was thought that this might be Brownian motion, which would be useful for calibrating the resonator mass and determining the force sensitivity of our device. However, an investigation of these oscillations as a function of temperature showed reduced oscillations at higher temperatures, the opposite of what is expected from Brownian motion. It is possible that in our experiment the oscillator was artificially heated from using a MW probe tone with excessive power, which could explain this reversed temperature dependence [12, 116], however, qualitative comparison to literature seems to indicate that our observations are a reasonably good match for indications of current-driven oscillations of the nanotube [119].

From the temperature sweep for the above Brownian motion investigation a potential flaw of the experimental setup was identified. In the corresponding dataset a very much unexpected reduction of gain at increased temperature was noticed. A rough estimation suggests that high-valued resistors used on the sample carrier PCB could potentially produce enough Johnson-Nyquist noise to cause gain compression in the TWPA. Additionally, electrostatic force noise on a CNT resulting from Johnson-Nyquist noise in the current setup might approach the force sensitivity of good CNT force sensors already around 1 K. This needs to be investigated before attempting more noise measurements or temperature dependent experiments

to make sure that the amplifier performs as expected and system noise does not excessively impact experimental results. Depending on the outcome, reworking of the sample carrier with smaller resistors may be necessary.

A few options for next steps in the experiment are available. First, since the signal from nanotube motion in the electromechanical mixing approach not only contains information about the motion amplitude (like the rectification technique), but also the frequency spectrum of the resonator response, this could be used for further investigation of apparent resonances that are suspected to be parametric excitations. Parametric excitation could for example be directly confirmed by detecting nanotube motion at half the drive frequency. This is currently being worked on by S. Dicker, and initial results seem promising. Future implementation of above mentioned setup improvements for making cancellation of leaked input tones redundant may allow higher drive powers, potentially making investigation of parametric excitation or other non-linear effects more accessible.

Naturally, the next step once ongoing low-temperature experiments on the current device conclude, is to finally attempt the last step of the fabrication process, deposition of a magnetic particle through the device substrate shadow mask. The verdict on feasibility of the proposed device design entirely depends on the success or failure of this step. Successful magnet deposition could enable a number of experiments that so far were inaccessible to ultraclean CNT resonators, including torsion of a nanotube in a rotating magnetic field and investigation of impacts on the mechanical quality factor (e.g., how much do we need to worry about eddy current damping?).

Repeating the experiments in this thesis with a second device should also be a worthwhile effort. A device with a more transparent quantum dot could easily have orders of magnitude higher transconductance, which should also significantly increase the sensitivity for detection of nanotube motion and external forces. Of course, the force sensitivity in our experiment needs to be properly quantified as soon as possible in order to see how our efforts rank compared to other approaches for improvements in the realm of MRFM.

Finally, returning to the initial motivation for this work, once the type of CNT device proposed in this thesis has been sufficiently characterised, integration as a detector in MRFM can be attempted. A first milestone for establishing our device as MRFM detector could be demonstrating the capability of mechanically detected spin resonance spectroscopy without any attempt of imaging. For this, four main challenges need to be addressed. The first is selection of a suitable sample. One could start with a material suitable for observing electron spin resonance (e.g., the stable organic radical diphenyl picrahydrazyl (DPPH) [10]), since interactions with

electron spins are typically stronger than with nuclear spins, leading to stronger spin resonance signals. Samples for NMR could be the ^1H spins in polymers like polystyrene [11]. The second challenge is the relative positioning of sample and detector. For a pure spectroscopy experiment this can likely be done at room temperature before loading the components into the cryostat, eliminating the challenge of alignment without visual feedback inside the cryostat and reducing the problem to designing a suitable mounting system that can hold both the sample and detector at a predetermined small enough distance from each other. The third challenge is delivering a RF or MW signal to the sample that drives resonant spin flips. This can be achieved via a nearby coil or a strip line on a sample carrying substrate and mostly depends on the geometry of the experiment, especially available space in the vicinity of the sample and possible ways of connecting to the cryostat wiring. Finally, a spin resonance spectroscopy measurement protocol needs to be implemented. Literature on NMR and MRFM already offers a plethora of approaches, ranging from simple continuous measurements to various pulse sequences for spin manipulation. The challenge here is selecting and implementing a suitable protocol.

For upgrading from spin resonance spectroscopy to MRFM, two more issues will need to be addressed. First, the detector needs to move relative to the sample. This is primarily an engineering problem that requires solutions for relative positioning of sample and detector with high accuracy, low noise and minimal drift, all in the absence of visual feedback. Additionally, the actuators used for scanning the detector across the sample cannot impose an excessive thermal load on the cryostat. Second, the interaction between a sample and MRFM detector occurs not at a single point, but within a *resonant slice* of constant magnetic field whose shape is determined by the field gradient created by the magnetic particle on our detector. Consequently, any image acquired in MRFM is convolved with a point spread function defined by the shape of this resonant slice. Accurately determining the shape of the resonant slice is essential, as it is the basis for image reconstruction algorithms that recover the true image from raw MRFM data [4, 6, 7]. Both of these challenges already had to be addressed in earlier MRFM experiments, the former also in many adjacent fields (i.e., any cryogenic scanning probe experiment), and much progress has already been made. Drawing insight from existing literature, as well as engaging in correspondence and collaboration with experts in MRFM and other cryogenic scanning probe techniques, will be vital for successful implementation of MRFM using the new CNT-based detector proposed in this work.

Bibliography

- [1] L. Ciobanu, D. A. Seeber and C. H. Pennington. ‘3D MR microscopy with resolution 3.7 microm by 3.3 microm by 3.3 microm’. In: *J. Magn. Reson.* 158.1-2 (2002), pp. 178–182. DOI: [10.1016/S1090-7807\(02\)00071-X](https://doi.org/10.1016/S1090-7807(02)00071-X).
- [2] J. A. Sidles. ‘Noninductive detection of single-proton magnetic resonance’. In: *Applied Physics Letters* 58.24 (1991), pp. 2854–2856. DOI: [10.1063/1.104757](https://doi.org/10.1063/1.104757).
- [3] D. Rugar et al. ‘Single spin detection by magnetic resonance force microscopy’. In: *Nature* 430.6997 (2004), pp. 329–332. DOI: [10.1038/nature02658](https://doi.org/10.1038/nature02658).
- [4] C. L. Degen et al. ‘Nanoscale magnetic resonance imaging’. In: *Proceedings of the National Academy of Sciences of the United States of America* 106.5 (2009), pp. 1313–1317. DOI: [10.1073/pnas.0812068106](https://doi.org/10.1073/pnas.0812068106).
- [5] U. Grob et al. ‘Magnetic Resonance Force Microscopy with a One-Dimensional Resolution of 0.9 Nanometers’. In: *Nano letters* 19.11 (2019), pp. 7935–7940. DOI: [10.1021/acs.nanolett.9b03048](https://doi.org/10.1021/acs.nanolett.9b03048).
- [6] S. Chao et al. ‘Nanometer-scale magnetic resonance imaging’. In: *Review of Scientific Instruments* 75.5 (2004), pp. 1175–1181. DOI: [10.1063/1.1666983](https://doi.org/10.1063/1.1666983).
- [7] J. M. Nichol et al. ‘Nanoscale Fourier-Transform Magnetic Resonance Imaging’. In: *Physical Review X* 3.3 (2013). DOI: [10.1103/PhysRevX.3.031016](https://doi.org/10.1103/PhysRevX.3.031016).
- [8] M. Toda and T. Ono. ‘Three-dimensional imaging of electron spin resonance-magnetic resonance force microscopy at room temperature’. In: *Journal of magnetic resonance (San Diego, Calif. : 1997)* 330 (2021), p. 107045. DOI: [10.1016/j.jmr.2021.107045](https://doi.org/10.1016/j.jmr.2021.107045).
- [9] R. Fischer et al. ‘Spin detection with a micromechanical trampoline: towards magnetic resonance microscopy harnessing cavity optomechanics’. In: *New Journal of Physics* 21.4 (2019), p. 043049. DOI: [10.1088/1367-2630/ab117a](https://doi.org/10.1088/1367-2630/ab117a).
- [10] N. Scozzaro et al. ‘Magnetic resonance force detection using a membrane resonator’. In: *Journal of magnetic resonance (San Diego, Calif. : 1997)* 271 (2016), pp. 15–20. DOI: [10.1016/j.jmr.2016.07.012](https://doi.org/10.1016/j.jmr.2016.07.012).

- [11] J. M. Nichol et al. ‘Nanomechanical detection of nuclear magnetic resonance using a silicon nanowire oscillator’. In: *Physical Review B* 85.5 (2012). DOI: [10.1103/PhysRevB.85.054414](https://doi.org/10.1103/PhysRevB.85.054414).
- [12] J. Moser et al. ‘Ultrasensitive force detection with a nanotube mechanical resonator’. In: *Nature nanotechnology* 8.7 (2013), pp. 493–496. DOI: [10.1038/NNANO.2013.97](https://doi.org/10.1038/NNANO.2013.97).
- [13] J. Moser et al. ‘Nanotube mechanical resonators with quality factors of up to 5 million’. In: *Nature nanotechnology* 9.12 (2014), pp. 1007–1011. DOI: [10.1038/NNANO.2014.234](https://doi.org/10.1038/NNANO.2014.234).
- [14] J. D. Teufel et al. ‘Nanomechanical motion measured with an imprecision below that at the standard quantum limit’. In: *Nature nanotechnology* 4.12 (2009), pp. 820–823. DOI: [10.1038/nnano.2009.343](https://doi.org/10.1038/nnano.2009.343).
- [15] O. Yaakobi et al. ‘Parametric amplification in Josephson junction embedded transmission lines’. In: *Physical Review B* 87.14 (2013). DOI: [10.1103/PhysRevB.87.144301](https://doi.org/10.1103/PhysRevB.87.144301).
- [16] C. Macklin et al. ‘A near-quantum-limited Josephson traveling-wave parametric amplifier’. In: *Science (New York, N.Y.)* 350.6258 (2015), pp. 307–310. DOI: [10.1126/science.aaa8525](https://doi.org/10.1126/science.aaa8525).
- [17] W. R. Hudson and R. J. Jirberg. *Superconducting Properties of Niobium Films: NASA technical note D-6380*. 1971.
- [18] H. London and G. R. Clarke. ‘Superconductivity of Thin Films of Niobium’. In: *Reviews of Modern Physics* 36.1 (1964), pp. 320–323. DOI: [10.1103/RevModPhys.36.320](https://doi.org/10.1103/RevModPhys.36.320).
- [19] P. Das, R. B. de Ouboter and K. W. Taconis. ‘A Realization of a London-Clarke-Mendoza Type Refrigerator’. In: *Low Temperature Physics LT9*. Ed. by J. G. Daunt et al. Boston, MA: Springer US, Imprint and Springer, 1965, pp. 1253–1255. DOI:

-
- [24] N. E. Frattini et al. ‘3-wave mixing Josephson dipole element’. In: *Applied Physics Letters* 110.22 (2017). DOI: [10.1063/1.4984142](https://doi.org/10.1063/1.4984142).
- [25] V. Vesterinen. *Josephson traveling wave parametric amplifiers for GHz frequencies: Datasheet for VTT TWPA*. 2020.
- [26] D. M. Pozar. *Microwave engineering*. Fourth Edition. Hoboken, NJ: John Wiley & Sons Inc, 2012.
- [27] S. Simbierowicz et al. ‘Characterizing cryogenic amplifiers with a matched temperature-variable noise source’. In: *Review of Scientific Instruments* 92.3 (2021), p. 034708. DOI: [10.1063/5.0028951](https://doi.org/10.1063/5.0028951).
- [28] J. M. A. Chawner et al. ‘LEGO® Block Structures as a Sub-Kelvin Thermal Insulator’. In: *Scientific reports* 9.1 (2019), p. 19642. DOI: [10.1038/s41598-019-55616-7](https://doi.org/10.1038/s41598-019-55616-7).
- [29] E. H. L. Falcao and F. Wudl. ‘Carbon allotropes: beyond graphite and diamond’. In: *Journal of Chemical Technology & Biotechnology* 82.6 (2007), pp. 524–531. DOI: [10.1002/jctb.1693](https://doi.org/10.1002/jctb.1693).
- [30] M. Monthieux and V. L. Kuznetsov. ‘Who should be given the credit for the discovery of carbon nanotubes?’ In: *Carbon* 44.9 (2006), pp. 1621–1623. DOI: [10.1016/j.carbon.2006.03.019](https://doi.org/10.1016/j.carbon.2006.03.019).
- [31] S. Iijima and T. Ichihashi. ‘Single-shell carbon nanotubes of 1-nm diameter’. In: *Nature* 363.6430 (1993), pp. 603–605. DOI: [10.1038/363603a0](https://doi.org/10.1038/363603a0).
- [32] D. S. Bethune et al. ‘Cobalt-catalysed growth of carbon nanotubes with single-atomic-layer walls’. In: *Nature* 363.6430 (1993), pp. 605–607. DOI: [10.1038/363605a0](https://doi.org/10.1038/363605a0).
- [33] Z. Ali et al. ‘Critical review on the characterization, preparation, and enhanced mechanical, thermal, and electrical properties of carbon nanotubes and their hybrid filler polymer composites for various applications’. In: *Composites Part C: Open Access* 13 (2024), p. 100434. DOI: [10.1016/j.jcomc.2024.100434](https://doi.org/10.1016/j.jcomc.2024.100434).
- [34] S. R. Bakshi, D. Lahiri and A. Agarwal. ‘Carbon nanotube reinforced metal matrix composites - a review’. In: *International Materials Reviews* 55.1 (2010), pp. 41–64. DOI: [10.1179/095066009X12572530170543](https://doi.org/10.1179/095066009X12572530170543).
- [35] S. K. Soni, B. Thomas and V. R. Kar. ‘A Comprehensive Review on CNTs and CNT-Reinforced Composites: Syntheses, Characteristics and Applications’. In: *Materials Today Communications* 25 (2020), p. 101546. DOI: [10.1016/j.mtcomm.2020.101546](https://doi.org/10.1016/j.mtcomm.2020.101546).

- [36] A. M. Schrand and T. B. Tolle. ‘Carbon nanotube and epoxy composites for military applications’. In: *Carbon nanotechnology*. Amsterdam [etc.]: Elsevier, 2006, pp. 633–675. DOI: [10.1016/B978-044451855-2/50021-8](https://doi.org/10.1016/B978-044451855-2/50021-8).
- [37] K. A. Watson and J. W. Connell. ‘Polymer and carbon nanotube composites for space applications’. In: *Carbon nanotechnology*. Amsterdam [etc.]: Elsevier, 2006, pp. 677–698. DOI: [10.1016/B978-044451855-2/50022-X](https://doi.org/10.1016/B978-044451855-2/50022-X).
- [38] E. G. Rakov. ‘Materials made of carbon nanotubes. The carbon nanotube forest’. In: *Russ. Chem. Rev.* 82.6 (2013), pp. 538–566. DOI: [10.1070/RC2013v082n06ABEH004340](https://doi.org/10.1070/RC2013v082n06ABEH004340).
- [39] S. Darwin et al. ‘Performance Analysis of Carbon Nanotube Transistors - A Review’. In: *6th International Conference on Trends in Electronics and Informatics (ICOEI 2022)*. Piscataway, NJ: IEEE, 2022, pp. 25–31. DOI: [10.1109/ICOEI53556.2022.9776858](https://doi.org/10.1109/ICOEI53556.2022.9776858).
- [40] A. D. Franklin, M. C. Hersam and H. S. P. Wong. ‘Carbon nanotube transistors: Making electronics from molecules’. In: *Science (New York, N.Y.)* 378.6621 (2022), pp. 726–732. DOI: [10.1126/science.abp8278](https://doi.org/10.1126/science.abp8278).
- [41] P. Prakash, K. Mohana Sundaram and M. Anto Bennet. ‘A review on carbon nanotube field effect transistors (CNTFETs) for ultra-low power applications’. In: *Renewable and Sustainable Energy Reviews* 89 (2018), pp. 194–203. DOI: [10.1016/j.rser.2018.03.021](https://doi.org/10.1016/j.rser.2018.03.021).
- [42] J. Si, P. Zhang and Z. Zhang. ‘Road map for, and technical challenges of, carbon-nanotube integrated circuit technology’. In: *National science review* 11.3 (2024), nwad261. DOI: [10.1093/nsr/nwad261](https://doi.org/10.1093/nsr/nwad261).
- [43] A. K. Hüttel et al. ‘Carbon Nanotubes as Ultrahigh Quality Factor Mechanical Resonators’. In: *Nano letters* 9.7 (2009), pp. 2547–2552. DOI: [10.1021/nl900612h](https://doi.org/10.1021/nl900612h).
- [44] Edward A. Laird et al. ‘A high quality factor carbon nanotube mechanical resonator at 39 GHz’. In: *Nano letters* 12.1 (2012), pp. 193–197. DOI: [10.1021/nl203279v](https://doi.org/10.1021/nl203279v).
- [45] H. B. Meerwaldt et al. ‘Carbon nanotubes: Nonlinear high-Q resonators with strong coupling to single-electron tunneling // Carbon nanotubes: Nonlinear high-Q resonators with strong coupling to single-electron tunneling’. In: *Fluctuating Nonlinear Oscillators*. Ed. by Mark Dykman. Oxford: Oxford University Press Incorporated, 2012.
- [46] N. Ares et al. ‘Resonant Optomechanics with a Vibrating Carbon Nanotube and a Radio-Frequency Cavity’. In: *Physical review letters* 117.17 (2016), p. 170801. DOI: [10.1103/PhysRevLett.117.170801](https://doi.org/10.1103/PhysRevLett.117.170801).

- [47] S. Blien et al. ‘Quantum capacitance mediated carbon nanotube optomechanics’. In: *Nature communications* 11.1 (2020), p. 1636. DOI: [10.1038/s41467-020-15433-3](https://doi.org/10.1038/s41467-020-15433-3).
- [48] N. Hüttner et al. ‘Optomechanical Coupling and Damping of a Carbon Nanotube Quantum Dot’. In: *Physical Review Applied* 20.6 (2023). DOI: [10.1103/PhysRevApplied.20.064019](https://doi.org/10.1103/PhysRevApplied.20.064019).
- [49] A. Tavernarakis et al. ‘Optomechanics with a hybrid carbon nanotube resonator’. In: *Nature communications* 9.1 (2018), p. 662. DOI: [10.1038/s41467-018-03097-z](https://doi.org/10.1038/s41467-018-03097-z).
- [50] T. Han et al. ‘Carbon nanotubes and its gas-sensing applications: A review’. In: *Sensors and Actuators A: Physical* 291 (2019), pp. 107–143. DOI: [10.1016/j.sna.2019.03.053](https://doi.org/10.1016/j.sna.2019.03.053).
- [51] V. Schroeder et al. ‘Carbon Nanotube Chemical Sensors’. In: *Chemical reviews* 119.1 (2019), pp. 599–663. DOI: [10.1021/acs.chemrev.8b00340](https://doi.org/10.1021/acs.chemrev.8b00340).
- [52] I. Khivrich and S. Ilani. ‘Atomic-like charge qubit in a carbon nanotube enabling electric and magnetic field nano-sensing’. In: *Nature communications* 11.1 (2020), p. 2299. DOI: [10.1038/s41467-020-16001-5](https://doi.org/10.1038/s41467-020-16001-5).
- [53] D. M. Armada, J. E. Proctor and A. Vijayaraghavan. *An Introduction to Graphene and Carbon Nanotubes*. CRC Press, 2020.
- [54] V. B. Mbayachi et al. ‘Graphene synthesis, characterization and its applications: A review’. In: *Results in Chemistry* 3 (2021), p. 100163. DOI: [10.1016/j.rechem.2021.100163](https://doi.org/10.1016/j.rechem.2021.100163).
- [55] E. A. Laird et al. ‘Quantum transport in carbon nanotubes’. In: *Reviews of Modern Physics* 87.3 (2015), pp. 703–764. DOI: [10.1103/RevModPhys.87.703](https://doi.org/10.1103/RevModPhys.87.703).
- [56] P. R. Wallace. ‘The Band Theory of Graphite’. In: *Physical Review* 71.9 (1947), pp. 622–634. DOI: [10.1103/PhysRev.71.622](https://doi.org/10.1103/PhysRev.71.622).
- [57] R. Saito, G. Dresselhaus and M. S. Dresselhaus. *Physical properties of carbon nanotubes*. 1st ed., repr. London: Imperial College Press, 1998 (imp. 2007).
- [58] R. Saito, G. Dresselhaus and M. S. Dresselhaus. ‘Trigonal warping effect of carbon nanotubes’. In: *Physical Review B* 61.4 (2000), pp. 2981–2990. DOI: [10.1103/PhysRevB.61.2981](https://doi.org/10.1103/PhysRevB.61.2981).
- [59] A. H. Castro Neto et al. ‘The electronic properties of graphene’. In: *Reviews of Modern Physics* 81.1 (2009), pp. 109–162. DOI: [10.1103/RevModPhys.81.109](https://doi.org/10.1103/RevModPhys.81.109).

- [60] K. S. Novoselov et al. ‘Electric field effect in atomically thin carbon films’. In: *Science (New York, N.Y.)* 306.5696 (2004), pp. 666–669. DOI: [10.1126/science.1102896](https://doi.org/10.1126/science.1102896).
- [61] I. Pletikosić et al. ‘Dirac cones and minigaps for graphene on Ir(111)’. In: *Physical Review Letters* 102.5 (2009), p. 056808. DOI: [10.1103/PhysRevLett.102.056808](https://doi.org/10.1103/PhysRevLett.102.056808).
- [62] K. S. Novoselov et al. ‘Two-dimensional gas of massless Dirac fermions in graphene’. In: *Nature* 438.7065 (2005), pp. 197–200. DOI: [10.1038/nature04233](https://doi.org/10.1038/nature04233).
- [63] R. Saito et al. ‘Electronic structure of chiral graphene tubules’. In: *Applied Physics Letters* 60.18 (1992), pp. 2204–2206. DOI: [10.1063/1.107080](https://doi.org/10.1063/1.107080).
- [64] N. Hamada, Si Sawada and A. Oshiyama. ‘New one-dimensional conductors: Graphitic microtubules’. In: *Physical review letters* 68.10 (1992), pp. 1579–1581. DOI: [10.1103/PhysRevLett.68.1579](https://doi.org/10.1103/PhysRevLett.68.1579).
- [65] X. Zhou et al. ‘Band structure, phonon scattering, and the performance limit of single-walled carbon nanotube transistors’. In: *Physical review letters* 95.14 (2005), p. 146805. DOI: [10.1103/PhysRevLett.95.146805](https://doi.org/10.1103/PhysRevLett.95.146805).
- [66] G. S. Painter and D. E. Ellis. ‘Electronic Band Structure and Optical Properties of Graphite from a Variational Approach’. In: *Physical Review B* 1.12 (1970), pp. 4747–4752. DOI: [10.1103/PhysRevB.1.4747](https://doi.org/10.1103/PhysRevB.1.4747).
- [67] R. C. Tatar and S. Rabii. ‘Electronic properties of graphite: A unified theoretical study’. In: *Physical Review B* 25.6 (1982), pp. 4126–4141. DOI: [10.1103/PhysRevB.25.4126](https://doi.org/10.1103/PhysRevB.25.4126).
- [68] S. B. Trickey et al. ‘Interplanar binding and lattice relaxation in a graphite dilayer’. In: *Physical review. B, Condensed matter* 45.8 (1992), pp. 4460–4468. DOI: [10.1103/physrevb.45.4460](https://doi.org/10.1103/physrevb.45.4460).
- [69] J. W. Mintmire, B. I. Dunlap and C. T. White. ‘Are fullerene tubules metallic?’ In: *Physical review letters* 68.5 (1992), pp. 631–634. DOI: [10.1103/PhysRevLett.68.631](https://doi.org/10.1103/PhysRevLett.68.631).
- [70] T. W. Odom et al. ‘Atomic structure and electronic properties of single-walled carbon nanotubes’. In: *Nature* 391.6662 (1998), pp. 62–64. DOI: [10.1038/34145](https://doi.org/10.1038/34145).
- [71] J. W. G. Wildöer et al. ‘Electronic structure of atomically resolved carbon nanotubes’. In: *Nature* 391.6662 (1998), pp. 59–62. DOI: [10.1038/34139](https://doi.org/10.1038/34139).

-
- [72] Z. Zhong et al. ‘Terahertz time-domain measurement of ballistic electron resonance in a single-walled carbon nanotube’. In: *Nature nanotechnology* 3.4 (2008), pp. 201–205. DOI: [10.1038/nnano.2008.60](https://doi.org/10.1038/nnano.2008.60).
- [73] X. Blase et al. ‘Hybridization effects and metallicity in small radius carbon nanotubes’. In: *Physical Review Letters* 72.12 (1994), pp. 1878–1881. DOI: [10.1103/PhysRevLett.72.1878](https://doi.org/10.1103/PhysRevLett.72.1878).
- [74] A. Kleiner and S. Eggert. ‘Curvature, hybridization, and STM images of carbon nanotubes’. In: *Physical review. B, Condensed matter* 64.11 (2001). DOI: [10.1103/PhysRevB.64.113402](https://doi.org/10.1103/PhysRevB.64.113402).
- [75] J. Klinovaja et al. ‘Carbon nanotubes in electric and magnetic fields’. In: *Physical Review B* 84.8 (2011). DOI: [10.1103/PhysRevB.84.085452](https://doi.org/10.1103/PhysRevB.84.085452).
- [76] C. J. Park, Y. H. Kim and K. J. Chang. ‘Band-gap modification by radial deformation in carbon nanotubes’. In: *Physical review. B, Condensed matter* 60.15 (1999), pp. 10656–10659. DOI: [10.1103/PhysRevB.60.10656](https://doi.org/10.1103/PhysRevB.60.10656).
- [77] C. L. Kane and E. J. Mele. ‘Size, Shape, and Low Energy Electronic Structure of Carbon Nanotubes’. In: *Physical Review Letters* 78.10 (1997), pp. 1932–1935. DOI: [10.1103/PhysRevLett.78.1932](https://doi.org/10.1103/PhysRevLett.78.1932).
- [78] L. Yang et al. ‘Band-gap change of carbon nanotubes: Effect of small uniaxial and torsional strain’. In: *Physical review. B, Condensed matter* 60.19 (1999), pp. 13874–13878. DOI: [10.1103/PhysRevB.60.13874](https://doi.org/10.1103/PhysRevB.60.13874).
- [79] L. Yang and J. Han. ‘Electronic structure of deformed carbon nanotubes’. In: *Physical Review Letters* 85.1 (2000), pp. 154–157. DOI: [10.1103/PhysRevLett.85.154](https://doi.org/10.1103/PhysRevLett.85.154).
- [80] T. Ando. ‘Spin-Orbit Interaction in Carbon Nanotubes’. In: *Journal of the Physical Society of Japan* 69.6 (2000), pp. 1757–1763. DOI: [10.1143/JPSJ.69.1757](https://doi.org/10.1143/JPSJ.69.1757).
- [81] F. Kuemmeth et al. ‘Coupling of spin and orbital motion of electrons in carbon nanotubes’. In: *Nature* 452.7186 (2008), pp. 448–452. DOI: [10.1038/nature06822](https://doi.org/10.1038/nature06822).
- [82] B. Witkamp et al. ‘Self-detecting gate-tunable nanotube paddle resonators’. In: *Applied Physics Letters* 93.11 (2008). DOI: [10.1063/1.2985859](https://doi.org/10.1063/1.2985859).
- [83] A. Barreiro et al. ‘Subnanometer motion of cargoes driven by thermal gradients along carbon nanotubes’. In: *Science (New York, N.Y.)* 320.5877 (2008), pp. 775–778. DOI: [10.1126/science.1155559](https://doi.org/10.1126/science.1155559).

- [84] G. Gruber et al. ‘Mass Sensing for the Advanced Fabrication of Nanomechanical Resonators’. In: *Nano letters* 19.10 (2019), pp. 6987–6992. DOI: [10.1021/acs.nanolett.9b02351](https://doi.org/10.1021/acs.nanolett.9b02351).
- [85] S. Sangiao et al. ‘Magnetic properties of optimized cobalt nanospheres grown by focused electron beam induced deposition (FEBID) on cantilever tips’. In: *Beilstein journal of nanotechnology* 8 (2017), pp. 2106–2115. DOI: [10.3762/bjnano.8.210](https://doi.org/10.3762/bjnano.8.210).
- [86] Q. Fu and J. Liu. ‘Catalytic chemical vapor deposition of single-walled carbon nanotubes’. In: *Carbon nanotechnology*. Amsterdam [etc.]: Elsevier, 2006, pp. 81–107. DOI: [10.1016/B978-044451855-2/50007-3](https://doi.org/10.1016/B978-044451855-2/50007-3).
- [87] A. Govindaraj and C.N.R. Rao. ‘Synthesis, growth mechanism and processing of carbon nanotubes’. In: *Carbon nanotechnology*. Amsterdam [etc.]: Elsevier, 2006, pp. 15–51. DOI: [10.1016/B978-044451855-2/50005-X](https://doi.org/10.1016/B978-044451855-2/50005-X).
- [88] M. Kumar and Y. Ando. ‘Chemical vapor deposition of carbon nanotubes: a review on growth mechanism and mass production’. In: *Journal of nanoscience and nanotechnology* 10.6 (2010), pp. 3739–3758. DOI: [10.1166/jnn.2010.2939](https://doi.org/10.1166/jnn.2010.2939).
- [89] M. Meyyappan. ‘A review of plasma enhanced chemical vapour deposition of carbon nanotubes’. In: *Journal of Physics D: Applied Physics* 42.21 (2009), p. 213001. DOI: [10.1088/0022-3727/42/21/213001](https://doi.org/10.1088/0022-3727/42/21/213001).
- [90] H. Kimura et al. ‘The infinite possible growth ambients that support single-wall carbon nanotube forest growth’. In: *Scientific reports* 3 (2013), p. 3334. DOI: [10.1038/srep03334](https://doi.org/10.1038/srep03334).
- [91] D. Yuan et al. ‘Horizontally aligned single-walled carbon nanotube on quartz from a large variety of metal catalysts’. In: *Nano letters* 8.8 (2008), pp. 2576–2579. DOI: [10.1021/nl801007r](https://doi.org/10.1021/nl801007r).
- [92] Y. Cao and Y. Q. Xu. ‘Controlling the growth morphology of carbon nanotubes: from suspended bridges to upright forests’. In: *Nanoscale* 4.5 (2012), pp. 1682–1687. DOI: [10.1039/c2nr11405d](https://doi.org/10.1039/c2nr11405d).
- [93] K. J. G. Götz et al. ‘Co-sputtered MoRe thin films for carbon nanotube growth-compatible superconducting coplanar resonators’. In: *Nanotechnology* 27.13 (2016), p. 135202. DOI: [10.1088/0957-4484/27/13/135202](https://doi.org/10.1088/0957-4484/27/13/135202).
- [94] S. Blien et al. ‘Quartz Tuning-Fork Based Carbon Nanotube Transfer into Quantum Device Geometries’. In: *physica status solidi (b)* 255.12 (2018). DOI: [10.1002/pssb.201800118](https://doi.org/10.1002/pssb.201800118).

- [95] J. Gramich et al. ‘Fork stamping of pristine carbon nanotubes onto ferromagnetic contacts for spin-valve devices’. In: *physica status solidi (b)* 252.11 (2015), pp. 2496–2502. DOI: [10.1002/pssb.201552213](https://doi.org/10.1002/pssb.201552213).
- [96] F. Pei et al. ‘Valley-spin blockade and spin resonance in carbon nanotubes’. In: *Nature nanotechnology* 7.10 (2012), pp. 630–634. DOI: [10.1038/nnano.2012.160](https://doi.org/10.1038/nnano.2012.160).
- [97] P. Steger. ‘Fabrication of a carbon nanotube mechanical resonator using a quartz tuning fork based transfer method’. Master thesis. University of Regensburg, 2019.
- [98] J. Waissman et al. ‘Realization of pristine and locally tunable one-dimensional electron systems in carbon nanotubes’. In: *Nature nanotechnology* 8.8 (2013), pp. 569–574. DOI: [10.1038/nnano.2013.143](https://doi.org/10.1038/nnano.2013.143).
- [99] C. C. Wu, C. H. Liu and Z. Zhong. ‘One-step direct transfer of pristine single-walled carbon nanotubes for functional nanoelectronics’. In: *Nano letters* 10.3 (2010), pp. 1032–1036. DOI: [10.1021/nl904260k](https://doi.org/10.1021/nl904260k).
- [100] K. P. Rola and I. Zobel. ‘Impact of alcohol additives concentration on etch rate and surface morphology of (100) and (110) Si substrates etched in KOH solutions’. In: *Microsystem Technologies* 19.4 (2013), pp. 635–643. DOI: [10.1007/s00542-012-1675-x](https://doi.org/10.1007/s00542-012-1675-x).
- [101] Norhafizah Burham, A. A. Hamzah and B. Y. Majlis. ‘Effect of isopropyl alcohol (IPA) on etching rate and surface roughness of silicon etched in KOH solution’. In: *2015 IEEE Regional Symposium on Micro and Nanoelectronics (RSM)*. IEEE, 19/08/2015 - 21/08/2015, pp. 1–4. DOI: [10.1109/RSM.2015.7355008](https://doi.org/10.1109/RSM.2015.7355008).
- [102] E. Abdur-Rahman, I. Alghoraibi and H. Alkurdi. ‘Effect of Isopropyl Alcohol Concentration and Etching Time on Wet Chemical Anisotropic Etching of Low-Resistivity Crystalline Silicon Wafer’. In: *International journal of analytical chemistry* 2017 (2017), p. 7542870. DOI: [10.1155/2017/7542870](https://doi.org/10.1155/2017/7542870).
- [103] Z. Jin et al. ‘Ultralow feeding gas flow guiding growth of large-scale horizontally aligned single-walled carbon nanotube arrays’. In: *Nano letters* 7.7 (2007), pp. 2073–2079. DOI: [10.1021/nl070980m](https://doi.org/10.1021/nl070980m).
- [104] T. Monteiro et al. ‘Dynamic Wet Etching of Silicon through Isopropanol Alcohol Evaporation’. In: *Micromachines* 6.10 (2015), pp. 1534–1545. DOI: [10.3390/mi6101437](https://doi.org/10.3390/mi6101437).
- [105] P. Pal et al. ‘High speed silicon wet anisotropic etching for applications in bulk micromachining: a review’. In: *Micro and Nano Systems Letters* 9.1 (2021). DOI: [10.1186/s40486-021-00129-0](https://doi.org/10.1186/s40486-021-00129-0).

- [106] K. R. Williams, K. Gupta and M. Wasilik. ‘Etch rates for micromachining processing-part II’. In: *Journal of Microelectromechanical Systems* 12.6 (2003), pp. 761–778. DOI: [10.1109/JMEMS.2003.820936](https://doi.org/10.1109/JMEMS.2003.820936).
- [107] A. Jorio and R. Saito. ‘Raman spectroscopy for carbon nanotube applications’. In: *Journal of Applied Physics* 129.2 (2021). DOI: [10.1063/5.0030809](https://doi.org/10.1063/5.0030809).
- [108] S. Jung et al. ‘Understanding and improving carbon nanotube-electrode contact in bottom-contacted nanotube gas sensors’. In: *Sensors and Actuators B: Chemical* 331 (2021), p. 129406. DOI: [10.1016/j.snb.2020.129406](https://doi.org/10.1016/j.snb.2020.129406).
- [109] R. Hanson et al. ‘Spins in few-electron quantum dots’. In: *Reviews of Modern Physics* 79.4 (2007), pp. 1217–1265. DOI: [10.1103/RevModPhys.79.1217](https://doi.org/10.1103/RevModPhys.79.1217).
- [110] A. K. Hüttel et al. ‘Nanoelectromechanics of suspended carbon nanotubes’. In: *New Journal of Physics* 10.9 (2008), p. 095003. DOI: [10.1088/1367-2630/10/9/095003](https://doi.org/10.1088/1367-2630/10/9/095003).
- [111] M. Poot and H. S. J. van der Zant. ‘Mechanical systems in the quantum regime’. In: *Physics Reports* 511.5 (2012), pp. 273–335. DOI: [10.1016/j.physrep.2011.12.004](https://doi.org/10.1016/j.physrep.2011.12.004).
- [112] M. Dequesnes, S. V. Rotkin and N. R. Aluru. ‘Calculation of pull-in voltages for carbon-nanotube-based nanoelectromechanical switches’. In: *Nanotechnology* 13.1 (2002), pp. 120–131. DOI: [10.1088/0957-4484/13/1/325](https://doi.org/10.1088/0957-4484/13/1/325).
- [113] A. Eichler et al. ‘Symmetry breaking in a mechanical resonator made from a carbon nanotube’. In: *Nature communications* 4 (2013), p. 2843. DOI: [10.1038/ncomms3843](https://doi.org/10.1038/ncomms3843).
- [114] V. Sazonova et al. ‘A tunable carbon nanotube electromechanical oscillator’. In: *Nature* 431.7006 (2004), pp. 284–287. DOI: [10.1038/nature02905](https://doi.org/10.1038/nature02905).
- [115] Nicole Kellner et al. ‘Stepwise Fabrication and Optimization of Coplanar Waveguide Resonator Hybrid Devices’. In: *physica status solidi (b)* 260.12 (2023). DOI: [10.1002/pssb.202300187](https://doi.org/10.1002/pssb.202300187).
- [116] S. L. de Bonis et al. ‘Ultrasensitive Displacement Noise Measurement of Carbon Nanotube Mechanical Resonators’. In: *Nano letters* 18.8 (2018), pp. 5324–5328. DOI: [10.1021/acs.nanolett.8b02437](https://doi.org/10.1021/acs.nanolett.8b02437).
- [117] G. A. Steele et al. ‘Strong coupling between single-electron tunneling and nanomechanical motion’. In: *Science (New York, N.Y.)* 325.5944 (2009), pp. 1103–1107. DOI: [10.1126/science.1176076](https://doi.org/10.1126/science.1176076).
- [118] D. R. Schmid et al. ‘Magnetic damping of a carbon nanotube nano-electromechanical resonator’. In: *New Journal of Physics* 14.8 (2012), p. 083024. DOI: [10.1088/1367-2630/14/8/083024](https://doi.org/10.1088/1367-2630/14/8/083024).

- [119] K. Willick and J. Baugh. ‘Self-driven oscillation in Coulomb blockaded suspended carbon nanotubes’. In: *Physical Review Research* 2.3 (2020). DOI: [10.1103/PhysRevResearch.2.033040](https://doi.org/10.1103/PhysRevResearch.2.033040).
- [120] Y. Wen et al. ‘A coherent nanomechanical oscillator driven by single-electron tunnelling’. In: *Nature physics* 16.1 (2020), pp. 75–82. DOI: [10.1038/s41567-019-0683-5](https://doi.org/10.1038/s41567-019-0683-5).
- [121] O. Usmani, Ya. M. Blanter and Yu. V. Nazarov. ‘Strong feedback and current noise in nanoelectromechanical systems’. In: *Physical Review B* 75.19 (2007). DOI: [10.1103/PhysRevB.75.195312](https://doi.org/10.1103/PhysRevB.75.195312).
- [122] S. Khan. ‘A vibrating carbon nanotube probe to study superfluid 4He’. PhD thesis. Lancaster University, 2024.